

A Study of 13 Powerful Classical Double Radio Galaxies

P. Kharb , C. P. O’Dea , S. A. Baum

Rochester Institute of Technology, 54 Lomb Memorial Drive, Rochester, NY 14623

R. A. Daly , M. P. Mory

Department of Physics, Penn State University, Berks Campus, P. O. Box 7009, Reading, PA 19610

M. Donahue

Department of Physics and Astronomy, BPS Building, Michigan State University, East Lansing, MI 48824

and

E. J. Guerra

Department of Physics and Astronomy, Rowan University, 201 Mullica Hill Rd. Glassboro, NJ 08028

ABSTRACT

We have carried out an extensive study of a sample of 13 large, powerful Fanaroff-Riley type II radio galaxies with the Very Large Array in multiple configurations at 330 MHz, 1.4, 5 and 8 GHz. We present the total intensity, polarization, spectral index, and rotation measure maps of the sources. On the whole the 13 FR II sources have symmetric structures with arm-length ratios close to unity, small misalignment angles and low values of radio core prominence, suggesting that these radio galaxies lie close to the plane of the sky. We have revisited some well known radio galaxy correlations using a large combined dataset comprising our radio galaxies and others from the literature. We confirm that the hotspot size correlates with the core-hotspot distance. The hotspot spectral index is correlated with, and flatter than the lobe spectral index, consistent with the assumptions of spectral aging models. Both the hotspot and lobe spectral index are correlated with redshift. The depolarization asymmetry in the lobes is not correlated with the radio core prominence or misalignment angle, which are statistical indicators of orientation. The ‘Liu-Pooley’ correlation of lobe depolarization with the lobe spectral index is significant in our radio galaxy

sample. Further, the lobe with the steeper spectral index and greater depolarization is shorter and fatter. The arm-length ratio seems to be correlated with the misalignment angle between the two sides of the radio source and strongly anti-correlated with the axial ratio, consistent with environmental effects and/or a change in the outflow direction. In this sample, asymmetries in the local environments and/or motion of the outflow axis are likely to be more important than relativistic beaming effects.

Subject headings: galaxies: active — radio continuum: galaxies

1. INTRODUCTION

Classical double radio galaxies are active galactic nuclei with regions of synchrotron-emitting plasma that can extend to thousands of kiloparsecs. These Fanaroff-Riley type II radio galaxies (Fanaroff & Riley 1974) are thought to be powered by narrow collimated jets, terminating in high surface brightness regions called ‘hotspots’. Regions of low surface brightness emission lying between the galaxy center and the hotspots, called radio bridges, are believed to be a result of the accumulation of relativistic particles accelerated at the hotspots over the lifetime of an FR II source that form a low-density cocoon around the jet (see Begelman et al. 1984, for a theoretical review). The ultimate motivation of our project is to study the radio bridges in FR II radio galaxies and do a spectral aging analysis. In this paper we present the first results of our study and describe the global properties of our FR II radio galaxy sample.

In order to comprehend the phenomenology of FR II galaxies, large samples of radio galaxies have hitherto been observed, yielding an extensive database of information. Results from arcsecond-scale radio observations of FR II radio galaxies have been presented by many authors, for example, Laing (1981); Leahy & Williams (1984); Alexander & Leahy (1987); Leahy et al. (1989); Pedelty et al. (1989); Garrington et al. (1991); Liu et al. (1992); Hardcastle et al. (1998); Ishwara-Chandra et al. (2001); Goodlet et al. (2004); Gilbert et al. (2004) and Mullin et al. (2006), and others. Previous studies of the radio bridges have included relatively low-resolution observations ($\sim 3'' - 4''$) at 151 MHz and 1.4 GHz of the full bridge region (e.g., Leahy et al. 1989), while the higher resolution observations ($\sim 1''$) at 1.4, 5 and 15 GHz have sampled the bridge emission partially (e.g., Liu et al. 1992). However, to empirically address and understand the different physical processes that are important at different radio frequencies, physical locations, and stages of evolution of a source, both low-frequency radio data and high-resolution radio data are required.

To this end, we observed 13 FR II radio galaxies with the Very Large Array (VLA) in multiple configurations at 330 MHz, 1.4 GHz, 5 GHz, and 8 GHz. Here we present images of the total and polarized radio intensity, spectral index between 1.4 and 5 GHz, 0.3 and 1.4 GHz, and rotation measure between 1.4 and 5 GHz¹. Further, we probe the relationship between different global characteristics of the radio galaxies by augmenting our data with additional galaxy data gleaned from the literature. We will subsequently refer to this extended, eclectic sample as the “combined” dataset, while the 13 FR II galaxies will be referred to as such.

The paper is arranged as follows: the radio galaxy sample is described in Sect. 2 while the observations and data reduction are discussed in Sect. 3; the source properties are presented in Sect. 4; the correlations are discussed in Sect. 5; and the summary and conclusions follow in Sect. 6. This paper is the first in a series of four papers. In Paper II, we will present the results of the spectral aging analysis, lobe propagation velocities, pressures, beam powers, and ambient gas densities. In Paper III, we will describe the use of these sources for cosmological studies and present the results for a large sample of powerful FR II galaxies. Finally, in Paper IV, we will present a detailed analysis of the radio bridge structure of the sources.

Throughout the paper, we have adopted the cosmology in which $H_0=71 \text{ km s}^{-1} \text{ Mpc}^{-1}$, $\Omega_m=0.27$ and $\Omega_\Lambda=0.73$. The spectral indices α are defined such that the flux density S_ν at frequency ν , is $S_\nu \propto \nu^{-\alpha}$.

2. THE SAMPLE

The FR II radio galaxies considered for the present study are part of the 3CR sample of radio sources (Bennett 1962). The 13 sources which are a focus of this paper were those for which we were allocated observing time, from a larger sample of powerful FR II sources selected for an extensive study of their radio bridges. These sources satisfy the following criteria: their radio power at 178 MHz is greater than $10^{28} \text{ W Hz}^{-1}$; their angular sizes are larger than $27''$, they span the redshift range of $z \simeq 0.4\text{--}1.65$, and are classified as narrow-line FR II radio galaxies (Hes et al. 1996; Jackson & Rawlings 1997). The largest source in our sample, 3C172, has an angular extent of $\geq 100''$, which corresponds to a linear size of $\simeq 680 \text{ kpc}$. The large angular sizes ensure that the radio lobes span several beam widths, crucial for the spectral aging study, which will be presented in Paper II. A compilation of the basic parameters for each source is given in Table 1.

¹Spectral index and RM maps are available only in the electronic version

Table 1. The sample of FR II radio galaxies

Source	IAU name	z	S_{178} (Jy)	$\log(P_{178})$ (W Hz $^{-1}$)	Scale (kpc/″)	Θ , PA (″, deg)	LAS (″)	LAS (kpc)	Ref
(1)	(2)	(3)	(4)	(5)	(6)	(7)	(8)	(9)	(10)
3C6.1	0013+790	0.8404	14.9	28.68	7.6	26.0, 27.3	31.5	241	9, 12
3C13	0031+391	1.3510	13.1	29.14	8.5	28.6, 145.1	32.5	276	4, 8
3C34	0107+315	0.6900	13.0	28.41	7.1	45.1, 82.9	48.7	346	9, 12
3C41	0123+329	0.7940	11.6	28.51	7.5	23.8, 145.1	27.2	204	9, 12
3C44	0128+061	0.6600	10.0	28.24	6.9	64.8, 12.8	72.0	502	7
3C54	0152+435	0.8274	10.5	28.51	7.6	51.1, 23.6	60.2	458	1, 2
3C114	0417+177	0.8150	8.2	28.38	7.6	53.2, 44.3	59.6	451	1, 6
3C142.1	0528+064	0.4061	18.6	28.00	5.4	52.4, 130.1	55.5	299	7
3C169.1	0647+452	0.6330	6.6	28.02	6.8	45.9*, 135.7*	53.6	367	9
3C172	0659+253	0.5191	16.5	28.21	6.2	101.2, 16.6	109.0	676	5, 11
3C441	2203+292	0.7070	13.7	28.45	7.2	33.3, 149.8	41.7	299	9, 12
3C469.1	2352+796	1.3360	12.1	29.09	8.5	75.4, 171.1	84.1	712	2
3C470	2356+437	1.6530	11.0	29.28	8.6	24.9, 37.9	29.8	255	3, 10

Note. — Cols.1 & 2: Common and IAU names of the FR II radio galaxies. Col.3: Redshifts were obtained from the NASA/IPAC Extragalactic Database (NED). Col.4 : Total flux density at 178 MHz in Jy on the Baars et al. (1977) scale taken from <http://www.3crr.dyndns.org/cgi/database> – for 5 sources not listed in Laing et al. (1983), we used the 4C flux densities from Gower et al. (1967) multiplied by a factor of 1.09 to convert them to Baars et al. scale following Roger et al. (1973). Col.5: Logarithm of the total luminosity at 178 MHz. Col.6: Spatial scale in source corresponding to 1″. Col.7: Angular extent and position angle of the source, measured from the VLA A-array 8 GHz maps using the brightest hotspot. The position angle is defined as counter-clockwise from North. * For 3C169.1, the northern hotspot was not detected in the 8 GHz image – the 2.5″ 5 GHz image was used instead to obtain the extent. Col.8: Largest angular size measured from the $\sim 2''$ image at 1.4 GHz. The AIPS task TVDIST was used to measure the entire radio extent (from hotspot-to-hotspot) of the source. Col.9: Largest projected linear size of source estimated using values in Cols 7 and 9. Col.10: References for previous observations (this is not an exhaustive list): 1 - MacDonald et al. (1968), 2 - Longair (1975), 3 - Riley & Pooley (1975), 4 - Schilizzi et al. (1982), 5 - Strom & Conway (1985), 6 - Strom et al. (1990), 7 - Bogers et al. (1994), 8 - Law-Green et al. (1995), 9 - Neff et al. (1995), 10 -

Best et al. (1997), 11 - Gilbert et al. (2004), 12 - Mullin et al. (2006).

3. OBSERVATIONS AND DATA ANALYSIS

The 13 FR II radio galaxies were observed with the A, B, C and D-array configurations of the VLA (Napier et al. 1983) between November, 2002 and November, 2003 at 330 MHz, 1.4, 4.8 and 8.4 GHz. Table 2 provides a summary of the VLA observations. The sources were observed in a ~ 10 min snapshot mode. In order to be able to extract possible radio frequency interference, which can become significant at low frequencies, the 330 MHz data were observed in the spectral-channel mode. While making the radio maps at 330 MHz, only the central 80% of the spectral channels were averaged. Scheduling constraints resulted in some sources not being observed at some frequencies. For a few sources, VLA archival data existed at one or more frequencies and these were not observed (see Table 3). We used the VLA archival data for these sources, the program IDs of which are listed in Table 3.

The data were reduced using the standard calibration and reduction procedures in the Astronomical Image Processing System (AIPS). 3C48 was used as the primary flux density calibrator for the experiment. The instrumental polarization and electric vector position angles were calibrated using 0217+738 and 3C138, respectively. The polarization data at 1.4 GHz were corrected for ionospheric Faraday rotation using the total electron content maps available at CDDIS data archive² in the AIPS task TECOR.

After the initial amplitude and phase calibration using the calibrators, the source data were phase and amplitude self-calibrated (Schwab 1980) and imaged in an iterative manner, using the tasks CALIB and IMAGR. In order to improve the UV coverage, we combined the self-calibrated datasets from the various configurations at a given frequency using the AIPS task DBCON, and performed additional rounds of phase and amplitude self-calibration on the combined datasets. Table 2 lists the largest angular scale structure which can be imaged well in single snapshot observations with the different VLA configurations. A quick comparison with the angular sizes of our 13 FR II galaxies listed in Table 1 demonstrates that our sources were imaged reasonably well when the data from A, B and C-arrays were combined at the L-band, B, C and D-arrays were combined at the C-band, and A and C-arrays were combined at the P-band.

The polarization maps were made by combining the Stokes Q and U images using the AIPS task COMB. We split our L-band data into its constituent Intermediate frequencies (IFs, see Table 2) and used the lower frequency, *ie.*, 1345 MHz and the averaged C-band data at 4860 MHz, to create the spectral index maps using the AIPS task COMB. For the rotation measure maps, we used the three frequencies, 1345, 1665 and 4860 MHz, in the

²ftp cddisa.gsfc.nasa.gov

AIPS task RM. When archival data were used, we could still combine the respective L-band IFs, which sometimes differed from our frequencies, to the closest frequency in our data. For 3C142.1 we noticed RM flips across the southern lobe, which were a result of the $n\pi$ ambiguity in the polarization angles. We therefore used a guess (integrated) RM value of $+84 \text{ rad m}^{-2}$ (Simard-Normandin et al. 1981) in the AIPS task RM for the rotation measure map of 3C142.1.

We typically recover 95% to 100% of the integrated flux density listed in Kuehr et al. (1996) at the L and C-bands. For 3C441 and 3C469.1, between 85% and 90% of the integrated flux density is recovered in our maps. The registration of images for the spectral index and rotation measure maps is better than $\sim 0.1''$. By blanking values in the task COMB, the polarization intensity, polarization angle and fractional polarization maps were restricted to have $S/N > 3$, output errors less than ≈ 10 degrees and 10%, respectively. No Ricean bias correction (e.g., Wardle & Kronberg 1974) was made to the polarized intensity. The mean rotation measure and the dispersion/spread in rotation measure, σ_{RM} was obtained by using the AIPS task IMEAN.

4. RESULTS

The final maps at 1.4 GHz and 5 GHz, restored with a $2.0''$ or $2.5''$ circular Gaussian beam, the 330 MHz maps restored with a $5.0''$ circular Gaussian beam, and the 8 GHz maps with insets for the hotspots, are presented in Figs. 13 to 49. The total intensity contours are superimposed with the fractional polarization vectors. 1.4 GHz polarization maps could not be made for 3C6.1 and 3C41 because their respective (archival) datasets did not include scans of a polarization angle calibrator. The dynamic range in the final images (defined as peak brightness/rms noise) varies from 7400 to 400, being typically greater than 3000. The 1.4–5 GHz spectral index and RM maps were made at a resolution of $2.0''$ or $2.5''$, while the 0.3–1.4 GHz spectral index maps were made at a resolution of $5.0''$.

The high resolution A-array 8 GHz images reveal the details of the hotspot structure. Most sources show the presence of multiple hotspots. These could be due to the plasma beam moving about along the cavity wall as in the ‘dentist’s drill’ model (Scheuer 1982). Alternatively, multiple hotspots could be interpreted as ‘splatter-spots’ formed by a jet with a variable direction (Williams & Gull 1985). Table 6 presents selected characteristics of the hotspots in our 13 FR II galaxies. Our high-resolution 8 GHz images reveal that the brightest hotspots at either end, which probably are the current acceleration sites of particles, lie roughly along a line connecting the hotspots and the core for each of the 13 sources.

Table 2. Summary of VLA Observations

Obs. Date	Config.	Band	Frequency (MHz)	Bandwidth (MHz)	Int. Time (mins)	θ_{LAS} (")
(1)	(2)	(3)	(4)	(5)	(6)	(7)
June 17, 2003	A	P	327.5, 321.5	3.1	8	85.0
		L	1344.9, 1664.9	25	11	19.0
		X	8435.1, 8485.1	25	11	3.5
Nov. 29, 2003	B	L	1344.9, 1664.9	25	9	60.0
		C	4885.1, 4835.1	50	9	18.0
Nov. 4, 2002	C	P	327.5, 321.5	3.1	6	2100.0
		L	1344.9, 1664.9	25	9	450.0
		C	4885.1, 4835.1	50	9	150.0
Apr. 11, 2003	D	C	4885.1, 4835.1	50	8	150.0

Note. — Col.1: Observing date, Col.2: VLA Array configuration, Col.3: Observing frequency band, Col.4 & 5: Central frequency for the 2 constituent IFs in each frequency band, and bandwidth respectively, Col.6: Integration time in minutes, Col.7: The largest angular scale structure which can be imaged reasonably well in single snapshot observations (see The VLA Observational Status Summary). The P-band data were observed in the spectral-line mode.

Table 3. Observation Summary of the Sample

Source	A/P	A/L	A/X	B/L	B/C	C/P	C/L	C/C	D/C
3C6.1	...	AH291	AP380	...	N	AJ111	...
3C13	N	AA150	AL322	N	N	VAH54
3C34	N	AG247	AL322	N	N	N	N	N	AP380
3C41	...	AH291	AP380	...	AG220
3C44	N	N	N	N	N	N	N	N	...
3C54	N	N	N	N	N	N	N	N	N
3C114	N	N	N	N	N	N	N	N	N
3C142.1	N	AH480	N	N	N	N	N	N	N
3C169.1	N	N	N	N	N	N	N	N	N
3C172	N	N	AP361	N	N	N	N	N	N
3C441	N	N	N	N	N	N	N	N	N
3C469.1	N	N	N	N	N	N	N	N	N
3C470	AB917	N	AL322	N	N	AH343	...

Note. — N: New observations made by us (Program ID - AO170). AH291, AA150, etc.,: Program IDs for Archival observations. ... : No observations due to scheduling constraints.

Radio bridges are detected in all but two sample radio galaxies *viz.*, 3C13 and 3C470. These sources are the most luminous and the most distant in our sample, and are likely to be strongly affected by $(1+z)^4$ surface brightness dimming. Therefore, more sensitive observations are required to detect the radio bridges in these sources. The spectral index maps show a gradual steepening of the radio spectra away from the hotspots with some spectral index variations superimposed, in agreement with previous studies (e.g., Myers & Spangler 1985; Alexander 1987; Alexander & Leahy 1987). Some quantitative estimates of the radio lobe properties are tabulated in Table 5.

The majority of the sources exhibit a regular bridge structure, with some distortions becoming apparent at very low surface brightness. We have classified distortions using the radio morphology classification of Leahy & Williams (1984): Type 1 (hereafter LW1) morphology describes a bridge with no distortions but a marked decrease in the bridge surface-brightness towards the centre; Type 2 (hereafter LW2) describes a bridge which bends away from the central galaxy only on one side; Type 3 (LW3) describes a bridge which bends away from the galaxy on both sides in a cross-shape; Type 4 (LW4) is a radio bridge which bends on both sides in the same direction away from the host galaxy; and Type 5 (LW5) describes a bridge that is continuous across the galaxy which is displaced towards the steepest edge of the radio source. The bridge types are presented in Table 5.

The radio core prominence (R_c) is the ratio of the flux density from the radio core (S_{core}) to the extended radio lobe emission (S_{ext}). In the restframe of the source, $R_c = \frac{S_{core}}{S_{ext}}(1+z)^{\alpha_{core}-\alpha_{ext}}$, where z is the redshift of the source, and α is the spectral index, assumed to be 0 and 1 for the core and extended emission, respectively. Due to Doppler beaming effects in the radio core (which is the unresolved base of the relativistic jet), R_c can be used as a statistical indicator of beaming and therefore orientation (Kapahi & Saikia 1982; Orr & Browne 1982). We have derived R_c using the radio core flux densities from the high-resolution 8 GHz maps (where the core is clearly delineated) and lobe flux densities from the 1.4 GHz maps (see Table 4). The lobe flux density is primarily all the extended radio emission minus the radio core, and therefore includes the emission from the hotspots and jets. We find that the core prominence in our 13 FR II radio galaxies is small – R_c varies from 4.7×10^{-5} to 0.0029. This is consistent with the picture of these radio galaxies oriented close to the plane of the sky.

In Table 5 we have tabulated the mean values of the rotation measure (RM) and the corresponding dispersion (σ_{RM}) in the radio lobes of our 13 FR II galaxies. The mean RM was averaged over the two lobes. We have estimated the lobe depolarization parameter, DP , as $DP = \frac{m_l}{m_h}$, where m_h , m_l are the fractional polarizations at high and low frequencies, respectively. A higher value of DP implies lower depolarization. We created DP maps using

the lower frequency L-band (IF1) and the C-band fractional polarization maps in AIPS using the task COMB. We used these maps to obtain a mean lobe DP by putting a box around each lobe (using AIPS verbs TVWIN and IMSTAT).

Note that a few sources have $DP > 1$. While the degree of polarization will occasionally increase with wavelength by chance due to Faraday effects, a close examination of our maps revealed that the high DP values were mostly obtained for those sources which showed polarization at 1.4 GHz only in the hotspots, where the systematic errors are expected to be the highest (e.g., 3C13, 3C54-North, 3C469.1-North, 3C470). Residual instrumental polarization errors and errors in the position-angle zero-point contribute to the total error in DP , especially since data from multiple configurations has been combined to get the polarization maps. The DP errors quoted in Table 5 were estimated by taking the difference in the DP obtained using the L-band IF1 or IF2, and the C-band, respectively. In our discussions of lobe depolarization we have therefore excluded all values of DP that are not estimated over the radio lobes.

The spectral index for the lobes in Table 5 was obtained by putting a box around the lobe in the spectral index map and getting a mean value. The hotspot spectral index was taken as the value in this map corresponding to the total intensity peak position at the hotspot. The arm-length ratio (Q) is the ratio of the angular extent of the larger radio lobe (core to hotspot) to the smaller. Another fundamental structural parameter is the axial ratio (AR), which is the ratio of the length to width of the radio lobe. The axial ratio was estimated for our radio galaxies following Leahy & Williams (1984) - the width was estimated of a section of the radio lobe roughly half-way between the hotspot and the core and defined as $2/\sqrt{3}$ times the FWHM of the Gaussian function fitted to the lobe surface brightness. We used the 1.4 GHz maps to get the widths and the 8 GHz maps to get accurate lengths. Table 5 presents the arm-length and axial ratios for the sample FRII radio galaxies.

Table 4. Properties of the Radio Components

Source	Freq (GHz)	S_ν (N lobe) (Jy)	S_ν (S lobe) (Jy)	S_ν (Core) (mJy)	S_8 (Core) (mJy)	Log R_c	Lobe Type	Jet-side N, S
(1)	(2)	(3)	(4)	(5)	(6)	(7)	(8)	(9)
3C6.1	5.0	0.58	0.51	...	7.52	-2.90	LW1
	1.4	1.75	1.49	10.14				
	0.33				
3C13	5.0	0.29	0.11	...	< 0.29 [†]	-4.19
	1.4	1.25	0.61	...				
	0.33	4.56	3.16	...				
3C34	5.0	0.22	0.16	1.91	0.69	-3.47	LW1	...,Jet
	1.4	0.69	0.54	3.23				
	0.33	2.79	2.38	...				
3C41	5.0	0.44	0.86	...	2.38	-3.40	LW3	...,Jet ^a
	1.4	1.29	2.05	...				
	0.33				
3C44	5.0	0.12	0.21	0.21	0.25	-3.94	LW1
	1.4	0.48	0.79	...				
	0.33	1.58	3.11	...				
3C54	5.0	0.21	0.36	...	0.36	-3.96	LW1	...,Jet
	1.4	0.65	1.11	...				
	0.33	2.03	3.66	...				
3C114	5.0	0.13	0.14	12.38	5.41	-2.53	LW1	...,Jet?
	1.4	0.47	0.52	13.85				
	0.33	1.81	1.96	...				
3C142.1	5.0	0.51	0.38	4.97	1.17	-3.57	LW1
	1.4	1.88	1.28	7.95				
	0.33	6.89	3.97	...				
3C169.1	5.0	0.14	0.21	0.81	0.75	-3.40	LW1
	1.4	0.44	0.68	5.13				
	0.33	1.42	2.12	...				
3C172	5.0	0.39	0.51	...	0.29	-4.18	LW5
	1.4	1.29	1.55	...				
	0.33	3.79	4.14	...				
3C441	5.0	0.55	0.23	...	< 0.19 [†]	-4.32	LW3	Jet,...
	1.4	1.65	0.79	...				
	0.33	5.60	3.25	...				
3C469.1	5.0	0.19	0.22	4.08	1.58	-3.40	LW1	...,Jet?
	1.4	0.85	0.84	4.77				
	0.33	3.69	2.81	...				
3C470	5.0	0.07	0.47	1.85	0.55	-3.97
	1.4	0.17	1.75	...				
	0.33	0.42	6.43	...				

Note. — Col.1 & 2: Source name and the observing frequency in GHz, respectively. Col.3 & 4: Radio flux density in the northern and southern radio lobe, respectively, obtained by putting a box around the lobe region and using the AIPS verb IMSTAT. Col.5: Radio core flux density in mJy. Col.6: 8 GHz core flux density in mJy. † For sources where core was not detected, an upper limit is derived assuming the core flux density to

be below five times the rms noise level. Col.7: Logarithm of the K-corrected radio core prominence parameter, defined as the ratio of (8 GHz) core to (1.4 GHz) lobe flux density (see Sect. 4). Col.8: Lobe type (see Sect. 4). Col.9: The side of the source on which a jet-like feature was observed. These tend to be faint and only visible in the grey-scale images (see Fig. 69). Tentative features are marked with “?”. ^a The jet in 3C41 was noted by Mullin et al. (2006). Note that all estimates for 3C34 are for the eastern and western lobe, respectively.

5. Radio Galaxy Properties and Correlations

In the following sections we describe some global properties of the 13 FRII galaxies. Further, we have revisited some well-known correlations for FRII radio galaxies using the “combined” dataset comprising our sample galaxies and other FRII radio galaxies taken from the literature.

5.1. Data from the Literature

In order to understand the properties of FRII radio galaxies better, we augmented our data with similar radio galaxy data from the literature. The additional data comes primarily from Leahy & Williams (1984); Leahy et al. (1989); Pedelty et al. (1989); Garrington et al. (1991); Liu & Pooley (1991b); Hardcastle et al. (1998) and Goodlet et al. (2004) (see Table 7). We emphasize here that the data from the literature is inhomogeneous and chosen on the basis of the availability of the relevant physical parameters that we wished to examine in samples of (primarily 3C) FRII radio galaxies observed at a resolution of a few arcseconds. We have excluded radio-loud quasars from our analysis, and restricted our selection to powerful FRII radio galaxies at a redshift-range matching our sample. The combined dataset includes a few broad-line radio galaxies.

When not listed explicitly in the above-mentioned references, the arm-length ratios and misalignment angles were directly estimated (using a ruler and protractor) from the maps presented in these papers. Therefore, the angle estimates have errors of the order of a few degrees, while the error in the arm-length ratios is expected to be less than 10%. When no radio core was observed in the maps, the position of the centre of the host galaxy was used for the core position. The host galaxy positions were procured either from the papers directly or through the NASA/IPAC Extragalactic Database (NED)³. For the 13 FRIIs, radio core prominence was derived using the 8 GHz core and 1.4 GHz lobe flux densities. If similar data were not available in the literature, we converted flux densities from other frequencies to 1.4 GHz for lobe and 8 GHz for core emission by assuming a spectral index of 1 and 0 respectively.

³<http://nedwww.ipac.caltech.edu/>

Table 5. Properties of the Radio Lobes

Source	$\Theta_{N, S}$ (" , ")	Q	ζ (deg)	$\langle RM \rangle$ (rad m ⁻²)	σ_{RM} (rad m ⁻²)	DP N, S	Error in DP	$\alpha_5^{1.4}$ N, S	$\alpha_{1.4}^{0.3}$ N, S	AR N, S	$\log(l_j/l_{cj})$
(1)	(2)	(3)	(4)	(5)	(6)	(7)	(8)	(9)	(10)	(11)	(12)
3C6.1	13.89,12.09	1.15	2.4	...,...	...,...	...,...	...,...	1.121,1.123	...,...	2.74,2.65	...
3C13*	16.46,12.11	1.36	3.4	60.49,...	28.04,...	0.73,1.43	0.37,0.5	1.278,1.539	0.983,1.121	...,...	...
3C34‡	23.98,21.10	1.14	3.0	-62.30,-63.16	19.13,7.73	0.91,0.75	0.07,0.15	1.281,1.311	0.955,0.942	4.79,3.81	-0.056
3C41	12.53,11.32	1.11	1.5	...,...	...,,...	...,...	0.996,1.095	...,...	3.21,2.68	-0.044
3C44	40.15,24.69	1.63	5.9	4.01,14.60	11.93,31.23	1.79,1.00	0.25,0.19	1.294,1.451	0.876,1.172	7.55,5.82	...
3C54	26.59,24.71	1.07	8.9	-78.95,-70.15	3.90,14.11	1.27,1.23	0.36,0.40	1.093,1.161	0.919,1.030	3.69,4.08	-0.032
3C114	25.43,27.73	1.09	0.1	-2.10,-6.50	12.70,17.80	0.39,0.59	0.27,0.01	1.267,1.247	1.031,1.205	4.32,4.68	0.037
3C142.1	18.30,34.14	1.87	3.4	83.02,85.01	19.03,12.16	0.62,0.94	0.13,0.17	1.179,1.018	0.886,0.752	1.98,5.20	...
3C169.1	19.19,27.69	1.44	14.6	9.22,11.29	9.63,15.40	0.99,0.89	0.07,0.08	1.057,1.105	0.888,0.876	2.05,3.39	...
3C172	47.33,53.49	1.13	7.8	25.87,1.72	13.68,34.55	1.09,1.54	0.07,0.50	0.859,0.772	0.753,0.770	4.29,5.14	...
3C441*	9.67,23.66	2.45	4.8	75.05,68.23	9.97,16.23	0.44,0.76	0.02,0.35	1.129,1.176	1.002,1.024	1.78,4.41	-0.389
3C469.1	36.44,38.99	1.07	2.1	19.60,8.99	14.70,16.34	1.26,1.09	0.12,0.07	1.280,1.262	1.277,0.994	7.30,6.41	0.028
3C470	14.36,10.54	1.36	3.7	..., -7.68	..., 32.10	..., 1.23	..., 0.5	0.708,1.118	0.670,0.920	...,...	...

Note. — Col.1: Source names. Col.2: Angular extent of source from the hotspot to the radio core, for the northern and the southern side, respectively, obtained using the high resolution 8 GHz maps. Sources with an * in Col.1 did not show a radio core in the 8 GHz image - host galaxy positions for 3C13 and 3C441 were obtained from McCarthy et al. (1997) and Fernini et al. (1997), respectively. Col.3: Arm-length ratio, derived by taking the ratio of the two angular extents listed in Col.2. Col.4: Misalignment angle in degrees, derived by taking the difference between PAs obtained for both sides of the source. Col.5: Mean value of rotation measure (RM) for the northern and the southern side of the source, respectively. Col.6: Dispersion in RM for the radio lobes. Col.7: Depolarization parameter for the northern and southern lobes, respectively. A higher value of DP implies lower lobe depolarization. Col.8: Error in Depolarization estimated by taking a difference in the DP obtained by the C-band and the two IFs in the L-band, respectively. Col.9: Average spectral index between 1.4 and 5 GHz, for the northern and southern lobes, respectively. Col.10: Average lobe spectral index between 330 MHz and 1.4 GHz. Col.11: Axial-ratio for both the radio lobes. N, S stand for the northern and southern side of source. Col.12: Logarithm of the arm-length ratio of the jet to the counterjet side. ‡ For 3C34, all the estimates are for the eastern and western lobe, respectively.

Table 6. Properties of Hotspots

Source	Morph	Comp	Size	I_{peak}^8	$I_{peak}^{1.4}$	I_{peak}^5	$\alpha_{1.4}^5$	$\alpha_{1.4}^{0.3}$
(1)	(2)	(3)	(θ_{maj}'' , θ_{min}'' , PA $^\circ$)	(mJy/bm)	(mJy/bm)	(mJy/bm)	(2'')	(5'')
			(4)	(5)	(6)	(7)	(8)	(9)
3C6.1	Multiple	NH1	0.39, 0.25, 134.69	46.7	1217.0	435.1	0.85	...
		NH2	0.33, 0.24, 99.64	26.4
		SH	0.49, 0.44, 77.25	17.1	891.5	324.9	0.83	...
3C13	Single	NH	0.23, 0.09, 130.63	57.2	1066.0	270.1	1.13	0.86
		SH	0.22, 0.17, 161.55	17.8	499.3	91.6	1.41	1.09
3C34	Multiple	EH1	0.56, 0.47, 169.23	2.7	145.7	57.8	0.82	0.74
		EH2	1.24, 0.87, 9.55	1.8
		WH	0.39, 0.26, 179.44	1.5	38.3	15.0	0.86	0.70
3C41	Multiple	NH	0.46, 0.22, 20.53	8.0	446.9	178.8	0.73	...
		SH1	0.42, 0.32, 120.46	33.2	981.8	502.1	0.55	...
		SH2	0.33, 0.23, 76.19	33.3
3C44	Multiple	NH1	0.30, 0.22, 68.96	4.3	198.5	63.2	0.89*	0.91
		NH2	0.45, 0.28, 153.92	2.7
		SH	0.26, 0.17, 44.66	22.7	429.9	137.1	0.89*	0.81
3C54	Single	NH	0.19, 0.16, 31.99	7.5	289.6	105.7	0.79*	0.74
		SH	0.18, 0.10, 28.75	68.9	592.6	228.9	0.73*	0.71
3C114	Single	NH	0.33, 0.23, 104.83	2.2	108.5	37.5	0.82*	0.79
		SH	0.30, 0.15, 142.78	6.7	206.5	69.7	0.83*	0.81
3C142.1	Single	NH	0.42, 0.17, 41.45	1.8	376.8	123.3	0.89	0.83
		SH	0.46, 0.25, 67.12	1.6	183.3	66.3	0.77	0.82
3C169.1	Single	NH	49.6	18.2	0.80*	0.82
		SH	0.41, 0.23, 50.37	1.6	153.8	57.5	0.77*	0.77
3C172	Multiple	NH1	0.99, 0.76, 174.07	3.4	394.5	119.8	0.93*	0.73
		NH2	0.72, 0.49, 42.54	1.9
		NH3	1.22, 0.42, 173.03	1.9
		NH4	0.79, 0.58, 66.43	1.64
3C441	Single	SH	0.35, 0.23, 124.89	11.1	486.2	153.9	0.89*	0.71
		NH	0.29, 0.18, 98.68	31.9	424.8	186.1	0.64*	0.84
3C469.1	Multiple	SH	0.30, 0.17, 110.01	1.6	226.8	68.6	0.95*	0.98
		NH1	0.44, 0.30, 1.12	2.6	549.7	131.5	1.13*	0.97
3C470	Multiple	NH2	1.16, 0.77, 67.51	1.4
		NH3	0.69, 0.26, 27.40	1.8
		SH1	0.80, 0.53, 60.79	4.2	395.6	114.8	0.96*	0.83
		SH2	0.42, 0.33, 28.95	2.2
		NH	0.30, 0.13, 15.80	20.1	156.5	62.5	0.71	0.59
		SH1	0.22, 0.18, 57.18	38.6	1201.0	318.7	1.02	0.91
		SH2	0.91, 0.43, 33.06	17.0

Note. — Hotspot properties derived from the high-resolution 8 GHz images. Col.2: Morphology of the hotspot region – whether single or multiple hotspots. Col.3: NH, SH, EH and WH denote northern, southern, eastern and western hotspots respectively; NH2 is the second brightest hotspot and so on. Col.4: Major and minor axes of the deconvolved hotspot sizes, estimated using AIPS task JMFIT. Col.5: Peak surface brightness of hotspot at 8 GHz derived by JMFIT. Col.6 & 7: Peak surface brightness of hotspot at 1.4 and 5.0 GHz, respectively, from the 2.0'' (or 2.5'') total intensity map (data from both IFs were averaged). Col.8, & 9: Hotspot spectral index between 1.4 and 5 GHz, & between ~330 MHz and 1.4 GHz, respectively. *= Maps at 2.5'' were used.

Table 7. Data from the Literature

Source	z	Ref	Source	z	Ref
3C16	0.405	Goodlet et al. (2004)	3C268.1	0.970	Goodlet et al. (2004)
3C20	0.174	Hardcastle et al. (1998)	3C274.1	0.422	Leahy & Williams (1984)
3C27	0.184	Leahy et al. (1989)	3C277.2	0.766	Pedely et al. (1989)
3C42	0.395	Goodlet et al. (2004)	3C280	0.996	Goodlet et al. (2004)
3C46	0.437	Goodlet et al. (2004)	3C284	0.239	Leahy & Williams (1984)
3C52	0.285	Leahy & Williams (1984)	3C285	0.079	Leahy & Williams (1984)
3C55	0.734	Leahy et al. (1989)	3C288	0.246	Liu & Pooley (1991b)
3C65	1.176	Goodlet et al. (2004)	3C289	0.967	Liu & Pooley (1991b)
3C68.2	1.575	Leahy et al. (1989)	3C294	1.779	Liu & Pooley (1991b)
3C79	0.2559	Hardcastle et al. (1998)	3C299	0.367	Goodlet et al. (2004)
3C98	0.0306	Hardcastle et al. (1998)	3C300	0.270	Leahy & Williams (1984)
3C103	0.330	Leahy & Williams (1984)	3C322	1.681	Leahy et al. (1989)
3C105	0.089	Hardcastle et al. (1998)	3C324	1.206	Goodlet et al. (2004)
3C111	0.048	Leahy & Williams (1984)	3C327	0.1039	Hardcastle et al. (1998)
3C123	0.2177	Hardcastle et al. (1998)	3C330	0.550	Leahy et al. (1989)
3C132	0.214	Hardcastle et al. (1998)	3C337	0.635	Pedely et al. (1989)
3C135	0.1273	Hardcastle et al. (1998)	3C341	0.448	Goodlet et al. (2004)
3C136.1	0.064	Leahy & Williams (1984)	3C349	0.205	Hardcastle et al. (1998)
3C139.2	...	Leahy & Williams (1984)	3C352	0.806	Garrington et al. (1991)
3C153	0.2771	Hardcastle et al. (1998)	3C353	0.0304	Hardcastle et al. (1998)
3C165	0.295	Leahy & Williams (1984)	3C356	1.079	Pedely et al. (1989)
3C166	0.244	Leahy & Williams (1984)	3C368	1.131	Pedely et al. (1989)
3C171	0.2384	Hardcastle et al. (1998)	3C401	0.201	Hardcastle et al. (1998)
3C173.1	0.292	Hardcastle et al. (1998)	3C403	0.059	Hardcastle et al. (1998)
3C184.1	0.1182	Hardcastle et al. (1998)	3C405	0.056	Leahy & Williams (1984)
3C192	0.0598	Hardcastle et al. (1998)	3C424	0.127	Hardcastle et al. (1998)
3C197.1	0.1301	Hardcastle et al. (1998)	3C436	0.2145	Hardcastle et al. (1998)
3C200	0.458	Garrington et al. (1991)	3C438	0.290	Hardcastle et al. (1998)
3C217	0.897	Pedely et al. (1989)	3C452	0.0811	Hardcastle et al. (1998)
3C223	0.1368	Hardcastle et al. (1998)	3C457	0.428	Goodlet et al. (2004)
3C223.1	0.1075	Hardcastle et al. (1998)	4C14.11	0.206	Hardcastle et al. (1998)
3C234	0.184	Leahy & Williams (1984)	4C14.27	0.392	Goodlet et al. (2004)
3C239	1.781	Liu & Pooley (1991b)	4C53.16	0.064	Garrington et al. (1991)
3C244	...	Leahy & Williams (1984)	4C74.16	0.81	Garrington et al. (1991)
3C247	0.748	Liu & Pooley (1991b)	6C0943+39	1.040	Goodlet et al. (2004)
3C252	1.100	Goodlet et al. (2004)	6C1011+36	1.040	Goodlet et al. (2004)
3C263.1	0.824	Liu & Pooley (1991b)	6C1129+37	1.060	Goodlet et al. (2004)
3C265	0.811	Goodlet et al. (2004)	6C1256+36	1.127	Goodlet et al. (2004)
3C266	1.275	Liu & Pooley (1991b)	6C1257+36	1.000	Goodlet et al. (2004)
3C267	1.140	Goodlet et al. (2004)			

Note. — Col.1. Source name. Col.2. Redshift. Col.3. Reference.

5.2. Hotspot Sizes

A strong correlation has previously been noticed between linear sizes of FR II radio galaxies and their hotspot sizes (e.g., Hardcastle et al. 1998). We find that our 13 FR II radio galaxies follow the same trend. In Fig. 1 we have plotted the hotspot size (of the brightest hotspot at each end) against the core-hotspot distance. Here we have considered only the 8 GHz measurements for the hotspot sizes from Hardcastle et al. (1998) and excluded the broad-line radio galaxies from the analysis. The size of an individual hotspot was defined as the geometric mean of the largest and smallest angular sizes (see Table 6).

Using the least absolute deviation method (implemented in the LADFIT routine in IDL), we fitted a linear model in the log-log space to the combined dataset and obtained a slope of 0.72 ± 0.06 . Note that by fitting a linear model to the combined dataset using chi-square minimization (implemented in the LINFIT routine in IDL), we obtain a slope of 0.52 ± 0.08 (Perucho & Martí (2003) have found the slope of the radio galaxy correlation to be 0.40 ± 0.11). However since the use of the chi-square error statistic can result in a poor fit due to an undesired sensitivity to outlying data, we consider the slope of the correlation to be close to 0.7. Thus the following relation holds for the hotspot-size r_h and core-hotspot distance l of the radio galaxy: $r_h \propto l^{0.7}$.

This correlation provides support for suggestions that the hotspot sizes scale with source linear size (see Hardcastle et al. 1998; Laing 1989; Bridle et al. 1994). This is consistent with the hotspot maintaining ram pressure balance as the source propagates through a medium with declining ambient density (Carvalho & O’Dea 2002b). Carvalho & O’Dea (2002a,b) discuss the results of two-dimensional axisymmetric numerical simulations of light, supersonic jets propagating into different density atmospheres and compare them with the predictions of three types of self-similar models. Of the self-similar models discussed, type I corresponds to the jet moving with a constant speed in a constant density atmosphere (e.g., Begelman & Cioffi 1989; Daly 1990); the type II model corresponds to jet motion in a medium where the ambient density falls off as d^{-2} (e.g., Daly 1990), where d is the distance from the source; while the type III model assumes a power-law density distribution with an exponent δ (e.g., Kaiser & Alexander 1997).

Following the relations between hotspot size, expansion time and the core-hotspot distance for type III models in Carvalho & O’Dea (2002a), *i.e.*, $r_h^2 \propto t^{(\delta+4)/(5-\delta)}$ and $l \propto t^{3/(5-\delta)}$, the derived exponent of 0.7 for the $r_h - l$ relation translates to a δ of 0.2. This implies that the jet propagates in a nearly constant ambient density medium ($\rho_a \propto d^{-0.2}$). This inference is consistent with the sources being located in the cores of protoclusters or clusters of galaxies, which have a roughly constant ambient gas density. Indeed, a couple of our 13 FR II radio galaxies seem to reside in such environments (see notes on individual sources in

the Appendix). This is supported by the previous studies of Cygnus A (Carilli et al. 1991), 3C295 (Perley & Taylor 1991), and the study of Wellman et al. (1997). Finally, with a δ of 0.2, the hotspot advance speed is proportional to $t^{-0.4}$, thereby implying a decelerating source.

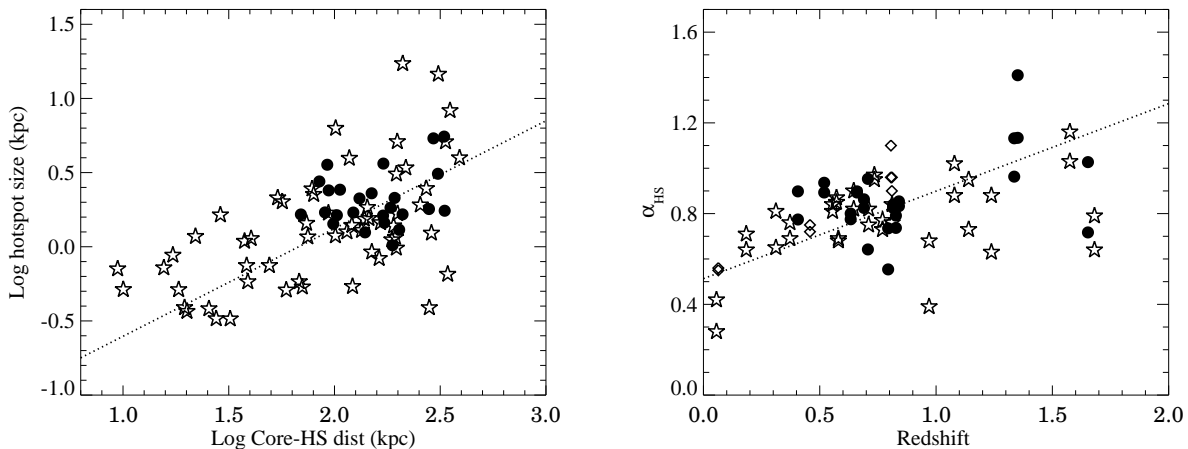


Fig. 1.— (Left) Log-log plot of the hotspot size versus the core-hotspot distance of the sources. Filled circles denote our sample FRII sources; open stars denote radio galaxies from Hardcastle et al. (1998). The slope of the correlation is ~ 0.7 . (Right) The hotspot spectral index versus redshift. The filled circles denote the hotspots for our 13 FRII sources, open stars are hotspot values from Leahy et al. (1989) while diamonds are from Garrington et al. (1991). The slope of the correlation is ~ 0.4 .

5.3. Spectral index vs. Redshift for Hotspots and Lobes

The hotspot spectral index (α_{HS}) is found to strongly correlate with redshift (z) – the spectra become steeper at higher redshifts (Fig. 1). This is consistent with the findings of Wellman et al. (1997); Dennett-Thorpe et al. (1999); Blundell et al. (1999) and Ishwara-Chandra & Saikia (2000). We find that the following approximate relation holds – $\alpha_{HS} \propto z^{0.4}$, with the absolute deviation in the exponent being ~ 0.03 . Note that the α_{HS} for our sources and from Garrington et al. (1991) have been estimated between 1.4 and 5 GHz, while the spectral index from Leahy et al. (1989) were derived between 151 MHz and 1.4 GHz. Excluding the data from Leahy et al. (1989) yields a slope of 0.43 ± 0.04 . The chi-square minimization method (LINFIT in IDL) results in a slope of 0.22 ± 0.05 for all the data, and 0.26 ± 0.07 when the data from Leahy et al. (1989) is excluded.

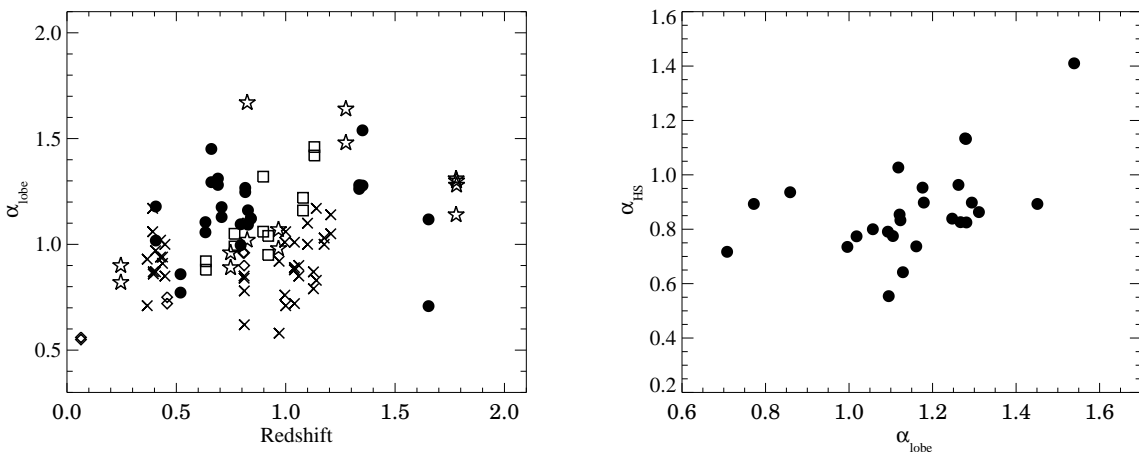


Fig. 2.— (Left) The lobe spectral index versus redshift. The filled circles denote our 13 radio galaxies, stars are galaxies from Liu & Pooley (1991b), squares from Pedelty et al. (1989), crosses from Goodlet et al. (2004), diamonds from Garrington et al. (1991). (Right) Hotspot spectral index versus lobe spectral index for our 13 FR II radio galaxies.

A correlation between spectral index and redshift is already well established for the integrated extended emission in FR II galaxies (e.g., Laing & Peacock 1980; Chambers et al. 1990; Athreya & Kapahi 1999; De Breuck et al. 2000). In Fig. 2, we have plotted the $z - \alpha$ correlation for our combined radio galaxy dataset. We do not find a correlation between the spectral index *difference* between the lobes and redshift, consistent with Goodlet & Kaiser (2005).

It has been pointed out that although a simple redshifting of the curved spectrum contributes to the $z - \alpha$ relation (e.g., Gopal-Krishna 1988; Lacy et al. 1993), it cannot account for the whole effect (e.g., Lacy et al. 1993; Blundell et al. 1999). It has been proposed that the hotspot spectral index is affected by inverse-Compton cooling owing to scattering with microwave background photons, which is a strong function of redshift (e.g., Rees & Setti 1968; Krolik & Chen 1991; Wellman et al. 1997). It has also been suggested that enhanced synchrotron losses in more powerful hotspots could also produce a spectral steepening at higher luminosity (e.g., Blundell et al. 1999; Dennett-Thorpe et al. 1999). Blundell et al. (1999) had examined three complete samples with successively fainter flux-limits, in order to break the luminosity-redshift degeneracy. They reached the conclusion that the rest-frame spectral indices have a stronger dependence on luminosity than on redshift, except at GHz frequencies. Based on the finding that the extremely steep-spectrum radio galaxies in the local universe inevitably reside at the centres of rich galaxy clusters (e.g., Baldwin & Scott 1973), Klammer et al. (2006) have postulated that $z - \alpha$ correlation could be a result of a

higher fraction of radio galaxies being located, as a function of redshift, in environments with densities similar to nearby rich clusters.

The hotspot spectral index correlates with the lobe spectral index (Fig. 2 Right). Further, the lobe spectral index is systematically steeper than the hotspot spectral index. These two results provide support to the spectral aging model in the radio lobes. Electrons are injected into the lobe with the spectral index of the hotspots. They subsequently age, making the spectra steeper.

5.4. The Rotation Measures and Dispersion

The mean rotation measure (RM) across the lobes of 11 of our 13 FRIIs varies from ~ 10 – 80 rad m^{-2} . On comparison with integrated RM measurements of Simard-Normandin et al. (1981), we find that our observed RM values are comparable to that expected from our Galaxy. The error in the rotation measure is typically less than 5 rad m^{-2} . The rotation measure dispersion (σ_{RM}) is typically less than 20 rad m^{-2} for our sources. For two of the sources with σ_{RM} greater than 30 rad m^{-2} , *viz.*, 3C13 and 3C470, large systematic errors were probably present in their bright hotspots.

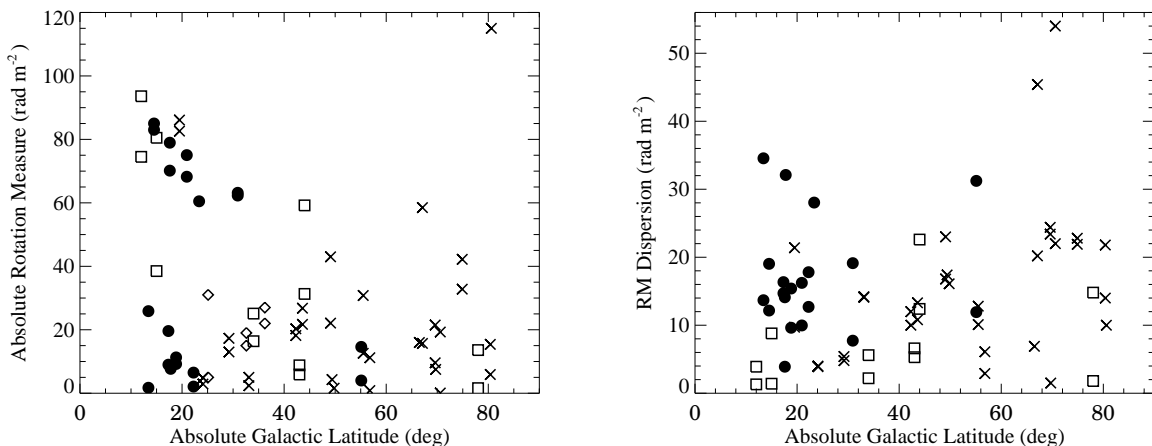


Fig. 3.— (Left) The absolute mean rotation measure for each of the two radio lobes versus the absolute Galactic latitude. (Right) The rotation measure dispersion in the two lobes versus the absolute Galactic latitude. Filled circles denote our sample FRII radio galaxies, stars and crosses denote radio galaxies from Liu & Pooley (1991b) and Goodlet et al. (2004), respectively, while squares and diamonds are galaxies from Pedelty et al. (1989) and Garrington et al. (1991), respectively.

Pedelty et al. (1989) had found a weak correlation between the rotation measures across the radio lobes and source Galactic latitudes, with the higher values of rotation measure occurring at lower Galactic latitudes. We find that such a correlation is significant at the 99% level (Spearman-Rank and Kendall’s-tau correlation tests) for the combined radio galaxy dataset (Fig. 3). The rotation measure dispersion and Galactic latitude are not correlated (see Table 8). These results suggest that the large-scale rotation measure is likely dominated by the Galactic foreground, whereas the small-scale structure in rotation measure (σ_{RM}) is produced in the source and/or its environment for these relatively high latitude sources (eg., Kronberg et al. 1972; Simonetti et al. 1984; Leahy 1987).

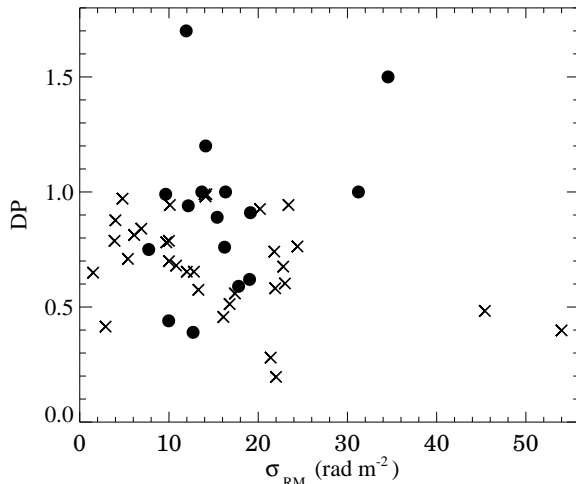


Fig. 4.— The two depolarization parameters DP and σ_{RM} plotted against each other. Filled circles denote our sample FRII radio galaxies while crosses denote radio galaxies from Goodlet et al. (2004).

Figure 4 shows the rotation measure dispersion plotted against the depolarization measure. We find no correlation between these two parameters (see Table 8). The lack of a correlation is consistent with the possibility that both the RM dispersion and depolarization result from a partially resolved foreground screen, associated with the radio source but in front of it (Tribble 1991; Johnson et al. 1995; Goodlet & Kaiser 2005). However this cannot be demonstrated unequivocally for these sources.

5.5. The Depolarization Asymmetry in Radio Lobes

Several strong correlations have been observed with lobe depolarization asymmetries in FRII radio galaxies. In sources with strong one-sided jets, the jet side tends to depolarize less rapidly with increasing wavelength, also referred to as the ‘Laing-Garrington’ effect (Laing 1988; Garrington et al. 1988). Further, the more depolarized lobe has a steeper spectrum (the ‘Liu-Pooley’ effect) and smaller angular distance between the core and the hotspot (Laing 1988; Liu & Pooley 1991a,b). Also, an asymmetry exists in the distribution of the emission-line gas in radio galaxies, with more emission-line gas lying on that side of the radio source for which the depolarization is stronger (McCarthy & van Breugel 1989).

Most of the 13 FRII radio galaxies have an arm-length ratio close to unity (Table 5). The misalignment angles are typically less than 8 degrees. Further, the radio core prominence in these 13 FRIIs is small, $-4.3 \leq \text{Log } R_c \leq -2.5$ (see Table 4). The small misalignment angles and radio core prominence suggest that our 13 FRII galaxies are largely plane-of-sky objects. This is consistent with the absence of bright radio jets in these radio galaxies. This makes them useful for a spectral aging study (Paper II).

5.5.1. The Laing-Garrington effect

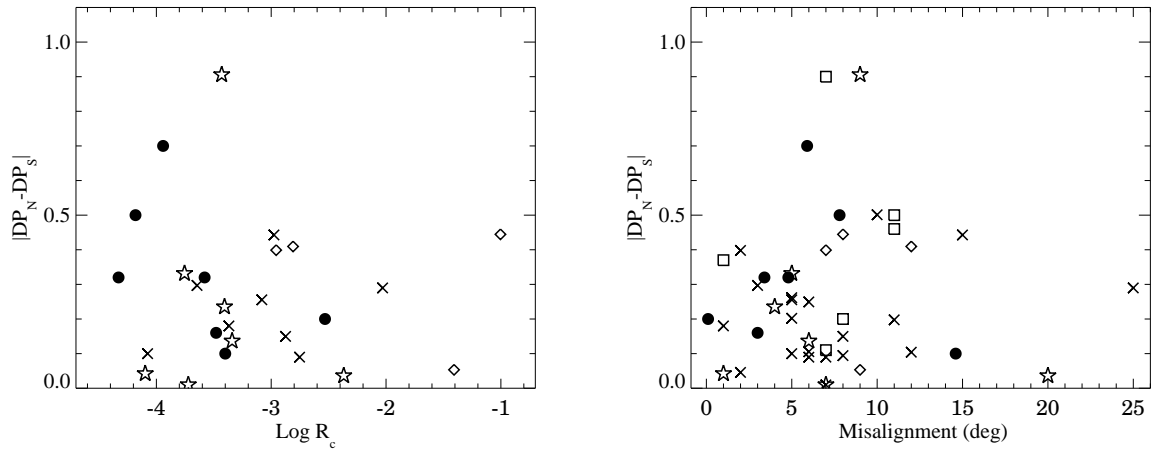


Fig. 5.— The absolute North-to-South lobe difference in depolarization versus the (Left) radio core prominence and (Right) misalignment angle. Filled circles denote our sample FRII radio galaxies, stars and crosses denote radio galaxies from Liu & Pooley (1991b) and Goodlet et al. (2004), respectively, while squares and diamonds are galaxies from Pedelty et al. (1989) and Garrington et al. (1991), respectively.

The jet-sidedness – depolarization relation cannot be unambiguously examined for our 6 FR II radio galaxies with mostly tentative jet detections. As the Laing-Garrington effect is suggested to be a consequence of Doppler-beaming, we examined the difference in lobe depolarization with respect to the (statistical) orientation-indicators – the radio core prominence and the misalignment angle, for the larger combined dataset (Fig. 5). We find that the lobe-to-lobe differences in depolarization are not correlated with either the radio core prominence or the misalignment angle. The lack of a correlation is consistent with the picture of these radio galaxies lying close to the plane of the sky. However it must be noted that Garrington et al. (1991) failed to see a correlation between depolarization asymmetry ratio and core strength, even in quasars. This is probably due to the large scatter in core prominence relation and the fact that this test is intrinsically less sensitive than one which compares quantities pertaining to two lobes. The lack of any correlation between the sidedness of faint jets with depolarization in a radio galaxy sample with weak jets has been noted by Laing (1993).

5.5.2. *The Liu-Pooley effect*

Liu & Pooley (1991a) found evidence for a correlation between the depolarization measure and lobe spectral index. They found that the radio lobe with the flatter spectrum is associated with lower depolarization. Among the 13 sample FRIIs, eleven sources have lobe depolarization measure and spectral index estimates, while only seven have depolarization estimates for both the lobes (see Table 5). Six out of these seven sources show lower depolarization in the lobe with the flatter spectral index. We examined the Liu-Pooley correlation with the combined dataset and found that the correlation is significant at the 99.99% significance level (Fig. 6). This is a significant improvement from the original radio galaxy (excluding quasars) correlation which was observed at the $\sim 80\%$ significance level (also see Ishwara-Chandra et al. 2001).

Liu & Pooley (1991a) have pointed out that the line-of-sight effects which derive from the orientation of the jet do not give a clear explanation for the $DP-\alpha$ correlation (see also Dennett-Thorpe et al. 1997). They concluded that differences in the medium surrounding the two radio lobes influence both the spectrum and the depolarization. A denser medium around one radio lobe would result in greater confinement of the lobe, thereby decreasing the expansion losses and possibly increasing the radiative losses, resulting in a steeper spectral index and greater depolarization. McCarthy et al. (1991) have indeed demonstrated that the emission-line gas is intrinsically asymmetric in powerful radio sources, and the differences in the density of the surrounding medium is sufficient to explain the observed arm-length ratios

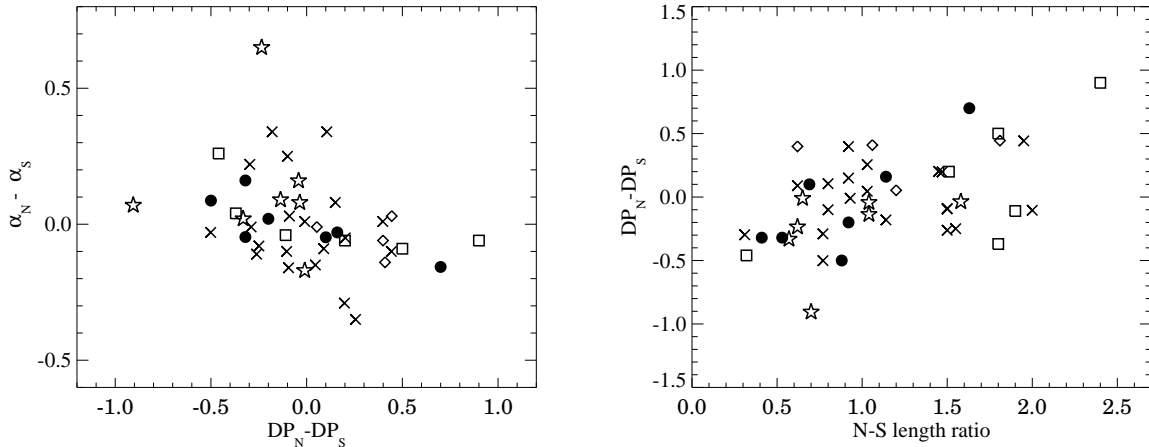


Fig. 6.— (Left) The North-to-South lobe difference in the spectral index versus the depolarization parameter. (Right) The North-to-South lobe difference in depolarization versus the North-to-South arm-length ratio. Filled circles denote our sample FRII radio galaxies, stars and crosses denote radio galaxies from Liu & Pooley (1991b) and Goodlet et al. (2004), respectively, while squares and diamonds are galaxies from Pedelty et al. (1989) and Garrington et al. (1991), respectively.

in radio galaxies (however see Best et al. 1995). We do find the presence of the “alignment effect” (McCarthy 1993), in 4 of our 13 FRII radio galaxies (see Notes in Appendix A).

With the intention of singling out factors that could contribute to the $DP - \alpha$ correlation, we examined the dependence of lobe depolarization and spectral index with (possible) orientation and environmental indicators. We find that the lobe depolarization difference is correlated with the North to South arm-length ratio (see Fig. 6), (as found by Pedelty et al. 1989; Laing 1996), in the sense that the shorter side of the source is more depolarized. This is in keeping with the idea of greater confinement around the shorter lobe by the source environment, which leads to greater depolarization (Liu & Pooley 1991b). We also find a tentative correlation between the difference in the lobe depolarization and the difference in axial ratios at a significance level greater than 99.8% (see Fig. 7). No trend is observed between the depolarization and axial ratio taken for each lobe separately. More data are clearly required to re-examine these relations. The trend between lobe depolarization difference and the axial ratio difference implies that shorter and/or fatter lobes are more depolarized. Again this is consistent with the picture of greater confinement around the lobes by the source environment, which gives rise to fatter lobes and depolarization.

We find that the absolute lobe-to-lobe difference in spectral index does not correlate with

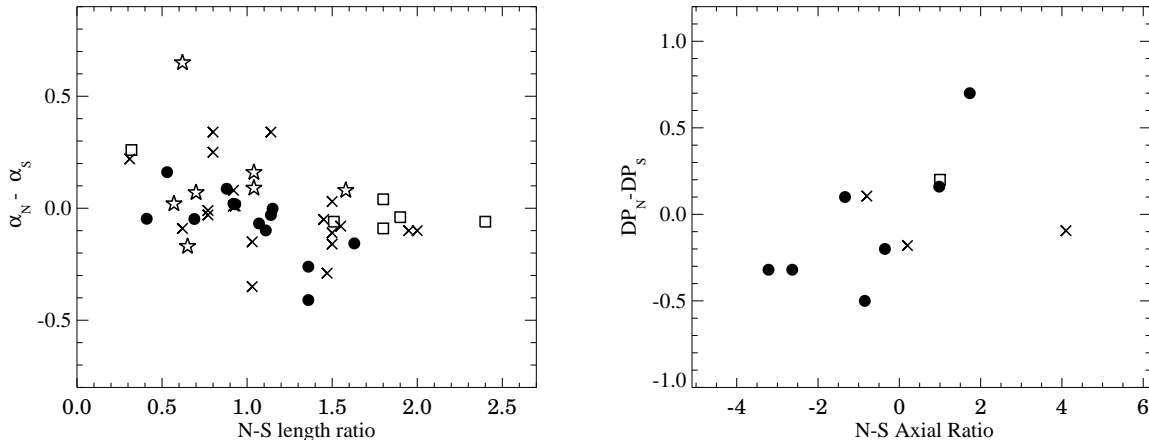


Fig. 7.— (Left) The North-to-South lobe difference in the spectral index versus the North-to-South arm-length ratio. (Right) The North-to-South lobe depolarization difference versus the axial ratio difference between the radio lobes. More data are clearly required to re-examine this correlation. Filled circles denote our sample FRII radio galaxies, stars and crosses denote radio galaxies from Liu & Pooley (1991b) and Goodlet et al. (2004), respectively, while squares and diamonds are galaxies from Pedelty et al. (1989) and Garrington et al. (1991), respectively.

the misalignment angle but shows a marginal correlation with the radio core prominence – core-dominant sources seem to have smaller differences in their lobe spectral indices (see Fig. 8 and Table 8). However, if relativistic beaming was indeed present in these radio galaxies, one would expect a correlation in the opposite sense. We confirm the significant correlation of the lobe spectral index difference with the North to South arm-length ratio, ie., the shorter lobe has the steeper spectral index (Fig. 7).

5.6. Structural Asymmetries and Trends with Redshifts

Although the 13 FRIIs have largely symmetric structures, trends with structural asymmetries emerge when the larger combined dataset is considered (see Gopal-Krishna & Wiita 2004, for a review on structural asymmetries). We find a correlation between the arm-length ratio and misalignment angle at the 99.9% significance level for the combined radio galaxy sample (Fig. 10) - sources whose lobes are asymmetric in length show greater misalignment between the two sides. This effect has been previously observed by, for example, Macklin (1981) and Kapahi & Saikia (1982). This correlation could suggest that the environmen-

Table 8. Correlation Statistics

Property 1	Property 2	Spearman Statistic	Spearman Prob.	Kendall Statistic	Kendall Prob.
Significant Correlations					
r_h	l	0.537	1.6E-7	0.373	5.3E-7
α_{lobe}	z	0.355	0.0002	0.243	0.0003
α_{HS}	z	0.393	0.0007	0.299	0.0002
DP_N-DP_S	$\alpha_N - \alpha_S$	-0.466	0.001	-0.317	0.002
$\alpha_N - \alpha_S$	N-S Length ratio	-0.445	0.001	-0.296	0.003
AR	Q	-0.352	0.003	-0.250	0.002
DP_N-DP_S	N-S Length ratio	0.448	0.002	0.315	0.002
α_{HS}	α_{lobe}	0.508	0.007	0.361	0.009
Marginal Correlations					
Q	ζ	0.306	0.010	0.206	0.012
$ RM $	$ b ^\dagger$	-0.287	0.014	-0.205	0.011
DP_N-DP_S	AR_N-AR_S	0.669	0.024	0.550	0.018
DP	z	-0.237	0.024	-0.160	0.024
ζ	R_c	0.367	0.038	0.234	0.059
$ \alpha_N - \alpha_S $	R_c	-0.452	0.009	-0.308	0.013
No Correlations					
σ_{RM}	$ b ^\ddagger$	0.205	0.100	0.141	0.095
$\alpha_N - \alpha_S$	z	-0.162	0.275	-0.116	0.249
AR	ζ	-0.128	0.294	-0.084	0.308
DP	AR	0.167	0.414	0.132	0.341
$ DP_N-DP_S $	ζ	0.095	0.539	0.043	0.677
Q	R_c	-0.092	0.615	-0.060	0.624
ζ	z	-0.092	0.454	-0.065	0.431
$ DP_N-DP_S $	R_c	-0.122	0.550	-0.080	0.565
$ \alpha_N - \alpha_S $	ζ	-0.049	0.745	-0.034	0.734
DP_N-DP_S	z	-0.032	0.762	-0.028	0.695
DP	σ_{RM}	-0.014	0.919	-0.009	0.921
Q	z	0.002	0.981	0.012	0.882

Note. — The correlations arranged according to decreasing probability. Col.s 1 & 2: The parameters examined for a correlation - $|RM|$ = Absolute value of rotation measure, $|b|$ = Absolute Galactic latitude, DP = Depolarization, Q = Arm-length ratio, ζ = Misalignment angle, AR = Axial ratio, R_c = Radio core prominence, r_h = Hotspot size, l = Core-hotspot distance, α_{HS} = Hotspot spectral index between 1.4 and 5 GHz, α_{lobe} = Lobe spectral index between 1.4 and 5 GHz, z = Redshift. Col.s 3 & 5: Spearman’s (rho) and Kendall’s (tau) rank correlation coefficient. Col.s 4 & 6: Probability that the two properties in Col.s. 1 & 2 are not correlated, using Spearman’s (rho) and Kendall’s (tau) rank correlation tests, respectively. A small value indicates a significant correlation. \dagger The correlation is significant at the 99.99% significance level, when the single high RM value from Goodlet et al. (2004) is excluded. \ddagger There is no correlation (Spearman prob. = 0.196) when the two high σ_{RM} values from Goodlet et al. (2004) are excluded.

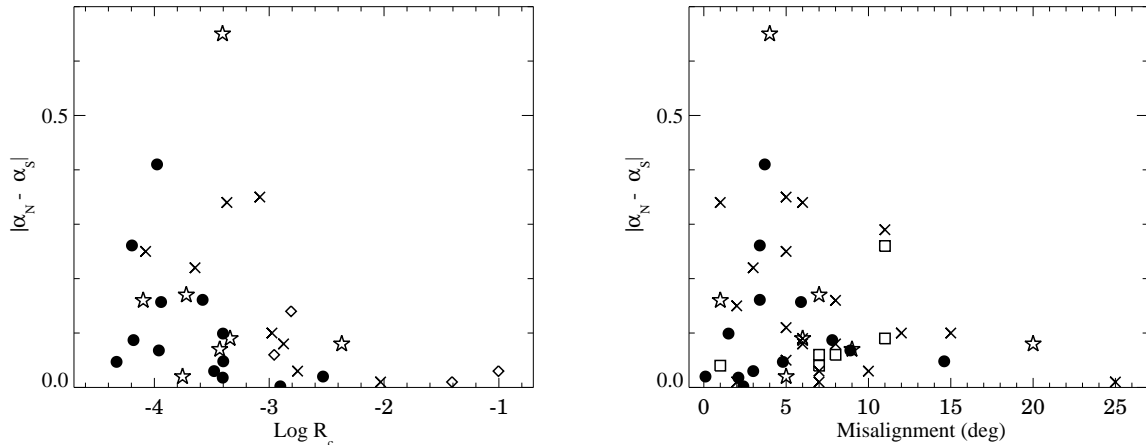


Fig. 8.— The absolute North-to-South lobe difference in the spectral index versus (Left) the radio core prominence and (Right) misalignment angle. Filled circles denote our sample FR II radio galaxies, stars and crosses denote radio galaxies from Liu & Pooley (1991b) and Goodlet et al. (2004), respectively, while squares and diamonds are galaxies from Pedelty et al. (1989) and Garrington et al. (1991), respectively.

tal asymmetries that give rise to the arm-length ratio could also be contributing to the misalignment angles in these radio galaxies, as also suggested by Macklin (1981).

The amount of misalignment also places a limit on the systematic jet axis stability and/or the dentist drill effect. If a source has two or more hotspots on one side of the source, and these two hotspots plus the core (or these two hotspots and the hotspot on the other side of the source) aligned to within some angle, say one degree, then the outflow axis must not change by more than an amount θ in a time δt . θ is the accuracy with which the hotspots and the core line up and δt is equal to or larger than the separation of the two hotspots on one side of the source divided by the speed of light. Thus if the separation of the two hotspots on one side is 10 kpc, and all of the hotspots line up to better than a degree, the wobble of the outflow axis must be less than about 10^{-14} rad s^{-1} . Wobbling could also produce substructure within the hotspots with a characteristic size that is proportional to the core-hotspot separation, and this could impact the overall hotspot size. As the misalignment angles are typically less than 10° in our 13 FR II radio galaxies, we infer that the wobble of the outflow axis in these sources is less than 10^{-13} rad s^{-1} . This argument is based on the relative positions of the hotspots and the core, and does not account for possible light travel time effects. These effects will be small if the source is close to the plane of the sky.

The radio core prominence is plotted with respect to the arm-length ratio and mis-

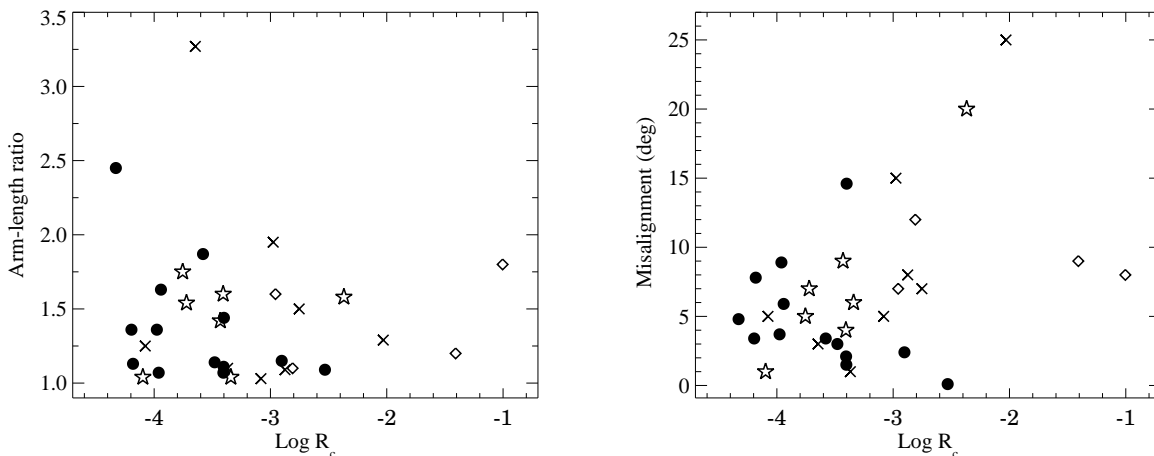


Fig. 9.— (Left) Arm-length ratio versus the radio core prominence parameter. (Right) Misalignment angle versus the radio core prominence. Filled circles denote our sample FRII radio galaxies, stars and crosses denote radio galaxies from Liu & Pooley (1991b) and Goodlet et al. (2004), respectively, diamonds are galaxies from Garrington et al. (1991).

alignment angle in Fig. 9. We observe a weak correlation between core prominence R_c and misalignment angle ζ , but none between R_c and arm-length ratio Q (see Table 8). The radio core prominence-misalignment angle ($R_c - \zeta$) correlation has previously been observed by, for example, Kapahi & Saikia (1982) and Hough & Readhead (1989). This correlation could be suggestive of the presence of relativistic beaming effects in the core due to orientation in the combined radio galaxy sample. On the other hand, there could be an environmental contribution to both the radio core prominence and misalignment angle. For example, the interaction of the jet as it is launched, with the surrounding nuclear environment could give rise to a brighter radio core along with changes in its direction of propagation, resulting in greater misalignment angles.

We find an anti-correlation between the arm-length ratios and axial ratios for the radio galaxies. In Fig. 10, we have plotted the axial ratios for each lobe separately, with respect to the arm-length ratio, for the combined radio galaxy dataset. The (anti)-correlation implies that sources which have a fatter lobe on one side, are also the most asymmetric in length. This effect is also clearly visible in the radio maps. If one radio lobe is shorter than the other, it could perhaps be due to a difference in the surrounding medium which slows down the expansion and confines one radio lobe preferentially. The overpressured radio plasma expands laterally when the jet meets resistance in the forward direction, thus producing fatter lobes. A larger variation in outflow direction can also lead to larger misalignment, fatter lobes and smaller axial ratios. The axial ratios and misalignment angles are however

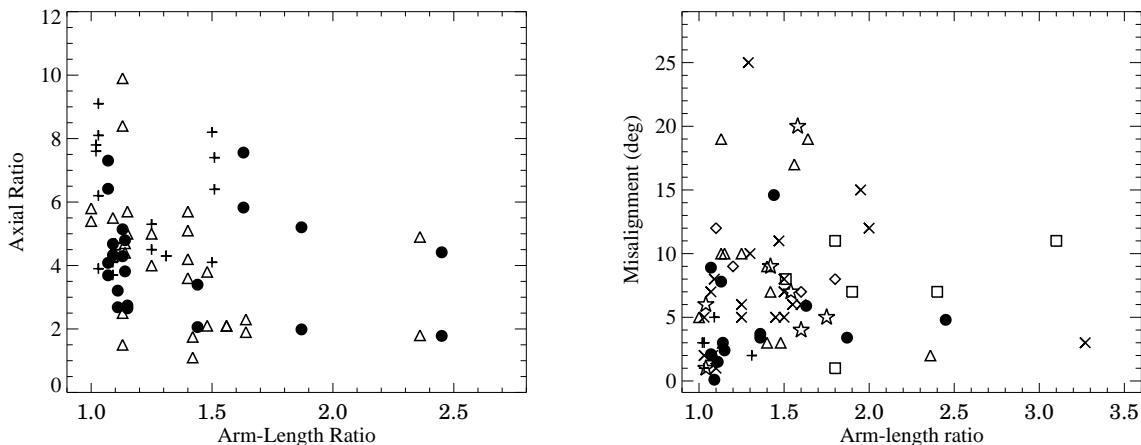


Fig. 10.— (Left) Axial ratio for each radio lobe versus the arm-length ratio. (Right) Misalignment angle versus arm-length ratio. The filled circles denote the radio galaxies from our sample, stars are data from Liu & Pooley (1991b), squares from Pedelty et al. (1989), crosses from Goodlet et al. (2004), diamonds from Garrington et al. (1991), triangles from Leahy & Williams (1984), and plus signs from Leahy et al. (1989).

not correlated (see Table 8). The lack of a correlation does not diminish the importance of the variation in outflow direction, because symmetric motions like the precession of the entire blackhole-double-jet system, could result in zero misalignment but still increase the axial ratios.

The anticorrelation between axial ratio and arm-length ratio and the correlation between depolarization and axial ratio (Figure 7) leads to an interesting new result. While it has been known for a long time that the shorter lobe is more depolarized in these radio galaxies, we find that shorter lobe is also the fatter one. This explains the correlation between depolarization and axial ratio. In a nutshell, we find that the shorter lobe is fatter, more depolarized and has a steeper spectrum.

We do not find any correlation between misalignment angle and redshift, nor between arm-length ratio and redshift (Fig. 11). Barthel & Miley (1988) had found a tentative correlation between misalignment angle and redshift but Kapahi & Kulkarni (1990) and Best et al. (1995) did not find such a correlation, consistent with our result.

We find a correlation between the lobe depolarization DP and redshift (Fig 12). Kronberg et al. (1972) and Goodlet & Kaiser (2005) have also found that the lobes of high redshift galaxies are more depolarized than their local counterparts. This would indicate that source environments vary with redshift, which would be consistent with the increasing alignment

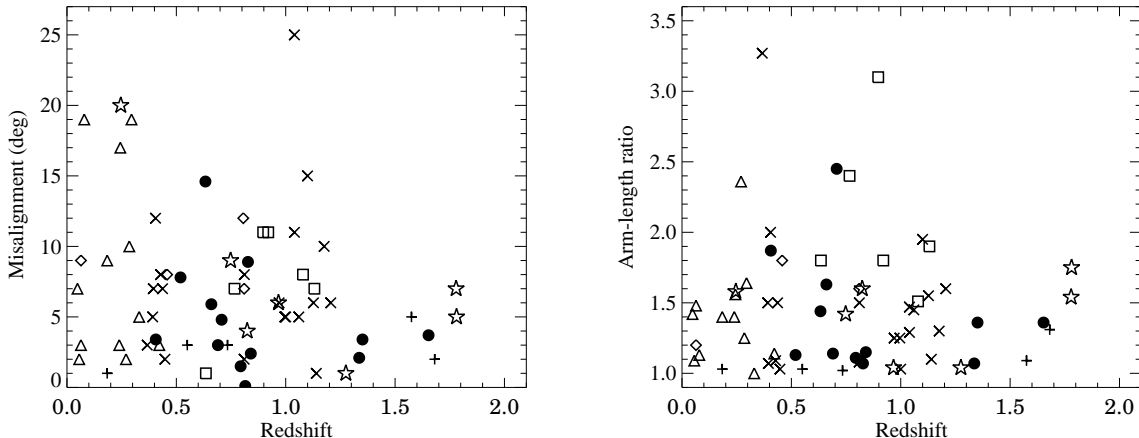


Fig. 11.— (Left) Misalignment angle and (Right) arm-length ratio versus redshift. The filled circles denote our 13 radio galaxies, stars are galaxies from Liu & Pooley (1991b), squares from Pedelty et al. (1989), crosses from Goodlet et al. (2004), diamonds from Garrington et al. (1991), triangles from Leahy & Williams (1984), and plus signs from Leahy et al. (1989). No correlation is observed between the parameters.

of emission line gas with the radio source with increasing redshift (e.g., McCarthy 1993; Best et al. 2000; Inskip et al. 2002; Privon et al. 2007). However, Morris & Tabara (1973) discovered that lobe depolarization showed a stronger dependence on the radio luminosity rather than on redshift. Goodlet & Kaiser (2005) have also found that lobe depolarization depends on both radio luminosity and redshift. We do not find a correlation between the depolarization difference between the lobes and redshift (see Table 8). Goodlet & Kaiser (2005) have reported the presence of this correlation, contrary to our finding. We note however that our sample-size is twice as large as Goodlet’s sample and spans a larger redshift range.

6. SUMMARY AND CONCLUSIONS

We have observed 13 large and powerful FRII radio galaxies with multiple arrays of the Very Large Array at the frequencies 330 MHz, 1.4, 5 and 8 GHz. Extended radio bridges are detected in all but two FRII galaxies (3C13 and 3C470). The rotation measures between 1.4 and 5 GHz are small, comparable to the expected Galactic contribution. The spectral index maps between 1.4 and 5 GHz show a gradual steepening of the radio spectra away from the hotspots with some spectral index variations superimposed, in agreement with previous

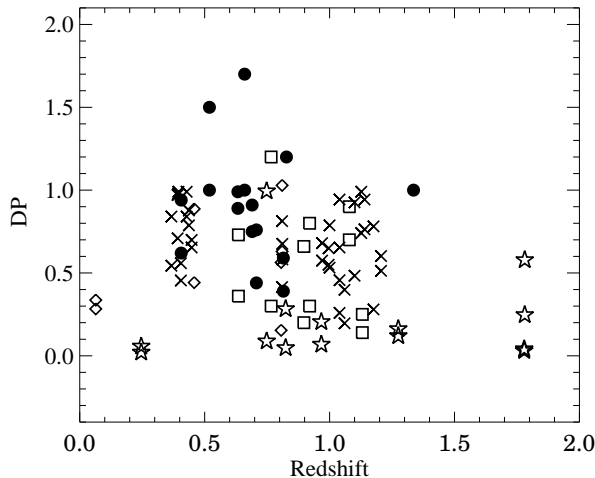


Fig. 12.— Depolarization for each radio lobe versus redshift. The filled circles denote our 13 radio galaxies, stars are galaxies from Liu & Pooley (1991b), squares from Pedelty et al. (1989), crosses from Goodlet et al. (2004), diamonds from Garrington et al. (1991).

studies.

The 13 FR II radio galaxies do not show the presence of bright jets and the core-to-lobe flux density ratio, *i.e.*, the radio core prominence is typically small ($-4 \leq \text{Log } R_c \leq -2$), indicating that these sources lie close to the plane of the sky. This is also consistent with the small misalignment angles which are less than 8° in all but one source. These characteristics make our sample useful for a spectral aging analysis, which will be presented in paper II.

We have supplemented our small sample with similar radio galaxy data gleaned from the literature and examined some well-known radio galaxy correlations.

1. We confirm that the hotspot size r_h is correlated with the core-hotspot distance l of the source and follows the relation $r_h \propto l^{0.7}$. This is consistent with the hotspot maintaining ram pressure balance as the source propagates through a medium with declining ambient density. This result is further consistent with a self-similar model of a jet propagating in a medium where the ambient density ρ_a falls off with distance from source d as $\rho_a \propto d^{-0.2}$. This could be due to the jets spanning hundreds of kiloparsecs in these sources, propagating through a roughly constant medium such as that which might be found in the core of a cluster or proto-cluster of galaxies.
2. The hotspot spectral index varies with redshift as $\alpha_{HS} \propto z^{0.4}$, consistent with previous studies on radio galaxies. A simple redshifting of the curved spectrum along with

an increase in inverse-Compton cooling due to scattering with microwave background photons at larger redshifts, could be responsible for this correlation. Alternatively, enhanced synchrotron losses in more powerful hotspots could be producing a spectral steepening at higher luminosity. This correlation could also be a result of a higher fraction of radio galaxies being located, as a function of redshift, in environments with densities similar to nearby rich clusters.

3. The hotspot spectral index is correlated with and flatter than the lobe spectral index, consistent with the assumptions of spectral aging models.
4. We find that the trend between the lobe depolarization and orientation, *i.e.*, the ‘Laing-Garrington effect’ is weak in these radio galaxies, suggesting that orientation/Doppler effects are not strong in them - these galaxies lie largely in the plane of the sky.
5. The correlation between lobe depolarization and lobe spectral index, *i.e.*, the ‘Liu-Pooley effect’, gains in statistical significance - radio lobes with a flatter spectrum exhibit lower depolarization.
6. The lobe depolarization difference is correlated with the North-to-South arm-length ratio, in the sense that the shorter side of the source is more depolarized. This strongly suggests that lobe depolarization depends significantly on environmental asymmetries in radio galaxies. The weak correlation between the lobe depolarization and the axial ratio difference is consistent with this inference.
7. In agreement with previous studies, we find that the lobe spectral index and depolarization are correlated with redshift. While the lobe spectral index – redshift correlation follows from points 2 and 3 above, the lobe depolarization – redshift correlation could suggest a variation in the source environments. However this effect cannot be differentiated from the dependence of depolarization on radio luminosity.
8. Based on the small misalignment angles in our 13 FR II radio galaxies, we infer that the wobble of the outflow axis in these sources is less than 10^{-13} rad s⁻¹.
9. We observe a weak correlation between the radio core prominence and misalignment angle but none between core prominence and arm-length ratio. This is consistent with both core prominence and misalignment angle being orientation indicators, and the arm-length ratio being more sensitive towards asymmetries in the environment. The radio core prominence and misalignment can however also be correlated if the inner jet interacts with the ambient medium, resulting in brighter radio cores and larger misalignment angles.

10. The arm-length ratio seems to be significantly correlated with the misalignment angle between the two sides of the radio source but anti-correlated with the axial ratio. This is again suggestive of environmental asymmetries close to the radio sources. Such asymmetries can cause a variation in the outflow direction which can result in larger misalignments. Variation in the jet direction can also result in fatter radio lobes and lower axial ratios.
11. We find that the shorter lobe is fatter, more depolarized and has a steeper spectrum.

To summarize, the FRII radio galaxy attributes can be influenced by many factors such as their local environment and asymmetries in the gas in the interstellar and intergalactic medium, and relativistic beaming effects. Changes in the outflow direction and variations in the beam power with time, may also be playing a role. Radio core prominence and misalignment angles can be used as statistical indicators of orientation while the arm-length and axial ratios can serve to highlight environmental asymmetries, in large radio galaxy samples. However the environmental contribution to the orientation-indicators, and the presence of variable motion of the outflow axis cannot be ignored.

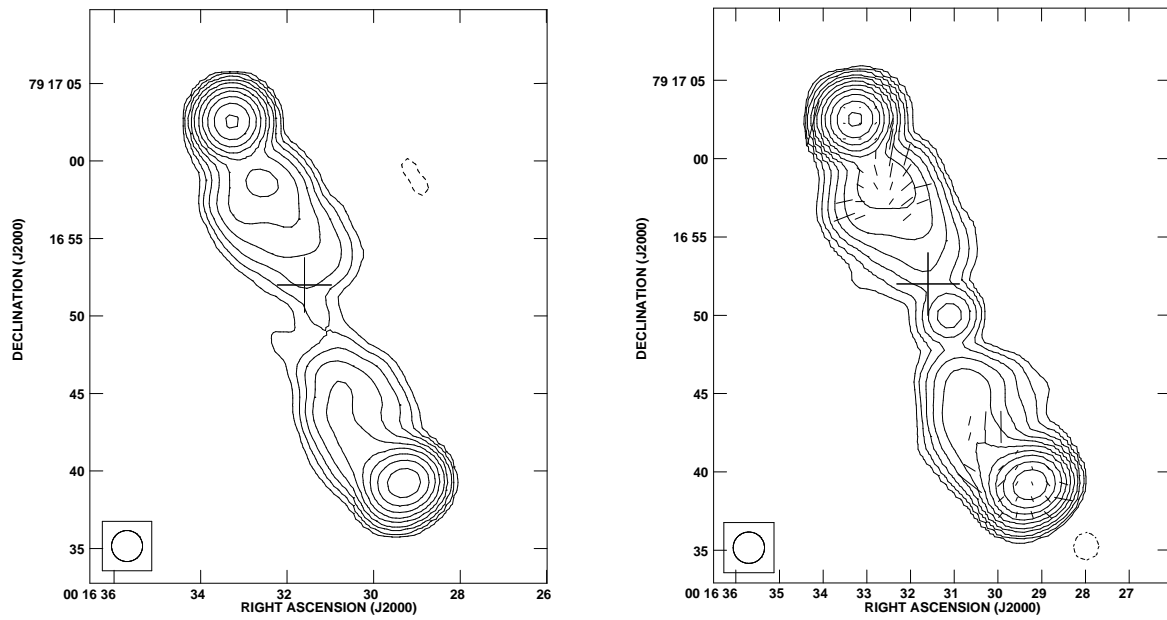


Fig. 13.— Total intensity image of 3C6.1 at (left) 1.66 GHz and (right) 4.86 GHz, at a resolution of $2''$ with fractional polarization vectors superimposed. The peak surface brightness and contour levels increasing in steps of 2 are (left) 1.2 Jy/beam, $(-0.17, 0.17, \dots, 90)\%$ of peak brightness, (right) 419.9 mJy/beam, $(-0.085, 0.085, \dots, 90)\%$ of peak brightness, $1''$ vector = 17% polarization.

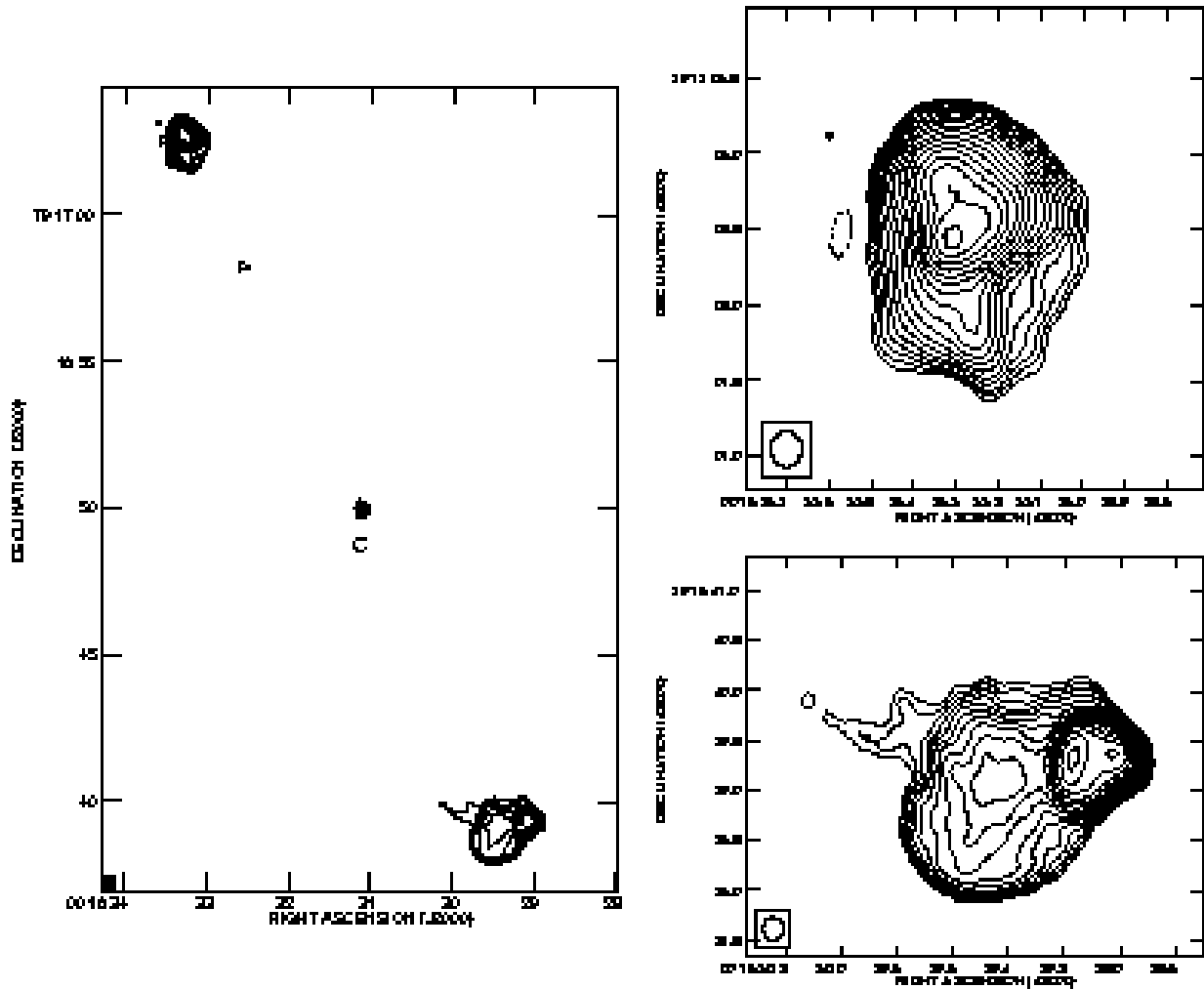


Fig. 14.— Total intensity image of 3C6.1 at 8.4 GHz. The peak surface brightness and contour levels increasing in steps of $2(\sqrt{2})$ for the closeup views of the hotspot regions) are 49.2 mJy/beam and $(-0.35, 0.35, \dots, 90)\%$ of peak brightness, respectively.

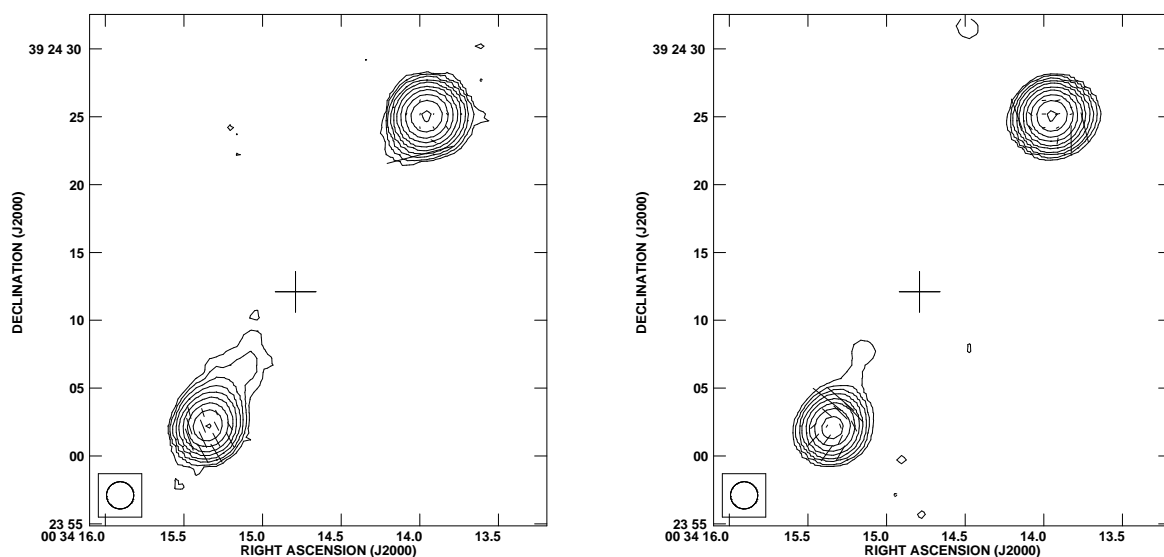


Fig. 15.— Total intensity image of 3C13 at (left) 1.46 GHz and (right) 4.86 GHz, at a resolution of $2''$ with fractional polarization vectors superimposed. The peak surface brightness and contour levels increasing in steps of 2 are (left) 1.06 Jy/beam, $(-0.17, 0.17, \dots, 90)\%$ of peak brightness, $1''$ vector = 7% polarization, (right) 270.0 mJy/beam, $(-0.17, 0.17, \dots, 90)\%$ of peak brightness, $1''$ vector = 7% polarization.

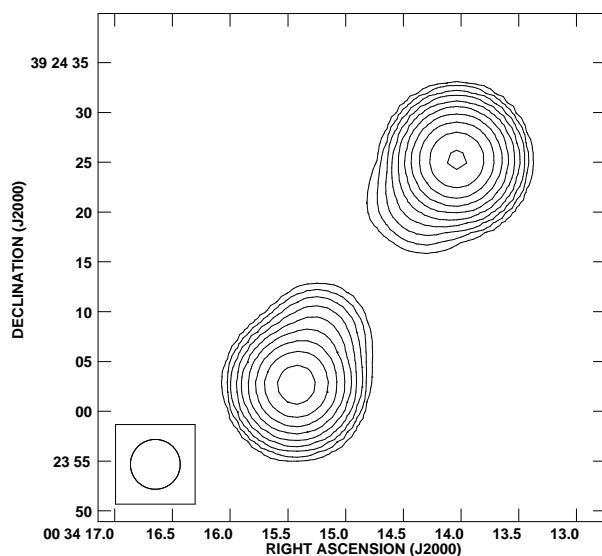


Fig. 16.— Total intensity image of 3C13 at 327.6 MHz. The peak surface brightness and contour levels increasing in steps of 2 are 4.3 Jy/beam, $(-0.17, 0.17, \dots, 90)\%$ of peak brightness.

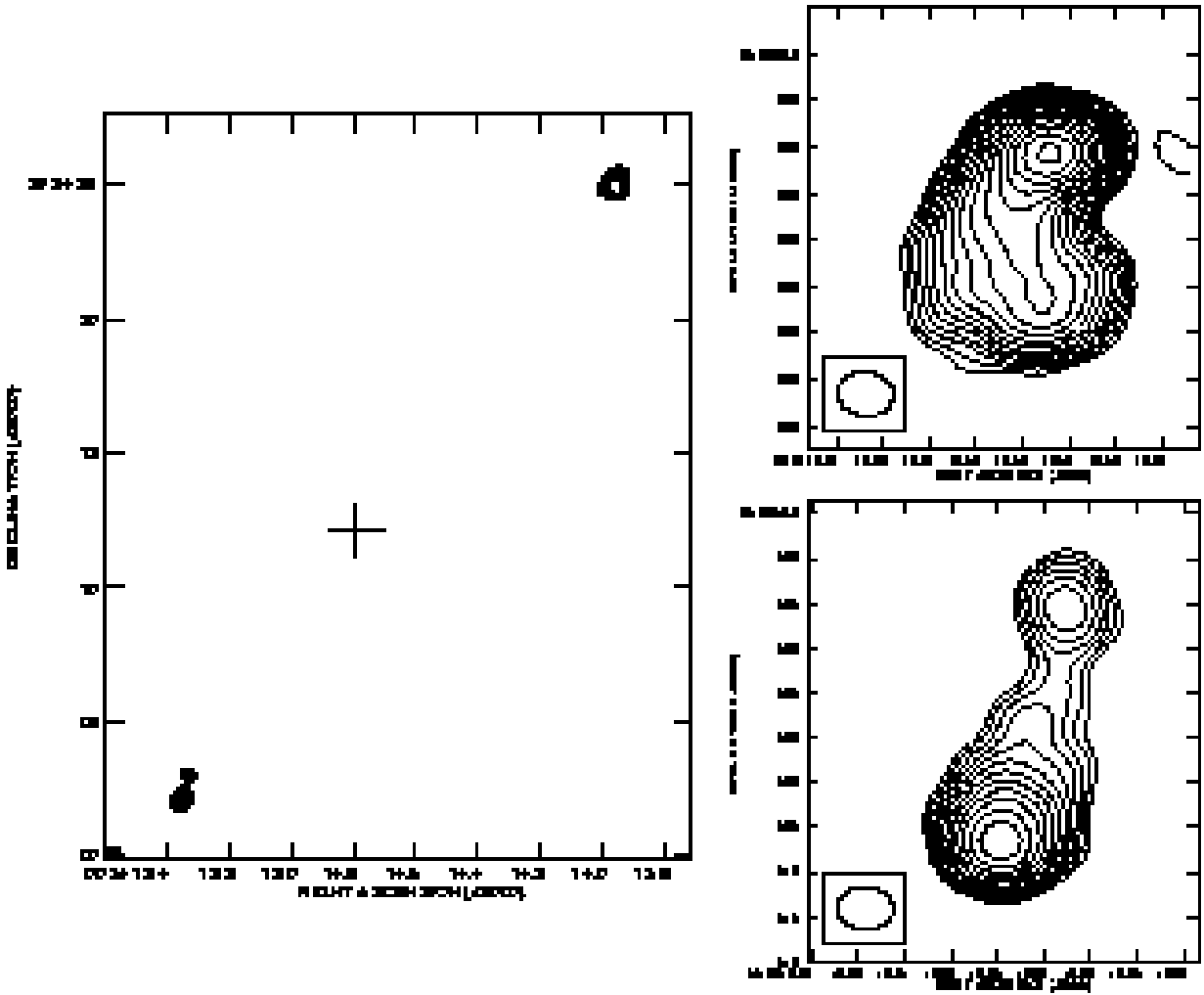


Fig. 17.— Total intensity image of 3C13 at 8.4 GHz. The peak surface brightness and contour levels increasing in steps of $2\sqrt{2}$ for the closeup views of the hotspot regions) are 60.3 mJy/beam, $(-0.7, 0.7, \dots, 90)\%$ of peak brightness.

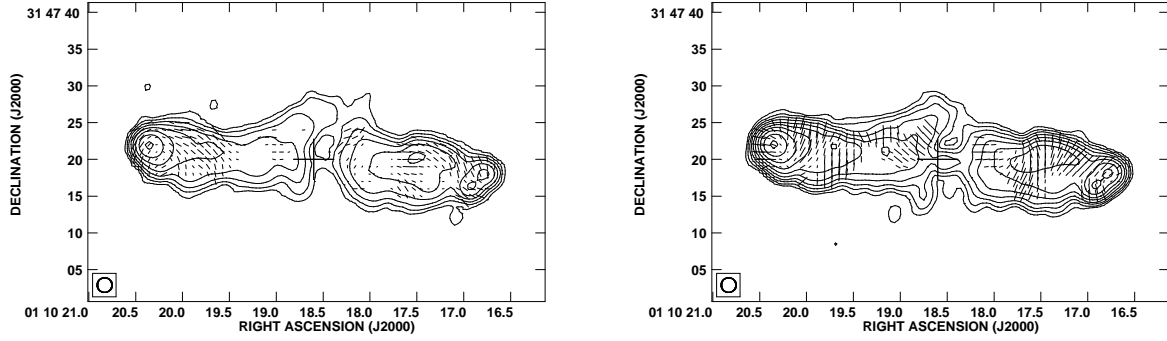


Fig. 18.— Total intensity image of 3C34 at (left) 1.66 GHz and (right) 4.86 GHz, at a resolution of $2''$ with fractional polarization vectors superimposed. The peak surface brightness and contour levels increasing in steps of 2 are (left) 135.5 mJy/beam, $(-0.7, 0.7, \dots, 90)\%$ of peak brightness, $1''$ vector = 20% polarization, (right) 57.8 mJy/beam, $(-0.17, 0.17, \dots, 90)\%$ of peak brightness, $1''$ vector = 17% polarization.

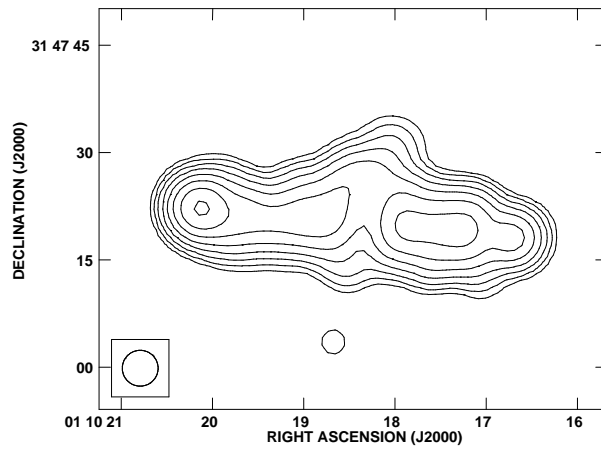


Fig. 19.— Total intensity image of 3C34 at 327.6 MHz. The peak surface brightness and contour levels increasing in steps of 2 are 913.8 mJy/beam, $(-0.7, 0.7, \dots, 90)\%$ of peak brightness

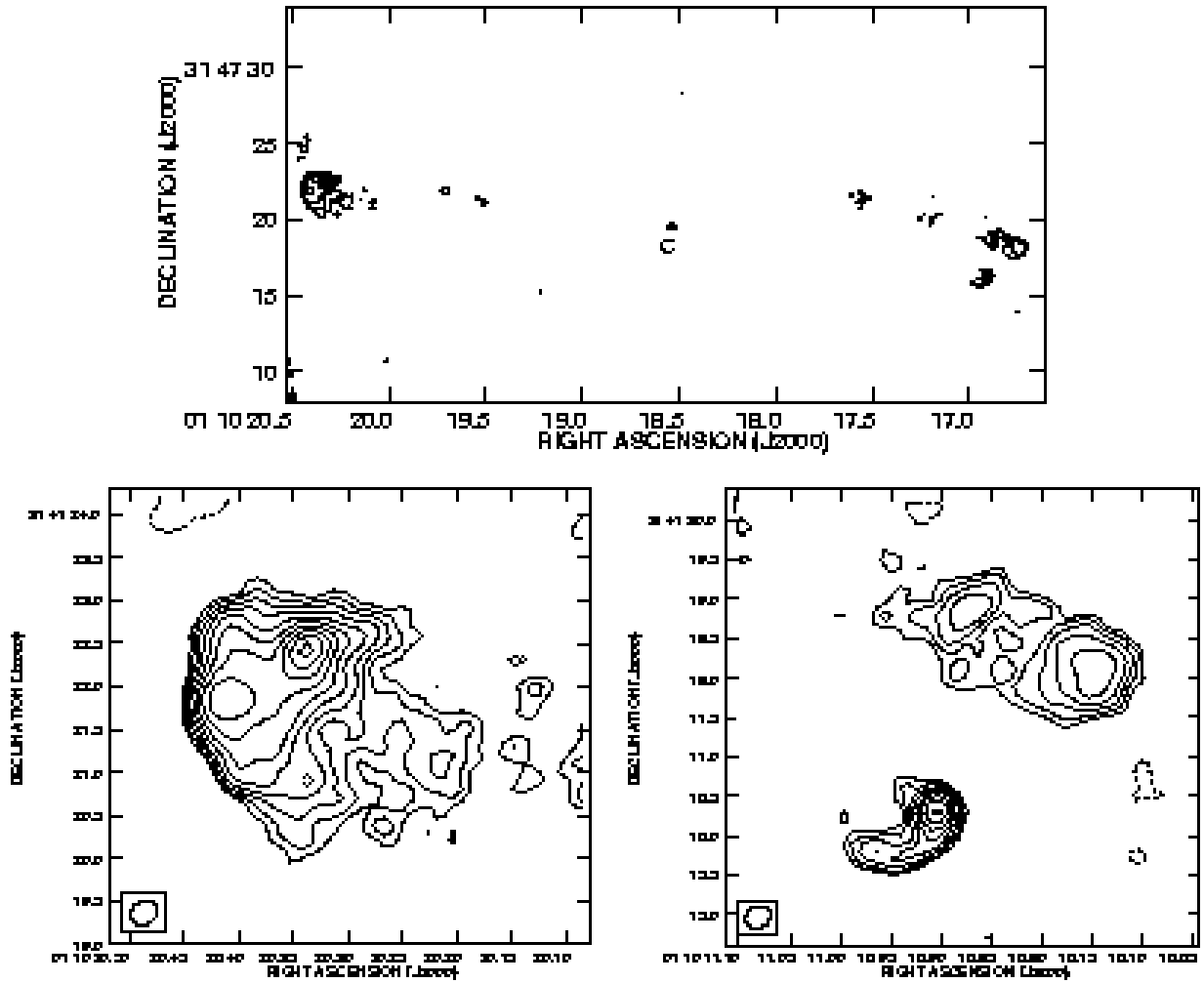


Fig. 20.— Total intensity image of 3C34 at 8.4 GHz. The peak surface brightness and contour levels increasing in steps of $2(\sqrt{2})$ for the closeup views of the hotspot regions) are 3.4 mJy/beam, $(-5.6, 5.6, \dots, 90)\%$ of peak brightness. The lowest contour level in the hotspot blowup is 4% of the peak brightness.

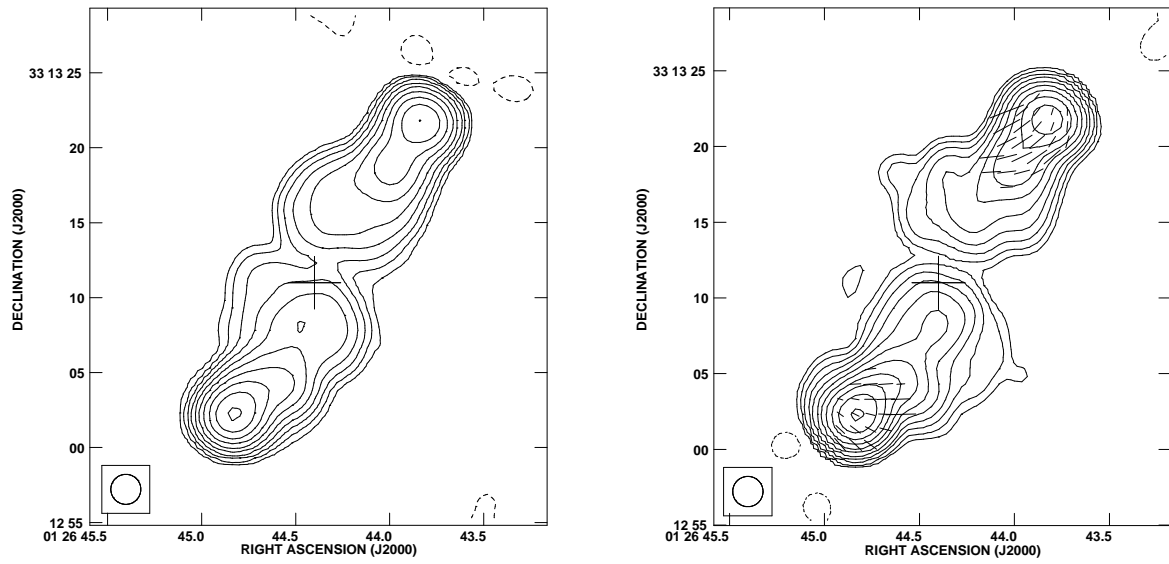


Fig. 21.— Total intensity image of 3C41 at (left) 1.34 GHz and (right) 4.86 GHz, at a resolution of $2''$ with fractional polarization vectors superimposed. The peak surface brightness and contour levels increasing in steps of 2 are (left) 977.0 mJy/beam, $(-0.17, 0.17, \dots, 90)\%$ of peak brightness, (right) 502.6 mJy/beam, $(-0.085, 0.085, \dots, 90)\%$ of peak brightness, $1''$ vector = 10% polarization.

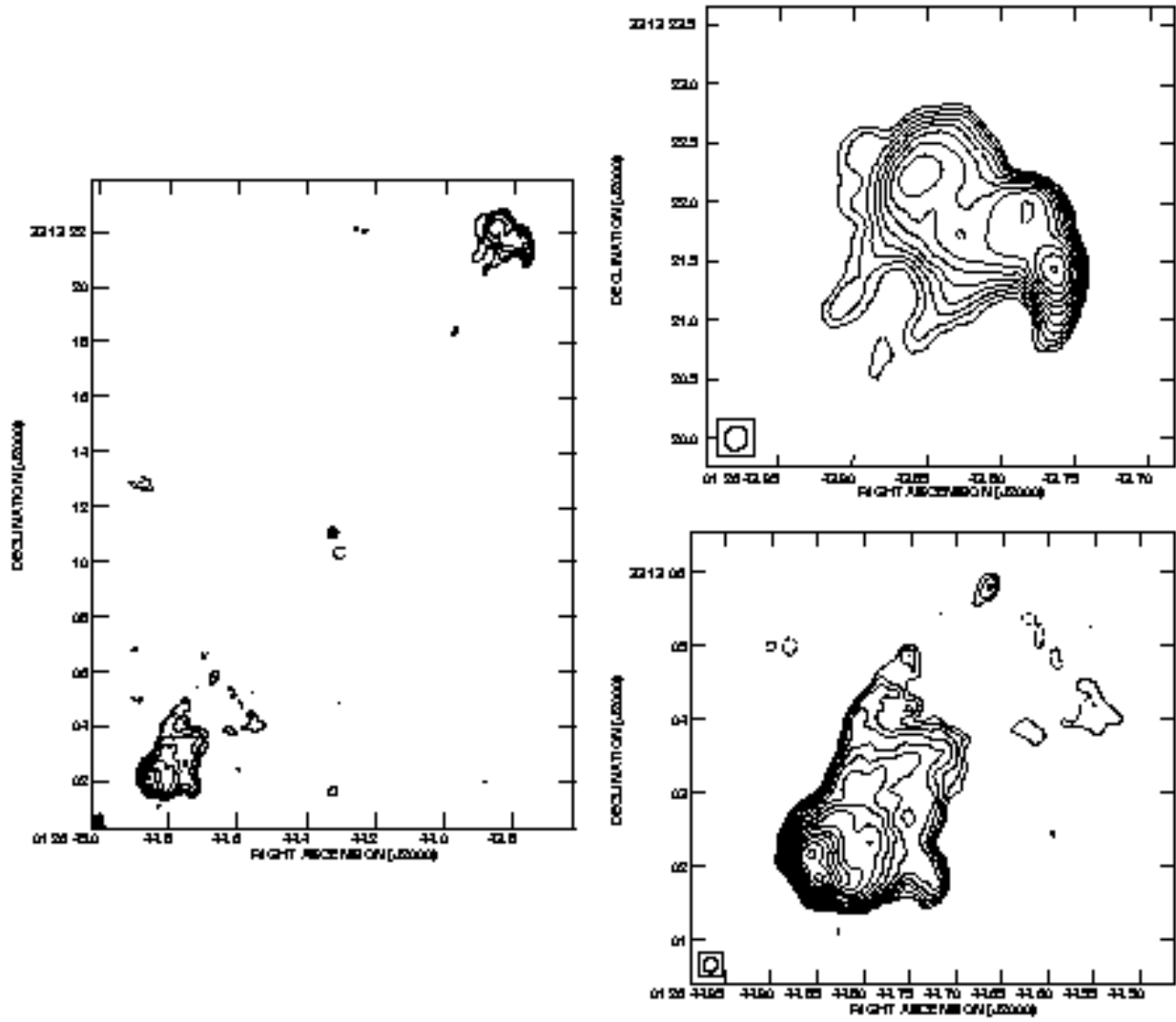


Fig. 22.— Total intensity image of 3C41 at 8.4 GHz. The peak surface brightness and contour levels increasing in steps of $2\sqrt{2}$ for the closeup views of the hotspot regions) are 38.2 mJy/beam and $(-0.7, 0.7, \dots, 90)\%$ of peak brightness, respectively. The lowest contour level in the hotspot blowup is 0.5% of the peak brightness.

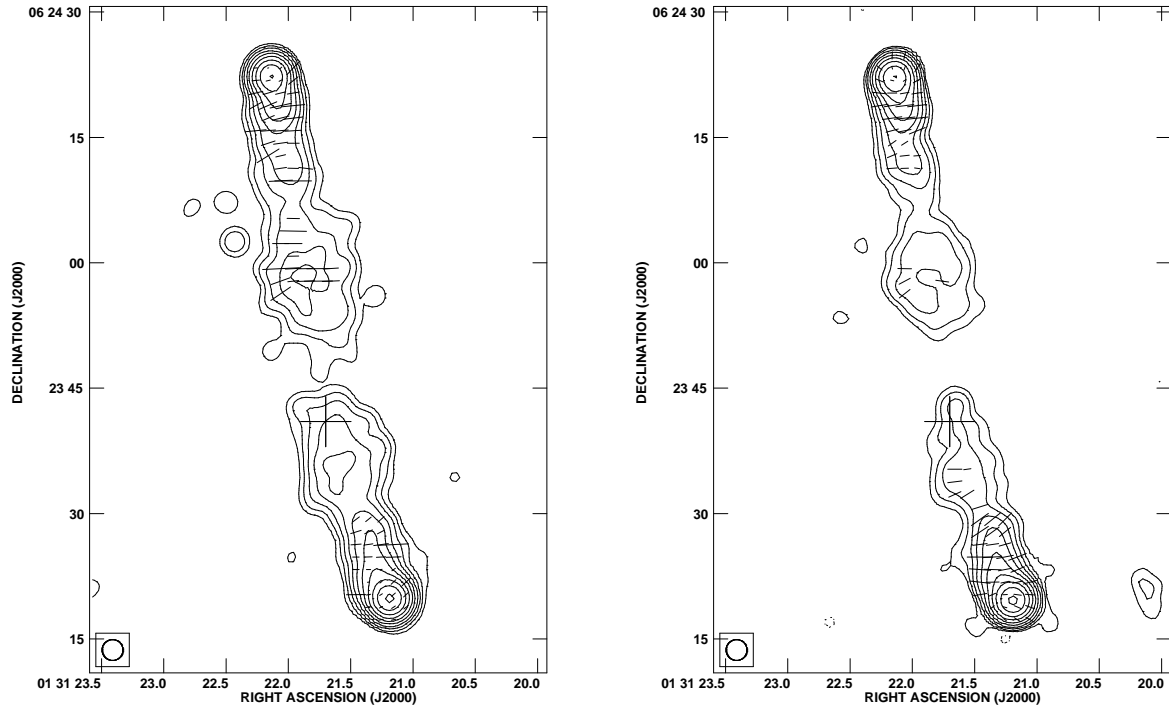


Fig. 23.— Total intensity image of 3C44 at (left) 1.66 GHz and (right) 4.86 GHz, at a resolution of $2.5''$ with fractional polarization vectors superimposed. The peak surface brightness and contour levels increasing in steps of 2 are (left) 432.1 mJy/beam, $(-0.17, 0.17, \dots, 90)\%$ of peak brightness, $1''$ vector = 13% polarization, (right) 136.1 mJy/beam, $(-0.17, 0.17, \dots, 90)\%$ of peak brightness, $1''$ vector = 10% polarization.

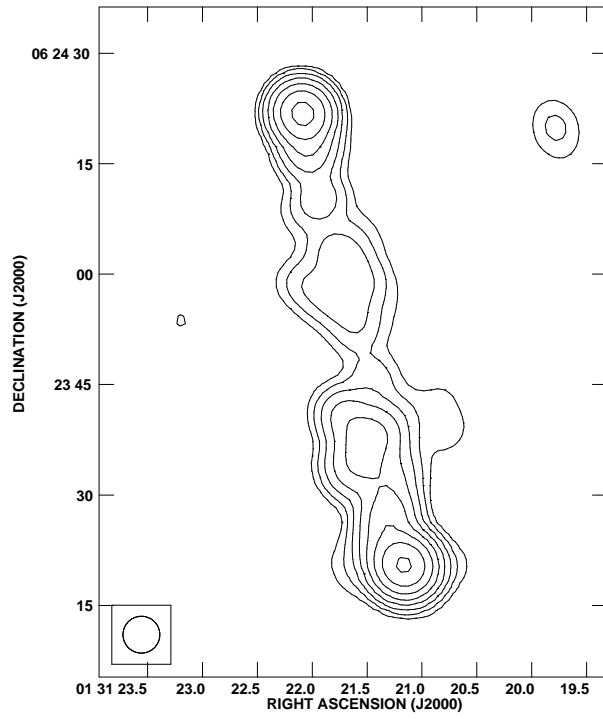


Fig. 24.— Total intensity image of 3C44 at 327.6 MHz. The peak surface brightness and contour levels increasing in steps of 2 are 1.6 Jy/beam, (-0.7,0.7,...,90)% of peak brightness.

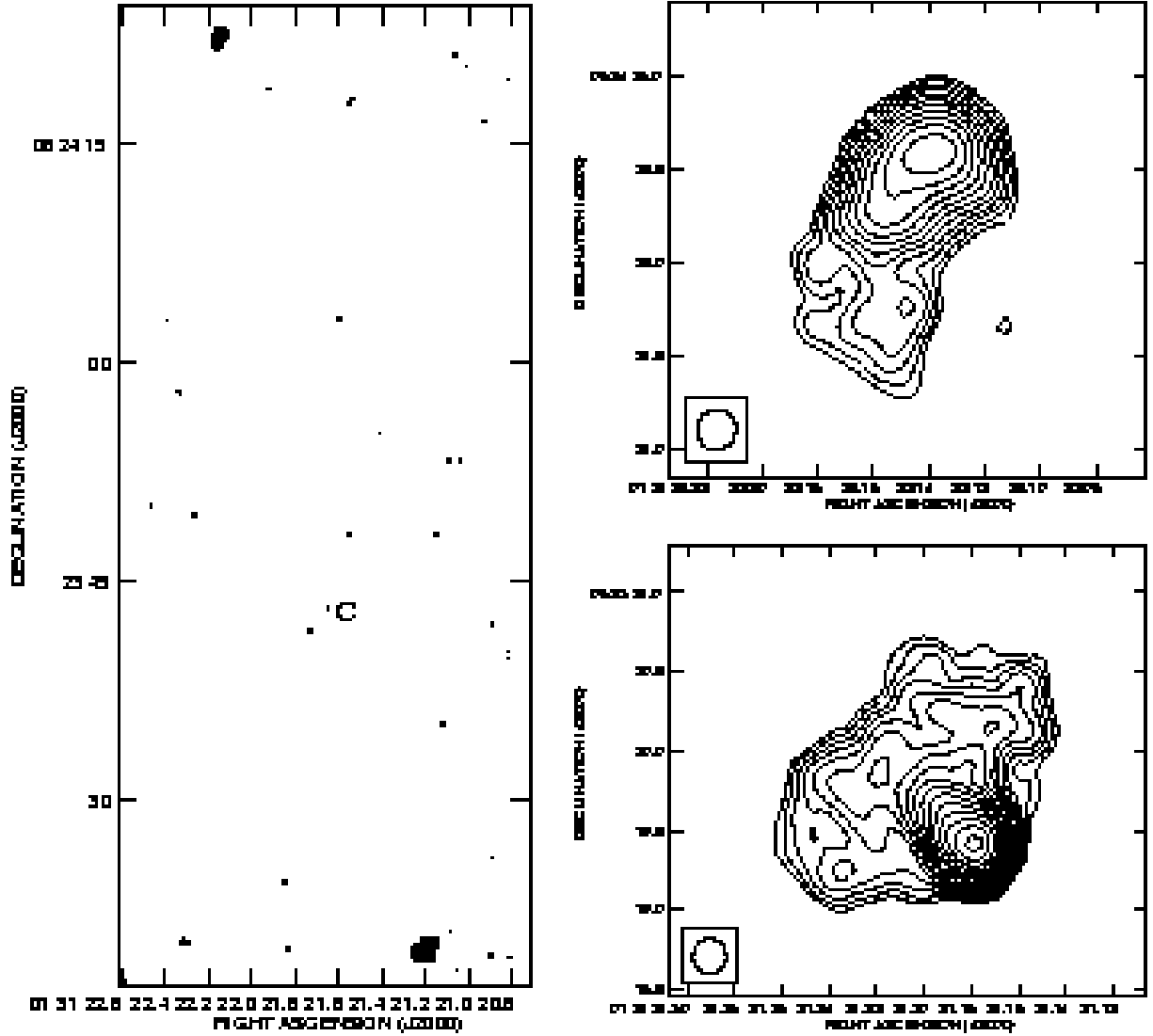


Fig. 25.— Total intensity image of 3C44 at 8.4 GHz. The peak surface brightness and contour levels increasing in steps of 2 ($\sqrt{2}$ for the closeup views of the hotspot regions) are 24.3 mJy/beam, $(-0.7, 0.7, \dots, 90)\%$ of peak brightness. The lowest contour level in the hotspot blowup is 0.5% of the peak brightness.

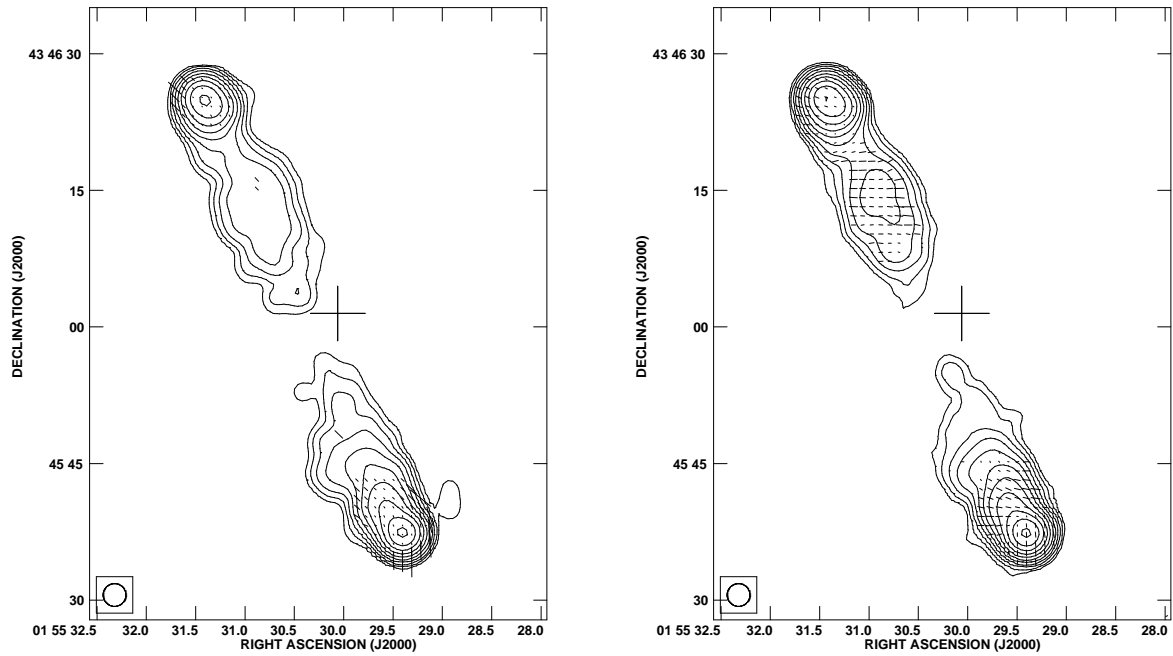


Fig. 26.— Total intensity image of 3C54 at (left) 1.34 GHz and (right) 4.86 GHz, at a resolution of $2.5''$ with fractional polarization vectors superimposed. The peak surface brightness and contour levels increasing in steps of 2 are (left) 581.9 mJy/beam, $(-0.17, 0.17, \dots, 90)\%$ of peak brightness, $1''$ vector = 25% polarization, (right) 227.8 mJy/beam, $(-0.085, 0.085, \dots, 90)\%$ of peak brightness, $1''$ vector = 25% polarization.

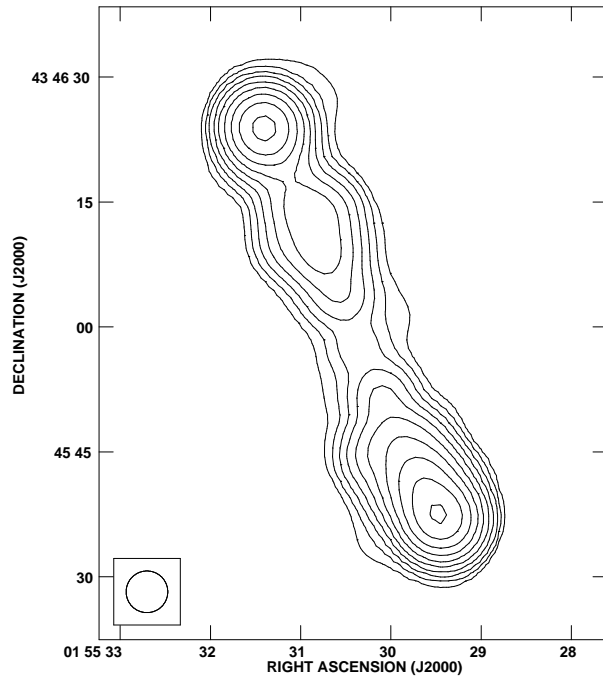


Fig. 27.— Total intensity image of 3C54 at 327.6 MHz. The peak surface brightness and contour levels increasing in steps of 2 are 2.1 Jy/beam, (-0.17,0.17,...,90)% of peak brightness

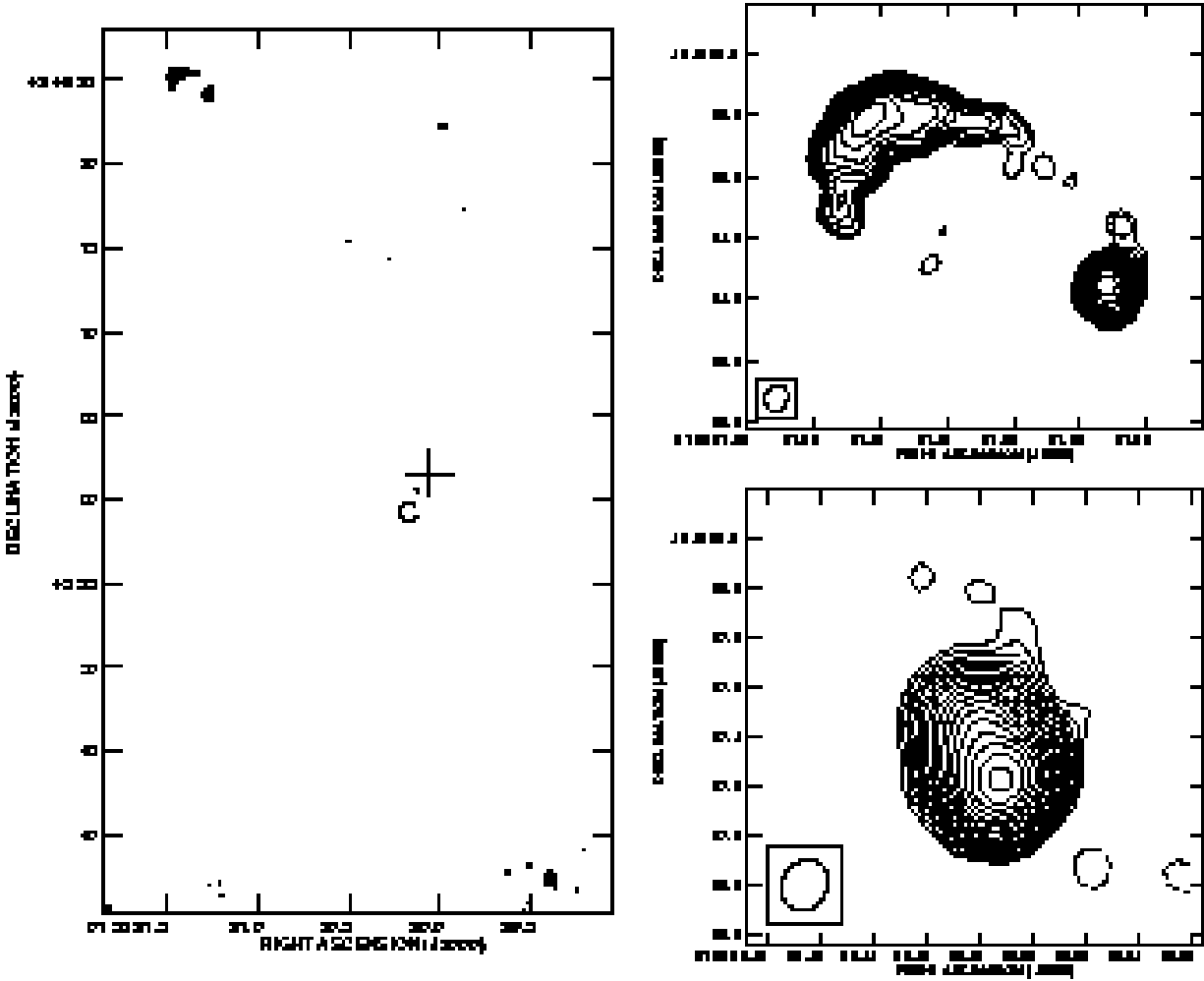


Fig. 28.— Total intensity image of 3C54 at 8.4 GHz. The peak surface brightness and contour levels increasing in steps of 2 ($\sqrt{2}$ for the closeup views of the hotspot regions) are 69.6 mJy/beam, $(-0.35, 0.35, \dots, 90)\%$ of peak brightness. The lowest contour level in the hotspot blowup is 0.25% of the peak brightness.

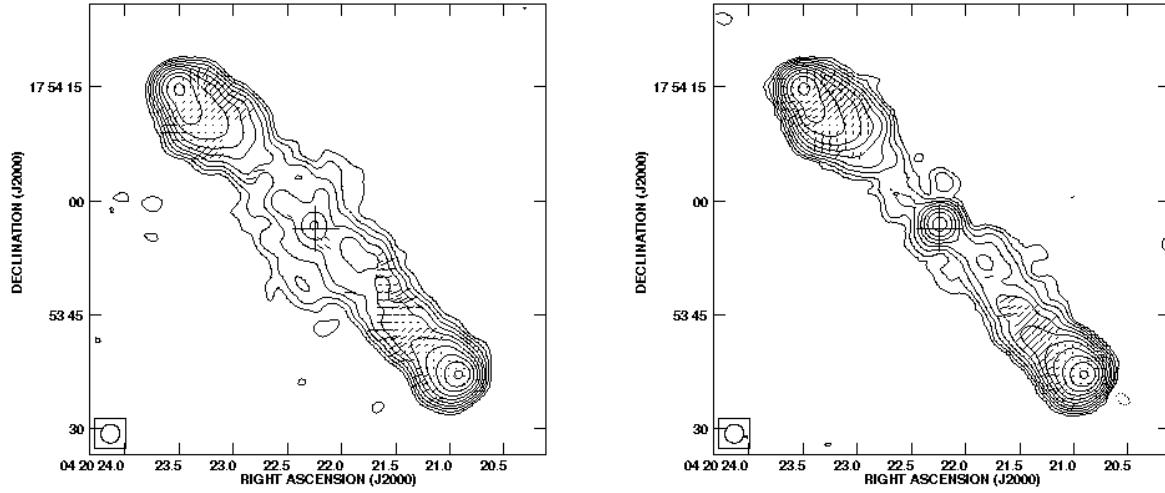


Fig. 29.— Total intensity image of 3C114 at (left) 1.66 GHz and (right) 4.86 GHz, at a resolution of $2.5''$ with fractional polarization vectors superimposed. The peak surface brightness and contour levels increasing in steps of 2 are (left) 203.7 mJy/beam, $(-0.17, 0.17, \dots, 90)\%$ of peak brightness, $1''$ vector = 17% polarization, (right) 69.5 mJy/beam, $(-0.085, 0.085, \dots, 90)\%$ of peak brightness, $1''$ vector = 17% polarization.

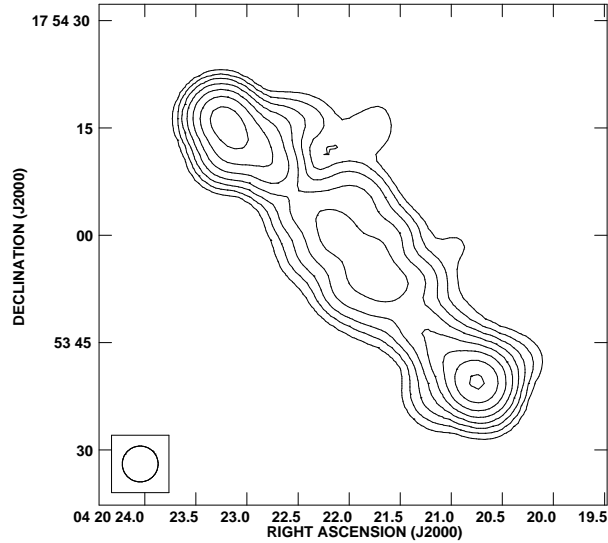


Fig. 30.— Total intensity image of 3C114 at 327.6 MHz. The peak surface brightness and contour levels increasing in steps of 2 are 898.5 mJy/beam, $(-0.7, 0.7, \dots, 90)\%$ of peak brightness

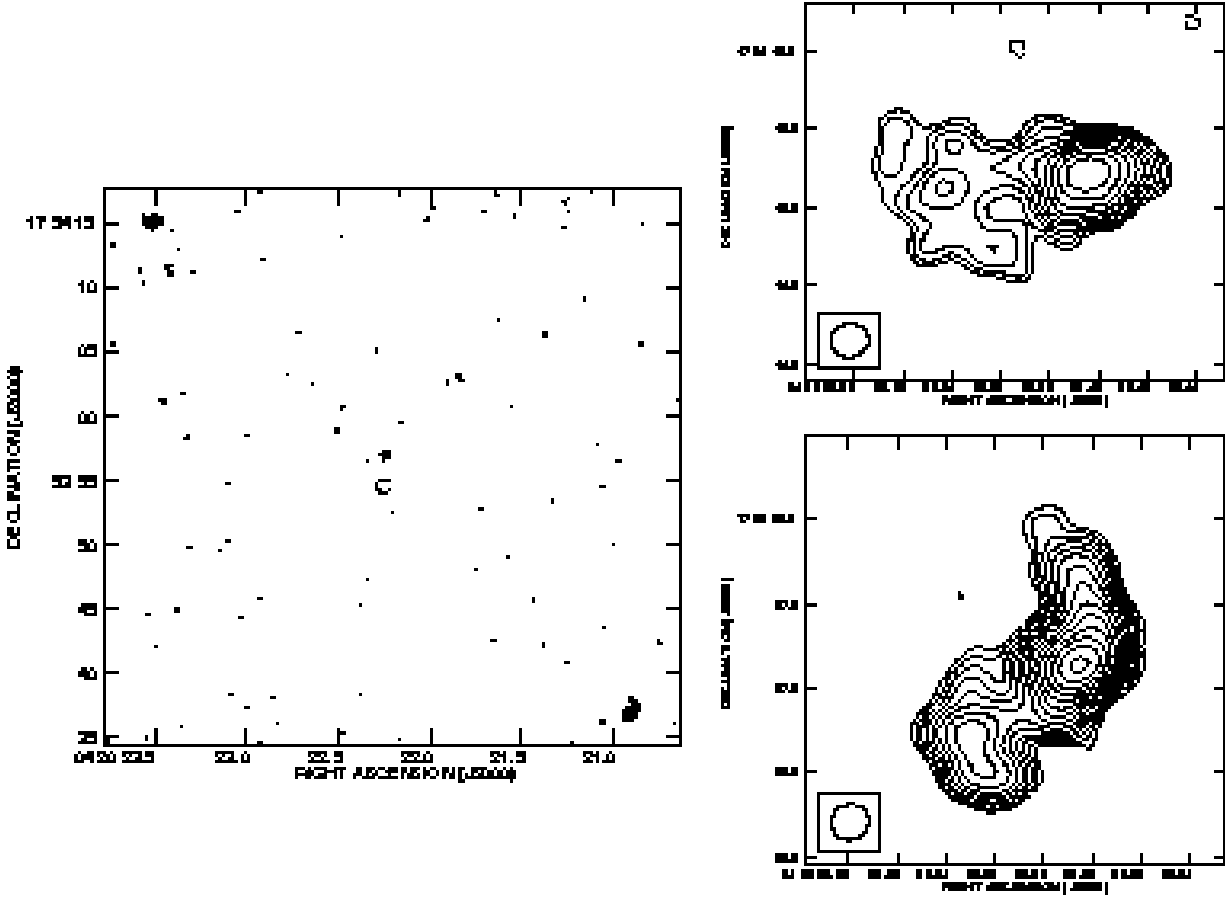


Fig. 31.— Total intensity image of 3C114 at 8.4 GHz. The peak surface brightness and contour levels increasing in steps of $2\sqrt{2}$ for the closeup views of the hotspot regions) are 7.3 mJy/beam, $(-1.4, 1.4, \dots, 90)\%$ of peak brightness. The lowest contour level in the hotspot blowup is 1% of the peak brightness.

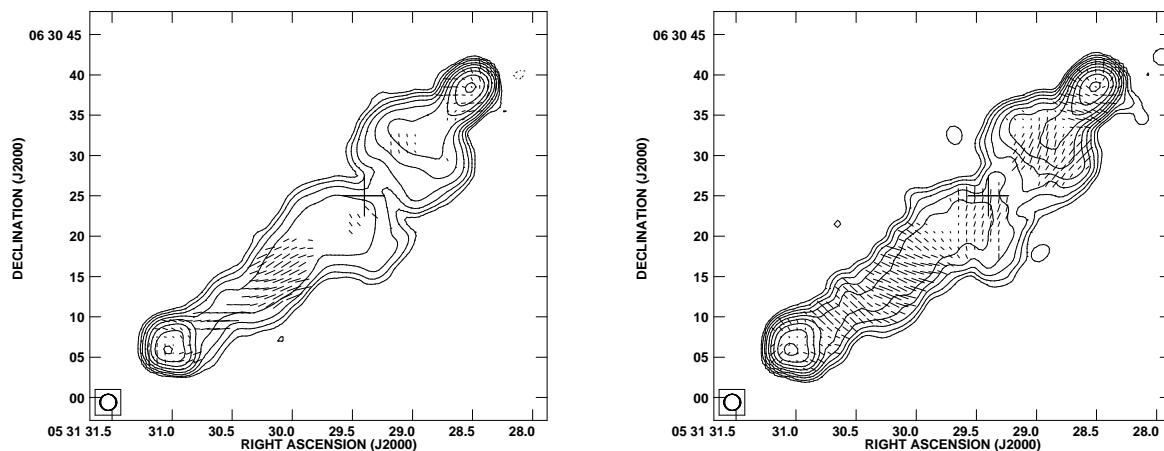


Fig. 32.— Total intensity image of 3C142.1 at (left) 1.34 GHz and (right) 4.86 GHz, at a resolution of $2''$ with fractional polarization vectors superimposed. The peak surface brightness and contour levels increasing in steps of 2 are (left) 378.8 mJy/beam, $(-0.35, 0.35, \dots, 90)\%$ of peak brightness, $1''$ vector = 20% polarization, (right) 123.0 mJy/beam, $(-0.17, 0.17, \dots, 90)\%$ of peak brightness, $1''$ vector = 25% polarization.

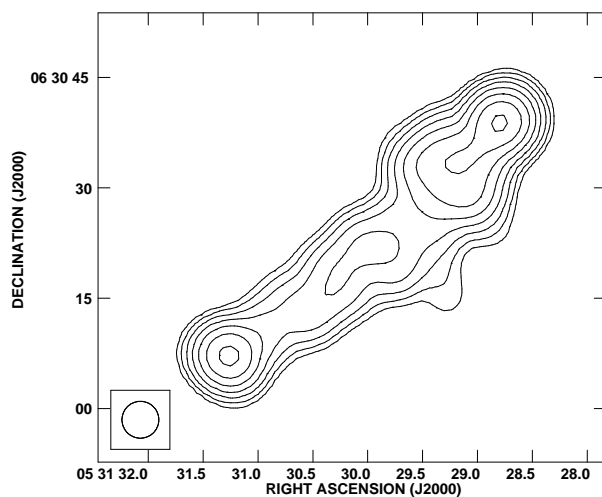


Fig. 33.— Total intensity image of 3C142.1 at 327.6 MHz. The peak surface brightness and contour levels increasing in steps of 2 are 2.6 Jy/beam, $(-0.7, 0.7, \dots, 90)\%$ of peak brightness

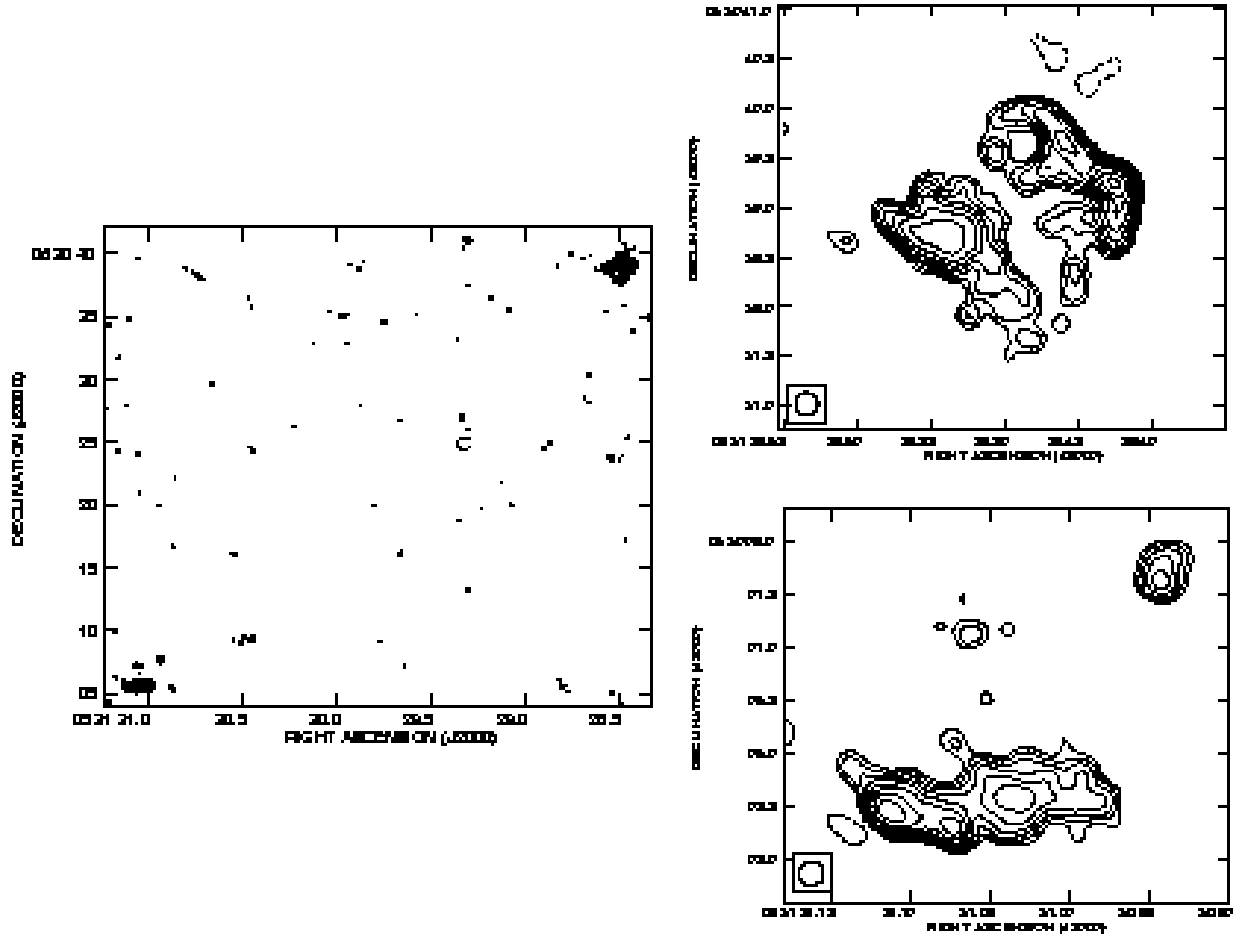


Fig. 34.— Total intensity image of 3C142.1 at 8.4 GHz. The peak surface brightness and contour levels increasing in steps of $2\sqrt{2}$ for the closeup views of the hotspot regions) are 2.1 mJy/beam, $(-5.6, 5.6, \dots, 90)\%$ of peak brightness.

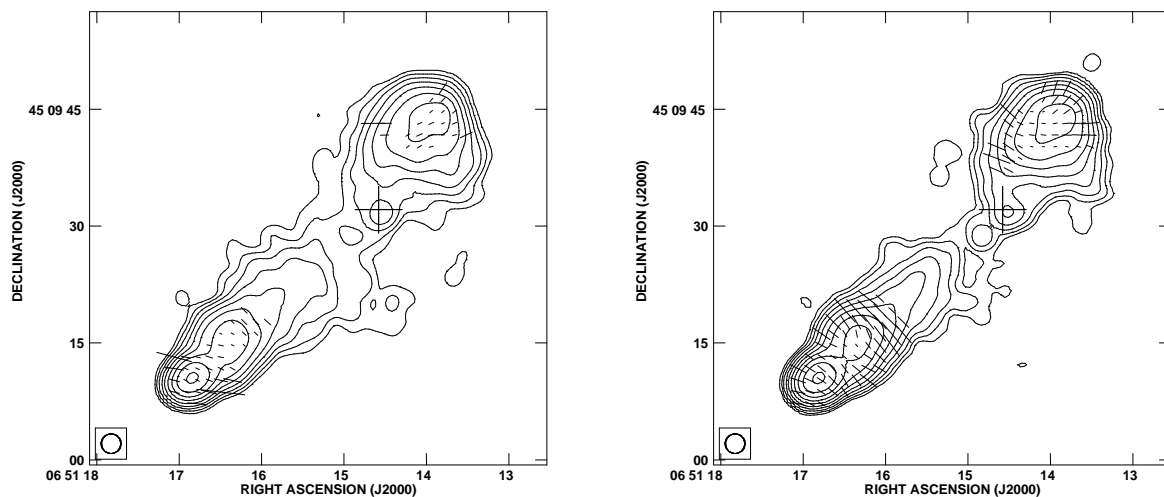


Fig. 35.— Total intensity image of 3C169.1 at (left) 1.66 GHz and (right) 4.86 GHz, at a resolution of $2.5''$ with fractional polarization vectors superimposed. The peak surface brightness and contour levels increasing in steps of 2 are (left) 153.2 mJy/beam, $(-0.35, 0.35, \dots, 90)\%$ of peak brightness, $1''$ vector = 10% polarization, (right) 56.7 mJy/beam, $(-0.17, 0.17, \dots, 90)\%$ of peak brightness, $1''$ vector = 10% polarization.

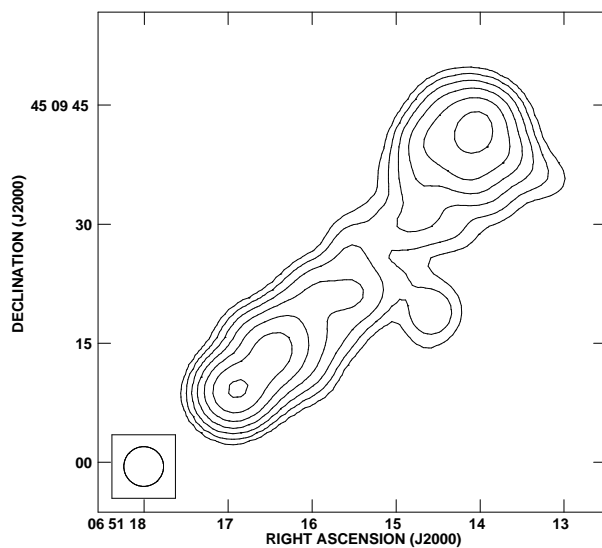


Fig. 36.— Total intensity image of 3C169.1 at 327.6 MHz. The peak surface brightness and contour levels increasing in steps of 2 are 744.1 Jy/beam, $(-1.4, 1.4, \dots, 90)\%$ of peak brightness.

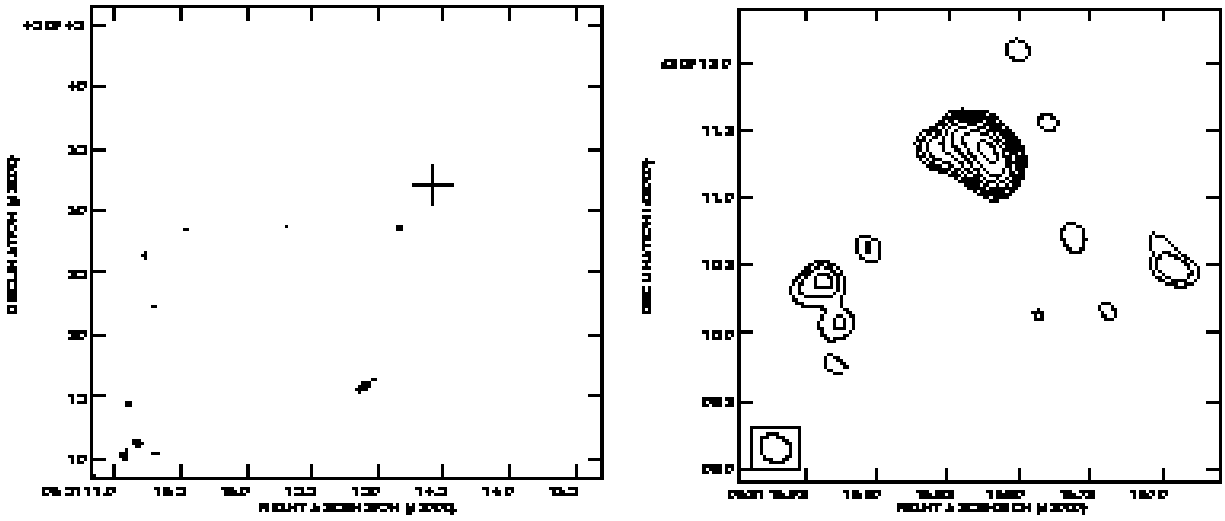


Fig. 37.— Total intensity image of 3C169.1 at 8.4 GHz. The peak surface brightness and contour levels increasing in steps of $2\sqrt{2}$ for the closeup views of the hotspot regions) are 1.5 mJy/beam, ($-16,16,32,64$)% of peak brightness. The lowest contour level in the hotspot blowup is 11.2% of the peak brightness.

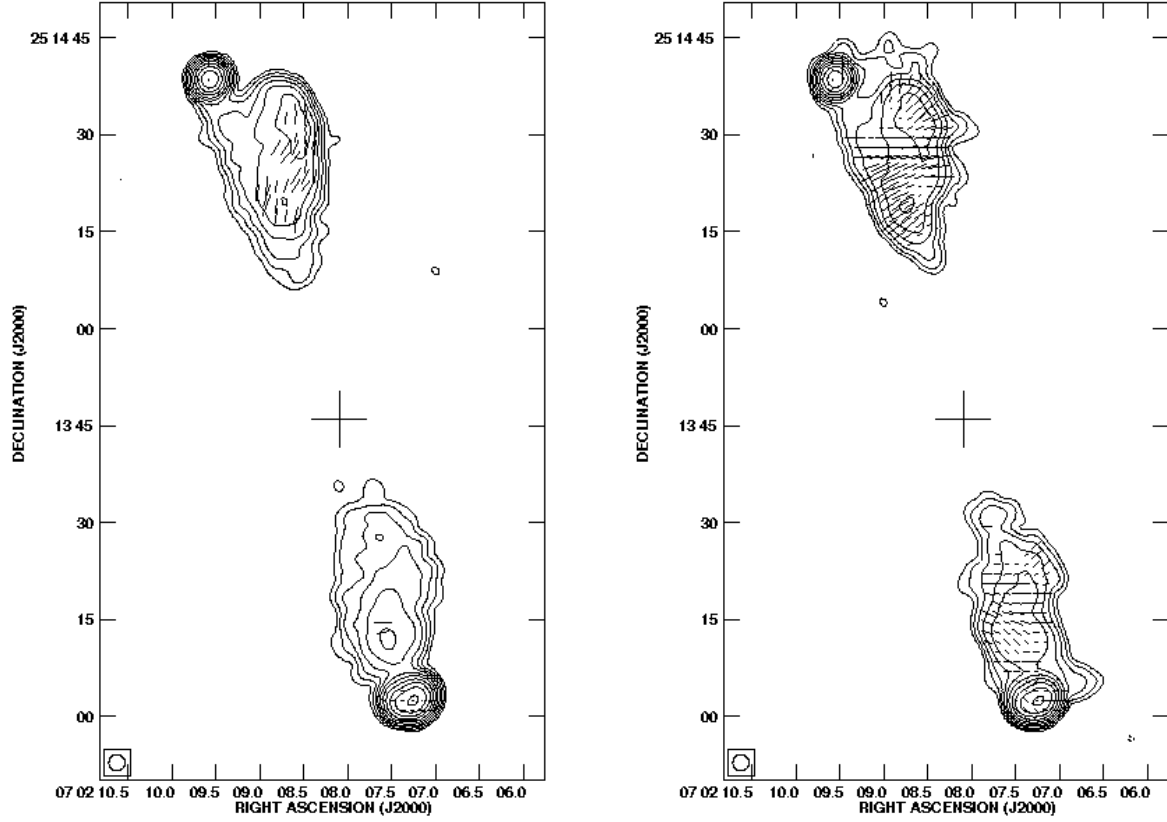


Fig. 38.— Total intensity image of 3C172 at (left) 1.66 GHz and (right) 4.86 GHz, at a resolution of $2.5''$ with fractional polarization vectors superimposed. The peak surface brightness and contour levels increasing in steps of 2 are (left) 478.1 mJy/beam, $(-0.17, 0.17, \dots, 90)\%$ of peak brightness, $1''$ vector = 10% polarization, (right) 153.7 mJy/beam, $(-0.17, 0.17, \dots, 90)\%$ of peak brightness, $1''$ vector = 11% polarization.

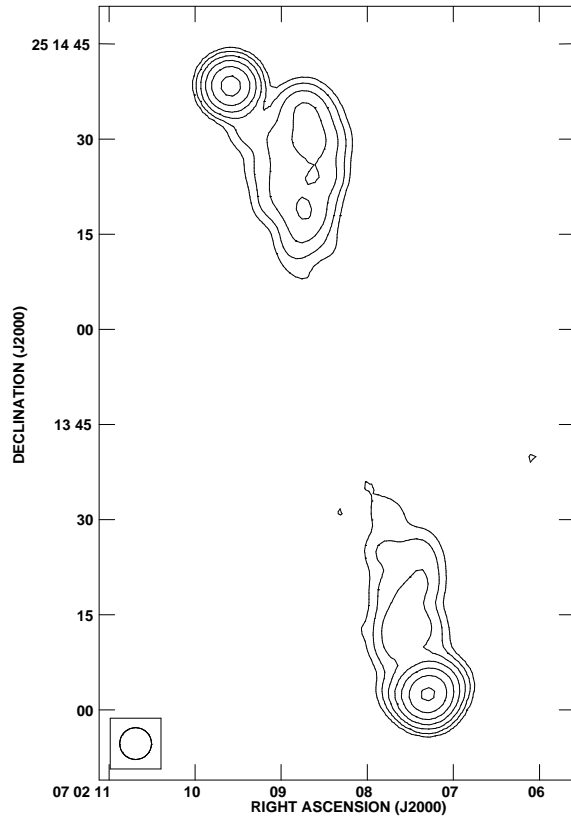


Fig. 39.— Total intensity image of 3C172 at 327.6 MHz. The peak surface brightness and contour levels increasing in steps of 2 are 2.3 Jy/beam, $(-1.4, 1.4, \dots, 90)\%$ of peak brightness.

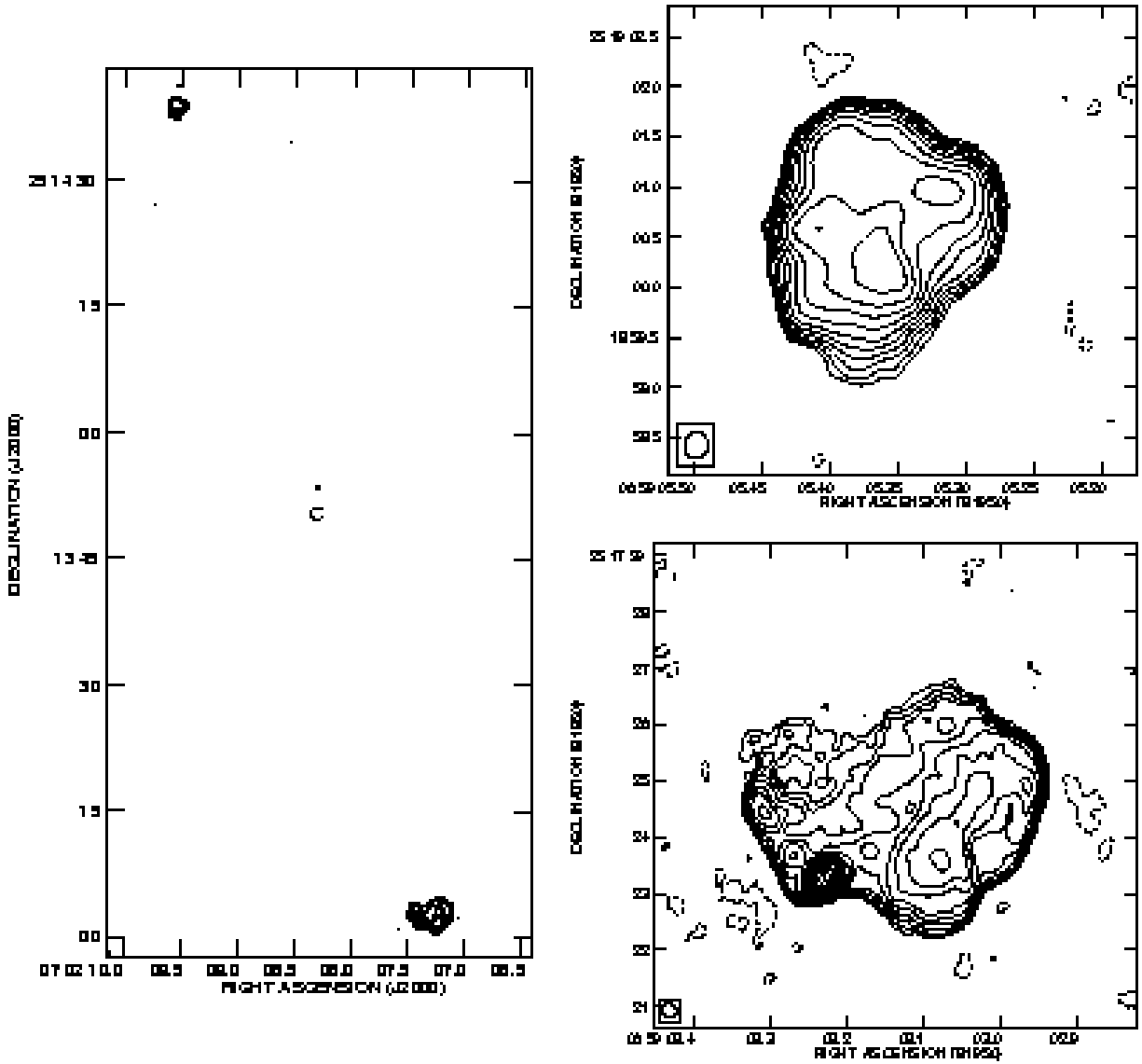


Fig. 40.— Total intensity image of 3C172 at 8.4 GHz. The peak surface brightness and contour levels increasing in steps of $2\sqrt{2}$ for the closeup views of the hotspot regions) are 11.9 mJy/beam, $(-1.4, 1.4, \dots, 90)\%$ of peak brightness. The lowest contour level in the hotspot blowup is 1% of the peak brightness.

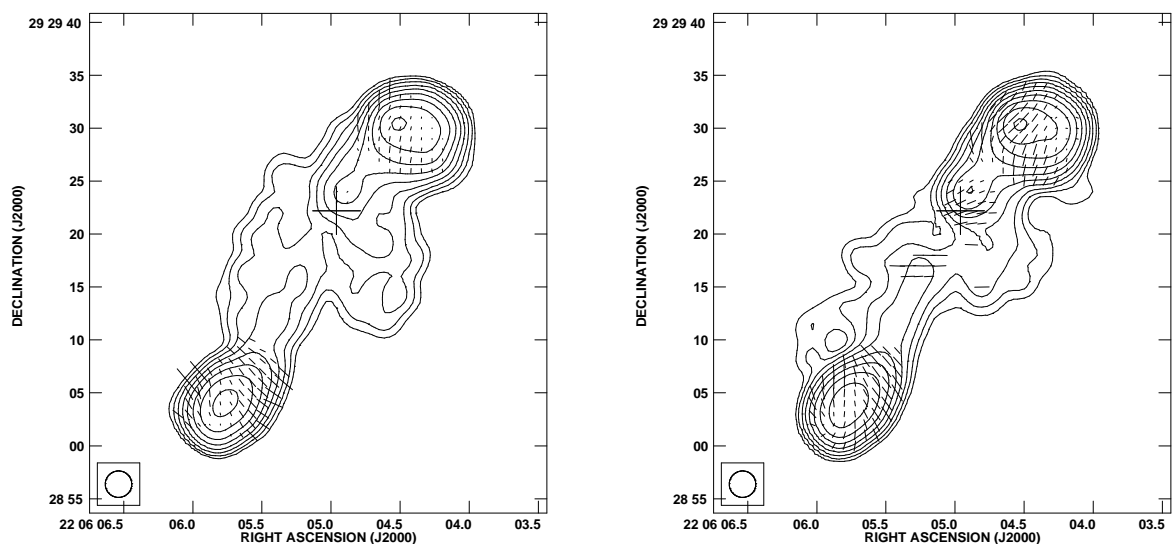


Fig. 41.— Total intensity image of 3C441 at (left) 1.34 GHz and (right) 4.86 GHz, at a resolution of $2.5''$ with fractional polarization vectors superimposed. The peak surface brightness and contour levels increasing in steps of 2 are (left) 420.1 mJy/beam, $(-0.35, 0.35, \dots, 90)\%$ of peak brightness, $1''$ vector = 20% polarization, (right) 184.8 mJy/beam, $(-0.17, 0.17, \dots, 90)\%$ of peak brightness, $1''$ vector = 20% polarization.

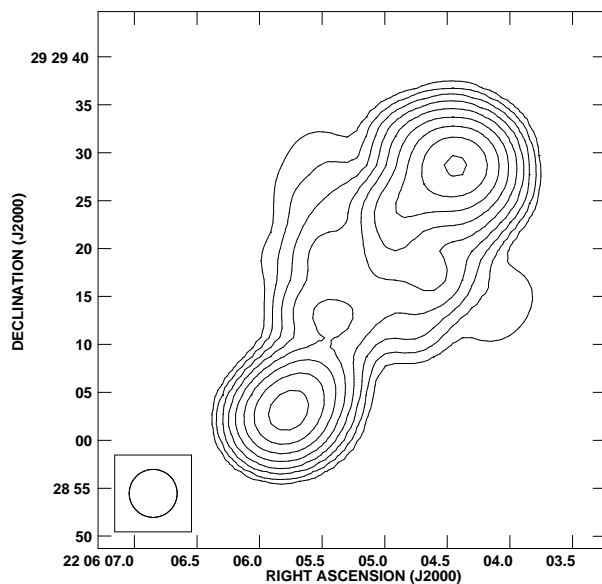


Fig. 42.— Total intensity image of 3C441 at 327.6 MHz. The peak surface brightness and contour levels increasing in steps of 2 are 2.8 Jy/beam, $(-0.35, 0.35, \dots, 90)\%$ of peak brightness.

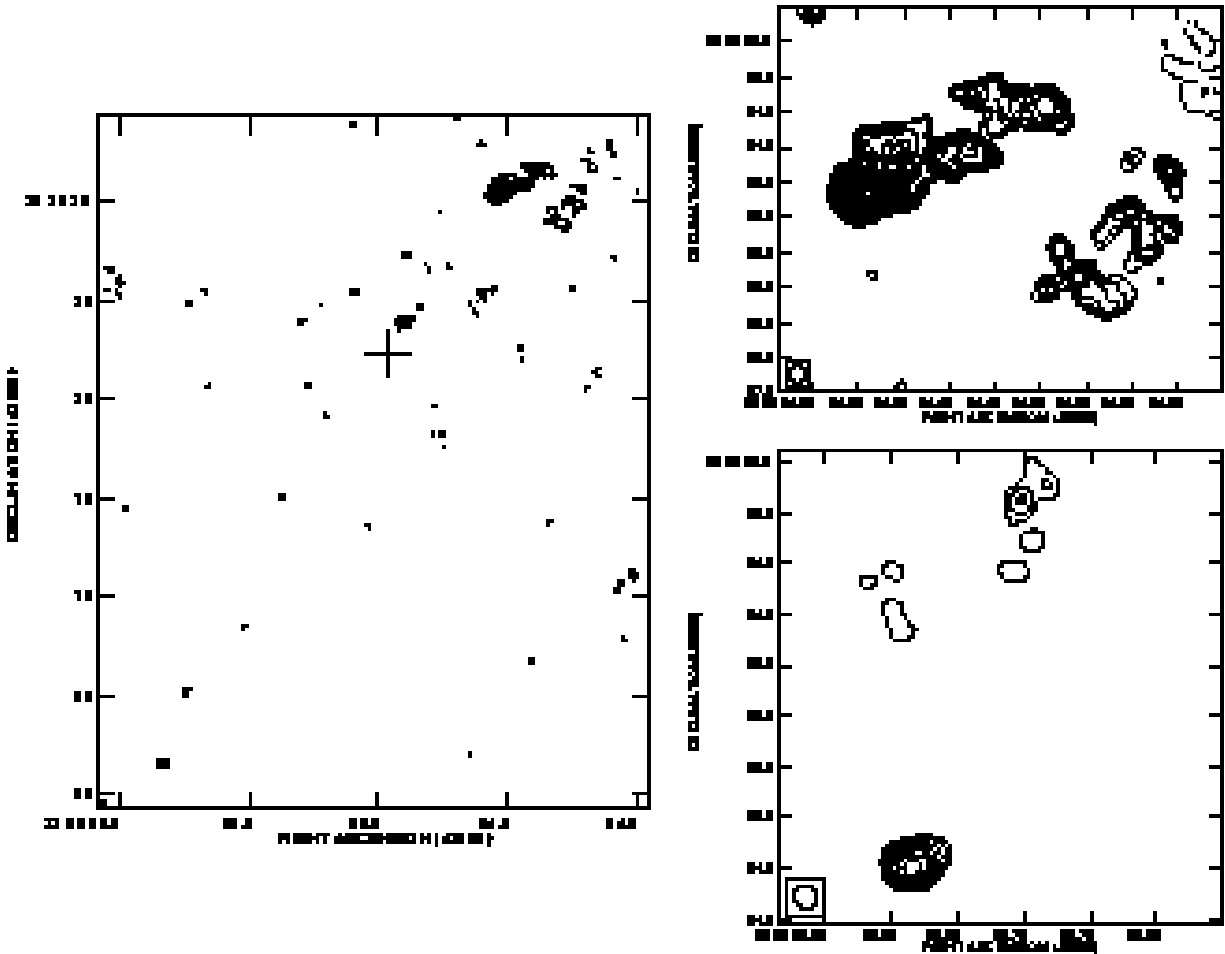


Fig. 43.— Total intensity image of 3C441 at 8.4 GHz. The peak surface brightness and contour levels increasing in steps of $2\sqrt{2}$ for the closeup views of the hotspot regions) are 33.9 mJy/beam, $(-0.7, 0.7, \dots, 90)\%$ of peak brightness. The lowest contour level in the hotspot blowup is 0.5% of the peak brightness.

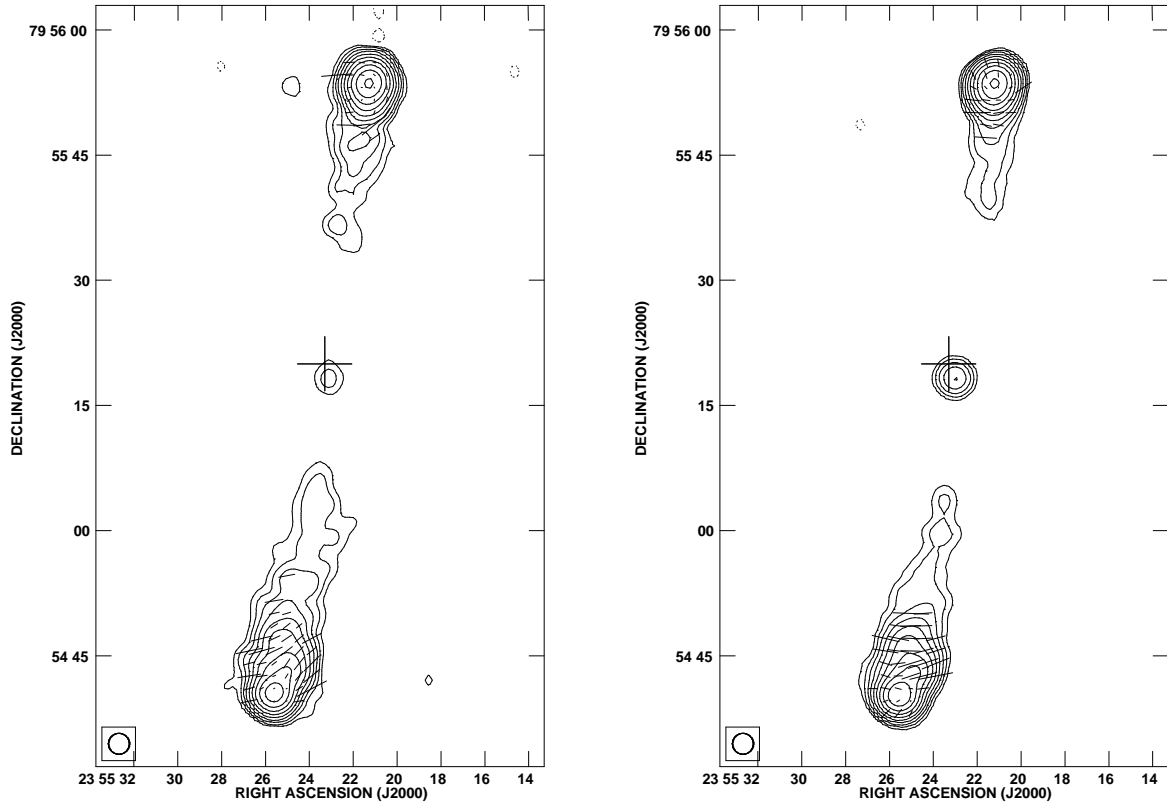


Fig. 44.— Total intensity image of 3C469.1 at (left) 1.34 GHz and (right) 4.86 GHz, at a resolution of $2.5''$ with fractional polarization vectors superimposed. The peak surface brightness and contour levels increasing in steps of 2 are (left) 559.2 mJy/beam, $(-0.17, 0.17, \dots, 90)\%$ of peak brightness, $1''$ vector = 12.5% polarization, (right) 131.7 mJy/beam, $(-0.17, 0.17, \dots, 90)\%$ of peak brightness, $1''$ vector = 7% polarization.

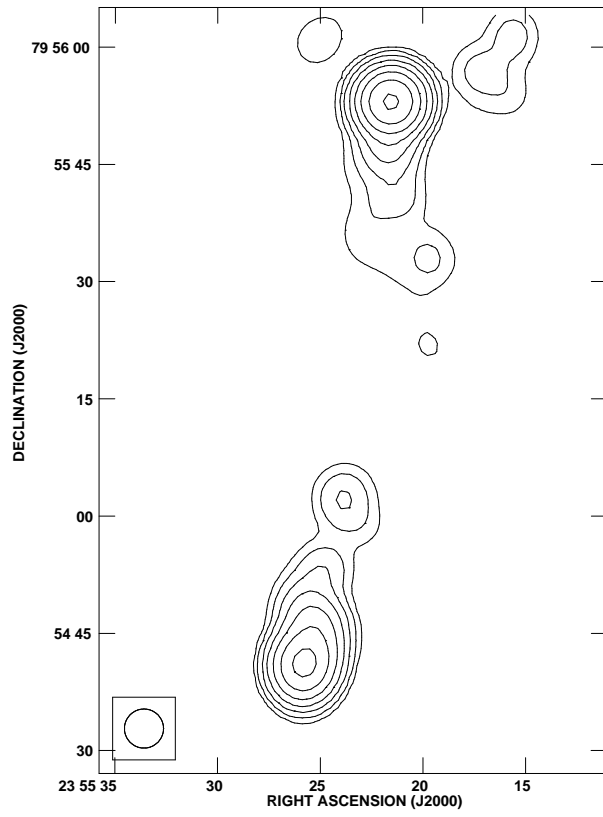


Fig. 45.— Total intensity image of 3C469.1 at 327.6 MHz. The peak surface brightness and contour levels increasing in steps of 2 are 2.9 Jy/beam, $(-0.7, 0.7, \dots, 90)\%$ of peak brightness.

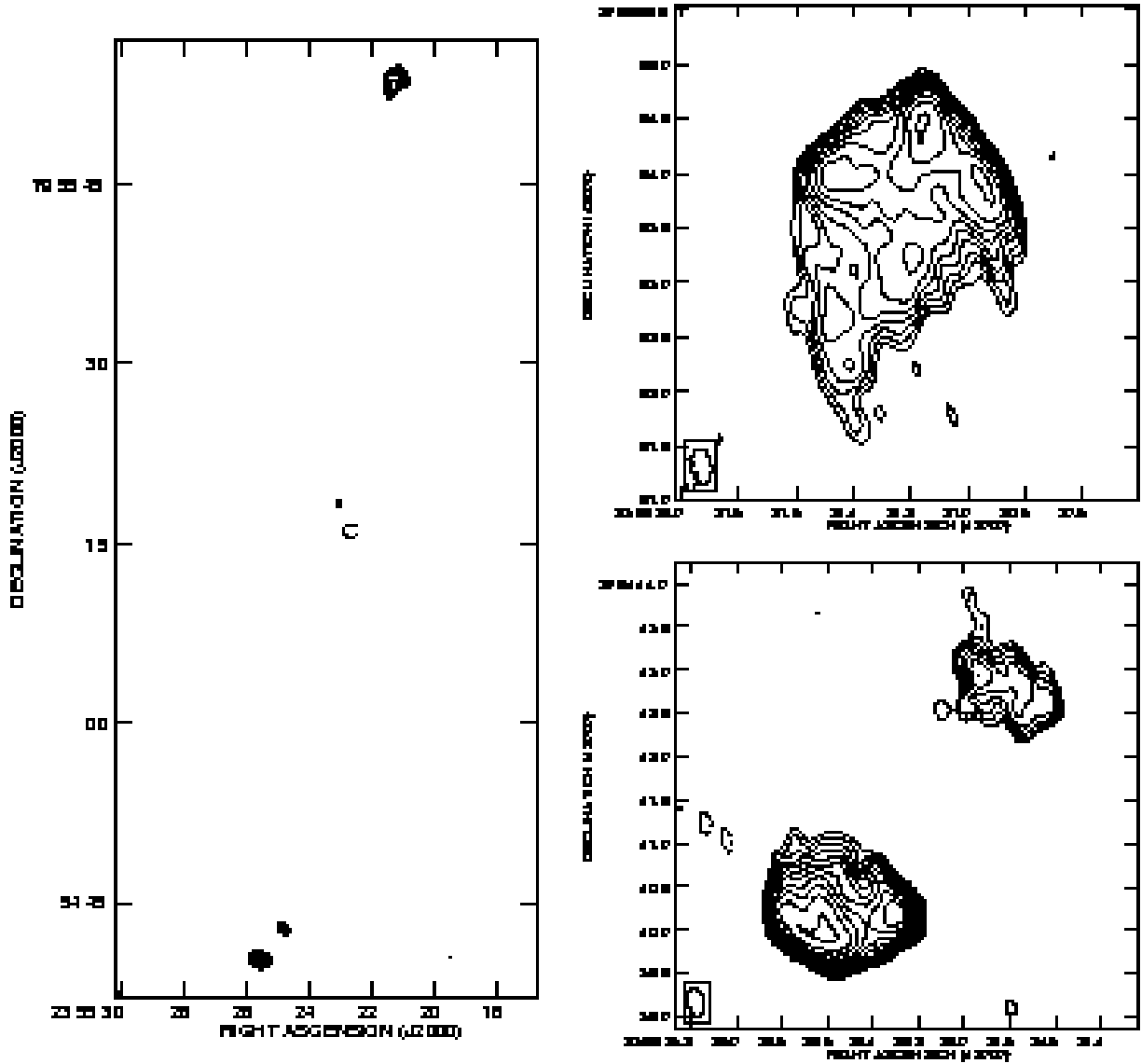


Fig. 46.— Total intensity image of 3C469.1 at 8.4 GHz. The peak surface brightness and contour levels increasing in steps of $2(\sqrt{2})$ for the closeup views of the hotspot regions) are 4.0 mJy/beam, $(-5.6, 5.6, \dots, 90)\%$ of peak brightness. The lowest contour level in the hotspot blowup is 2.8% of the peak brightness.

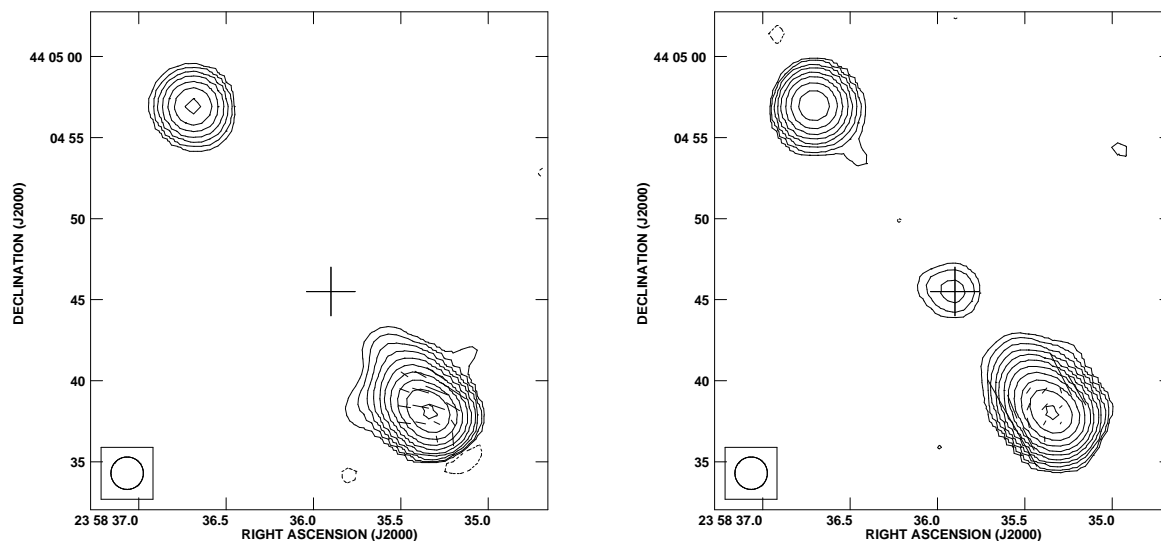


Fig. 47.— Total intensity image of 3C470 at (left) 1.34 GHz and (right) 4.86 GHz, at a resolution of $2''$ with fractional polarization vectors superimposed. The peak surface brightness and contour levels increasing in steps of 2 are (left) 1.2 Jy/beam, $(-0.17, 0.17, \dots, 90)\%$ of peak brightness, $1''$ vector = 7.7% polarization, (right) 318.8 mJy/beam, $(-0.085, 0.085, \dots, 90)\%$ of peak brightness, $1''$ vector = 14% polarization.

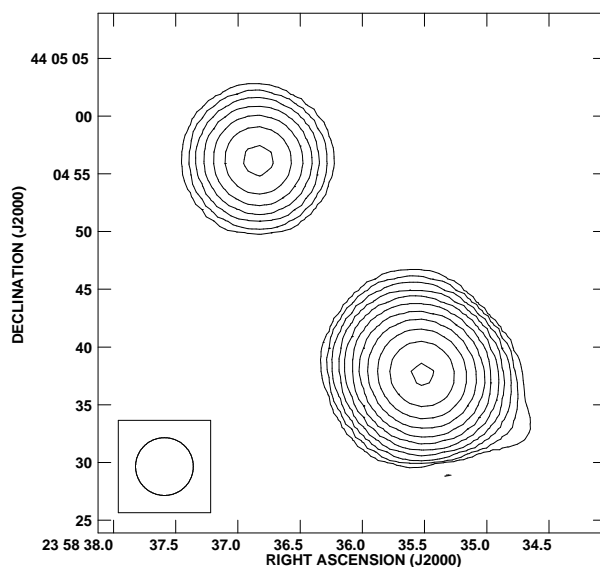


Fig. 48.— Total intensity image of 3C470 at 327.6 MHz. The peak surface brightness and contour levels increasing in steps of 2 are 5.9 Jy/beam, $(-0.085, 0.085, \dots, 90)\%$ of peak brightness.

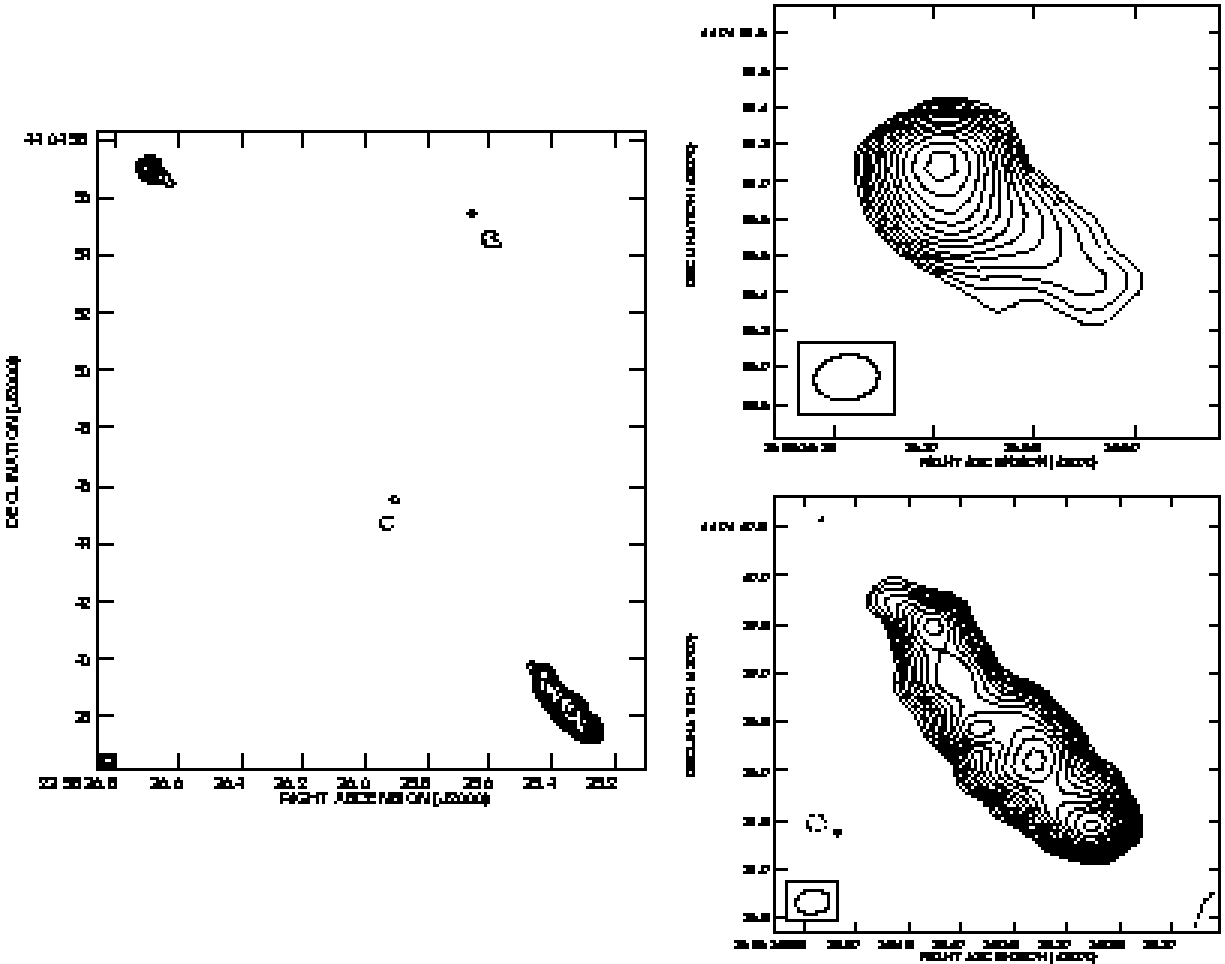


Fig. 49.— Total intensity image of 3C470 at 8.4 GHz. The peak surface brightness and contour levels increasing in steps of $2\sqrt{2}$ for the closeup views of the hotspot regions) are 39.9 mJy/beam, $(-1.4, 1.4, \dots, 90)\%$ of peak brightness. The lowest contour level in the hotspot blowup is 0.7% of the peak brightness.

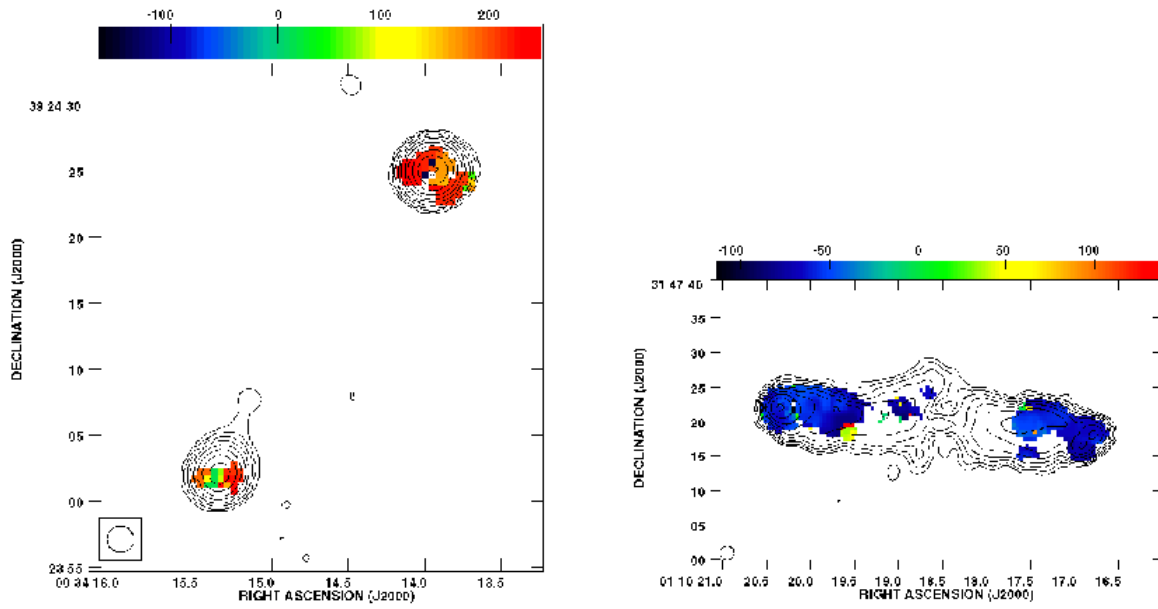


Fig. 50.— Rotation measure image in colour superimposed by 5 GHz radio contours for (left) 3C13 and (right) 3C34. The RM was obtained from polarization maps at 1.4 and 5 GHz. The colour-scale units are in rad m^2 .

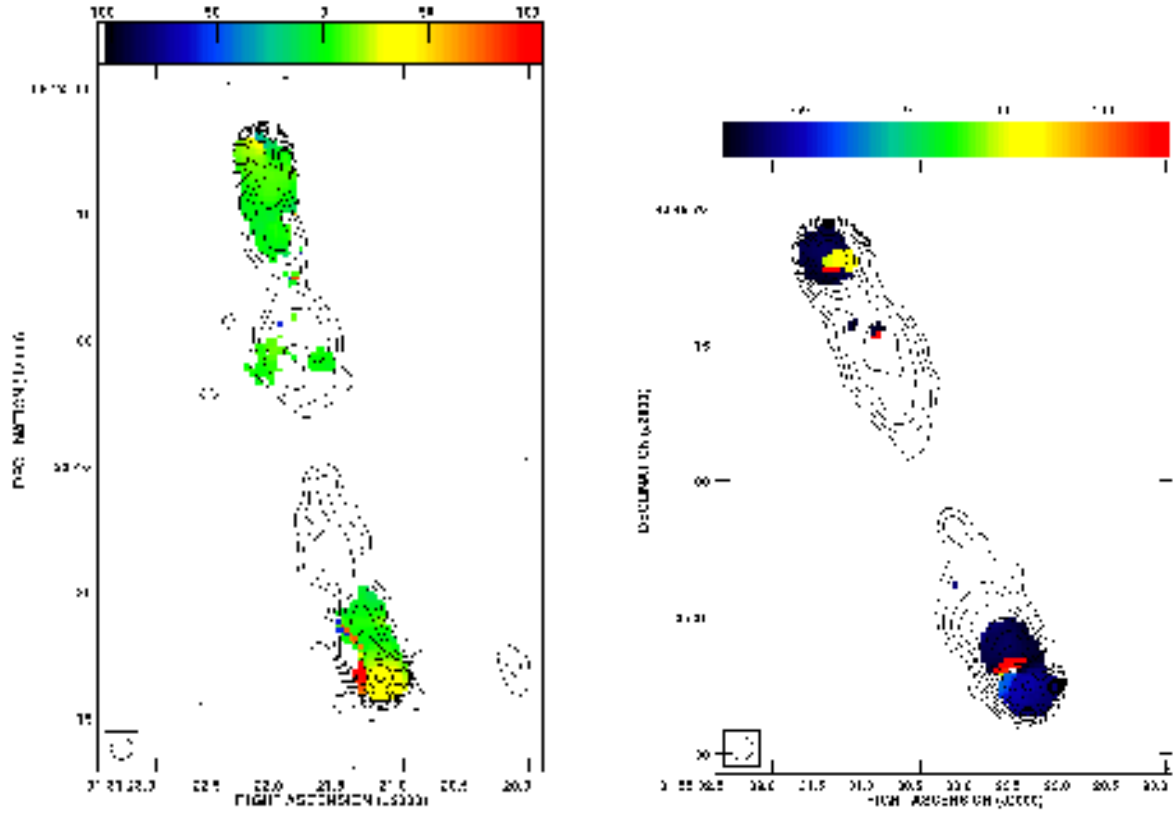


Fig. 51.— Rotation measure image in colour superimposed by 5 GHz radio contours for (left) 3C44 and (right) 3C54. The RM was obtained from polarization maps at 1.4 and 5 GHz. The colour-scale units are in rad m^2 .

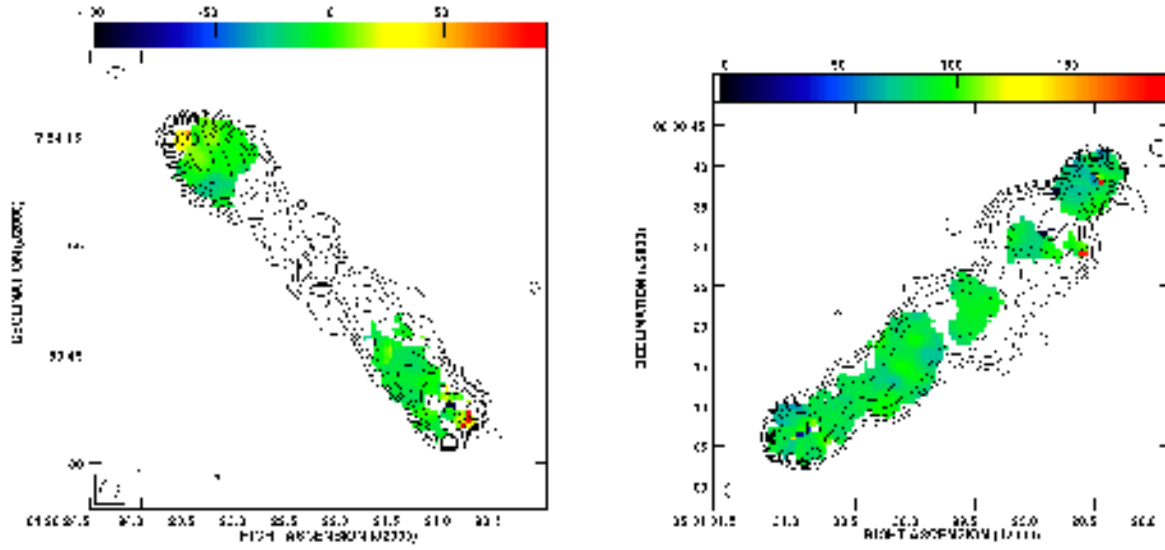


Fig. 52.— Rotation measure image in colour superimposed by 5 GHz radio contours for (left) 3C114 and (right) 3C142.1. The RM was obtained from polarization maps at 1.4 and 5 GHz. The colour-scale units are in rad m^2 .

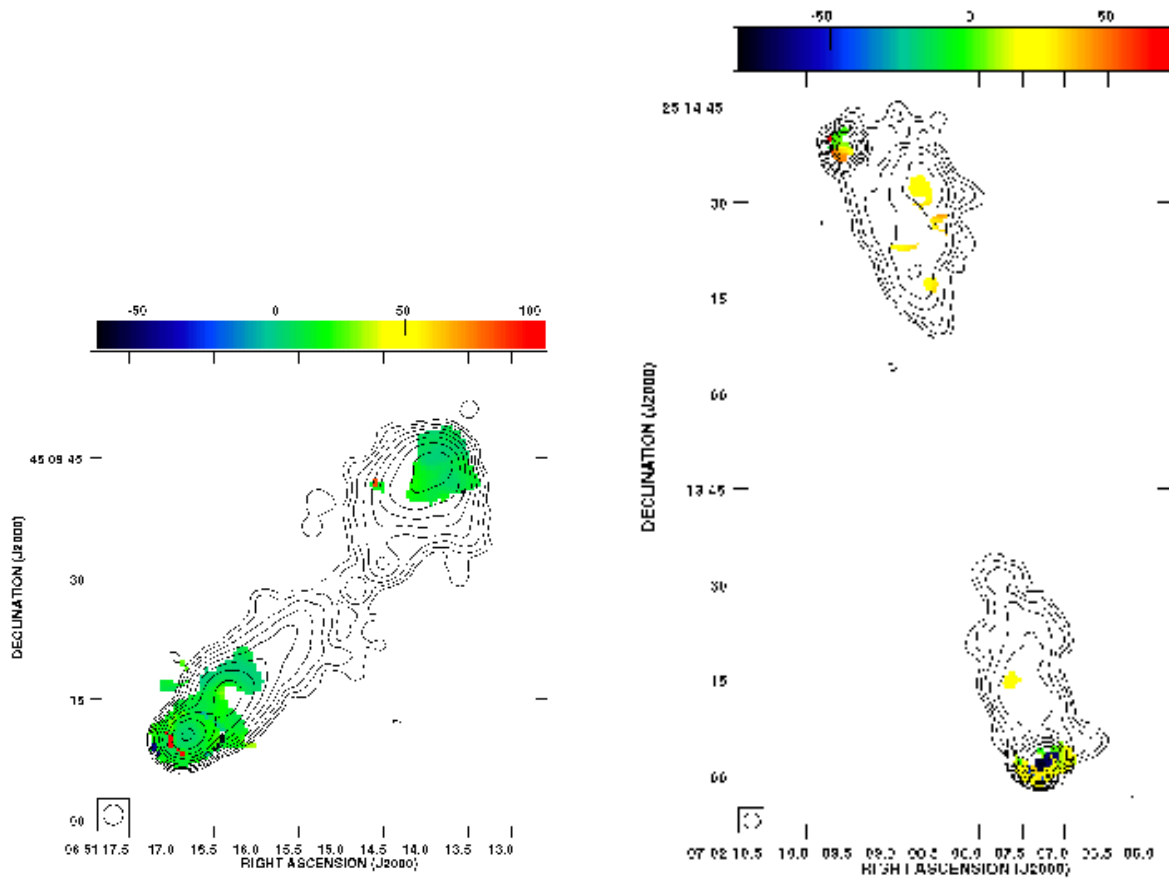


Fig. 53.— Rotation measure image in colour superimposed by 5 GHz radio contours for (left) 3C169.1 and (right) 3C172. The RM was obtained from polarization maps at 1.4 and 5 GHz. The colour-scale units are in rad m^2 .

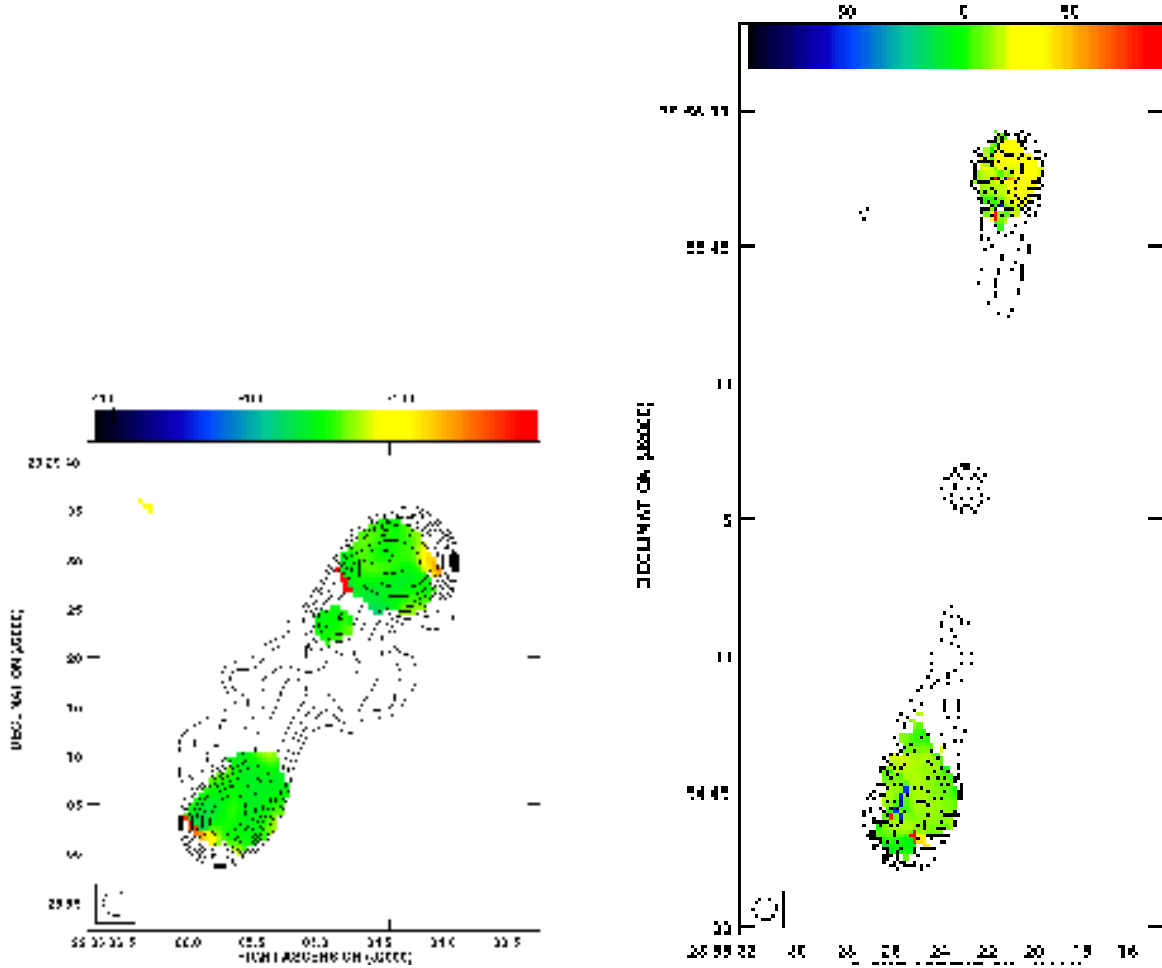


Fig. 54.— Rotation measure image in colour superimposed by 5 GHz radio contours for (left) 3C441 and (right) 3C469.1. The RM was obtained from polarization maps at 1.4 and 5 GHz. The colour-scale units are in rad m^2 .

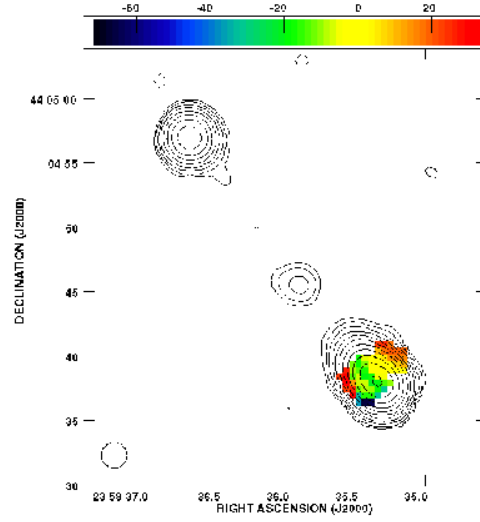


Fig. 55.— Rotation measure image in colour superimposed by 5 GHz radio contours for 3C470. The RM was obtained from polarization maps at 1.4 and 5 GHz. The colour-scale units are in rad m^2 .

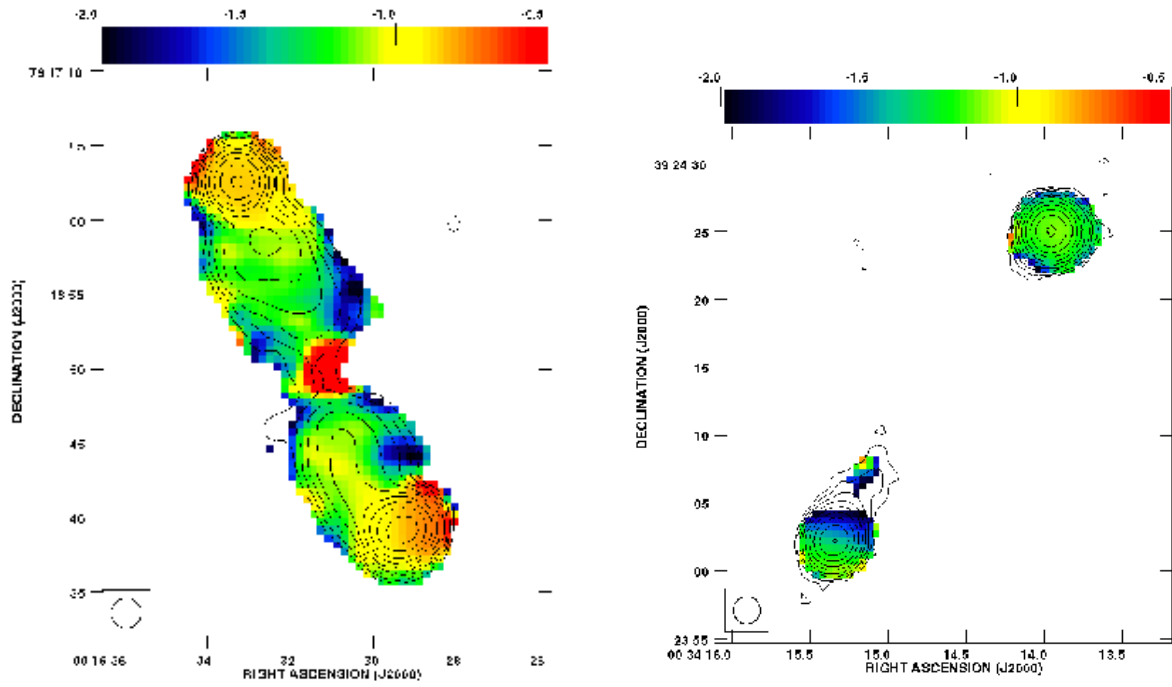


Fig. 56.— Spectral index image in colour superimposed by 1.4 GHz radio contours at a resolution of $\sim 2''$ for (left) 3C6.1 and (right) 3C13. The spectral index image was obtained with 1.4 and 5 GHz data.

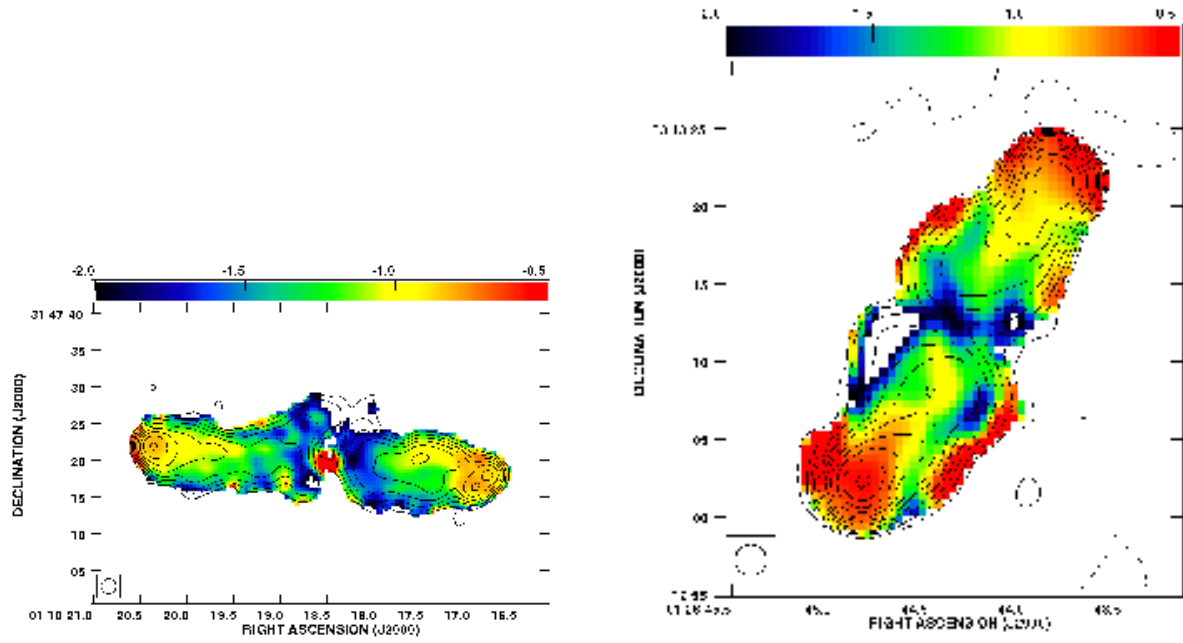


Fig. 57.— Spectral index image in colour superimposed by 1.4 GHz radio contours at a resolution of $\sim 2''$ for (left) 3C34 and (right) 3C41. The spectral index image was obtained with 1.4 and 5 GHz data.

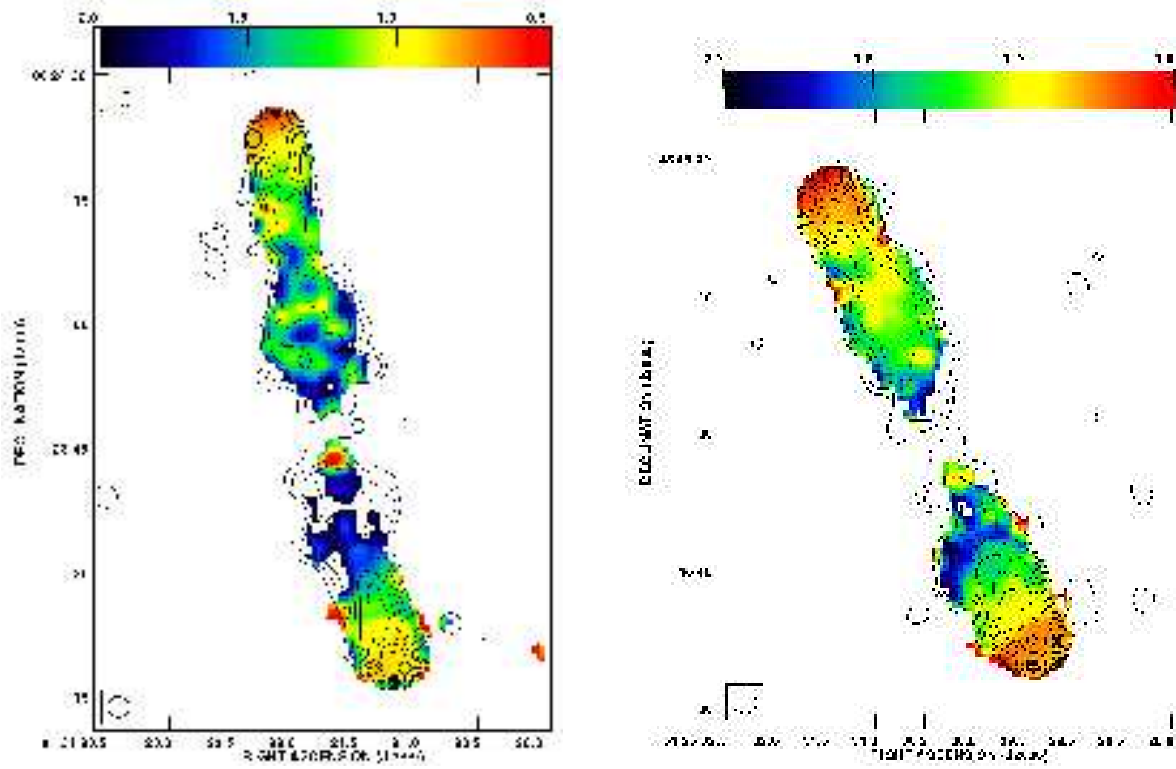


Fig. 58.— Spectral index image in colour superimposed by 1.4 GHz radio contours at a resolution of $\sim 2''$ for (left) 3C44 and (right) 3C54. The spectral index image was obtained with 1.4 and 5 GHz data.

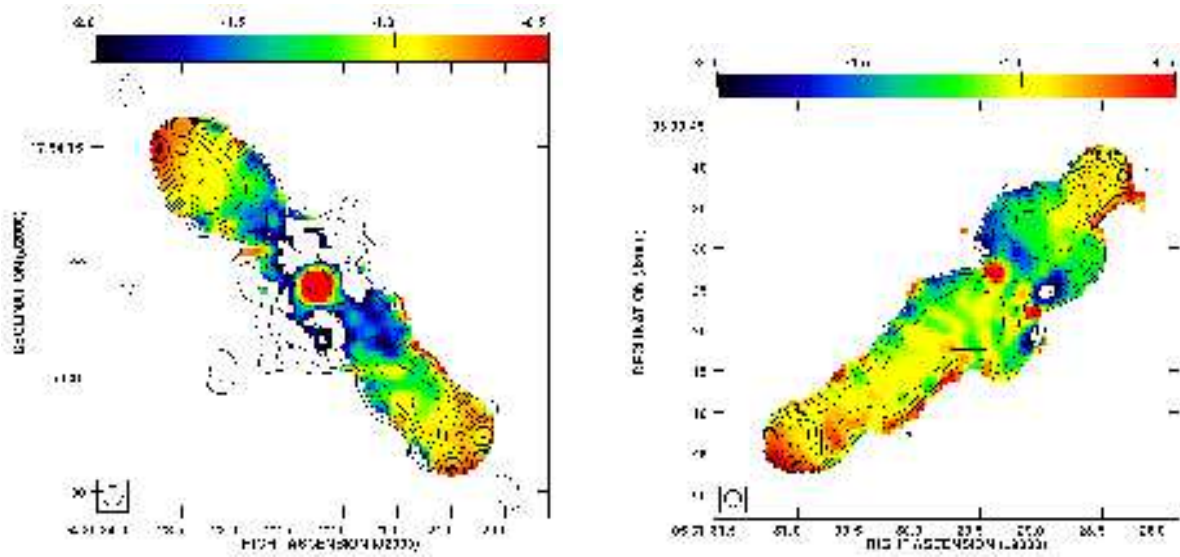


Fig. 59.— Spectral index image in colour superimposed by 1.4 GHz radio contours at a resolution of $\sim 2''$ for (left) 3C114 and (right) 3C142.1. The spectral index image was obtained with 1.4 and 5 GHz data.

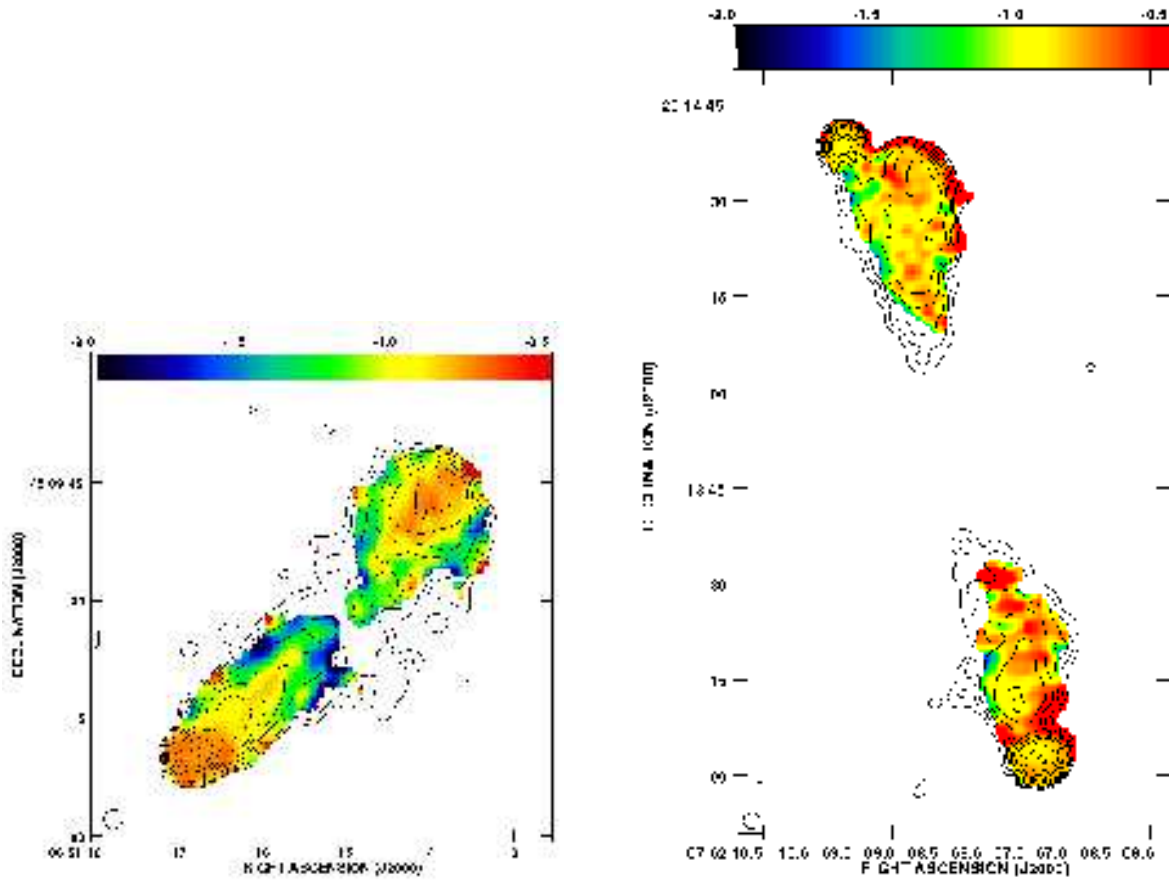


Fig. 60.— Spectral index image in colour superimposed by 1.4 GHz radio contours at a resolution of $\sim 2''$ for (left) 3C169.1 and (right) 3C172. The spectral index image was obtained with 1.4 and 5 GHz data.

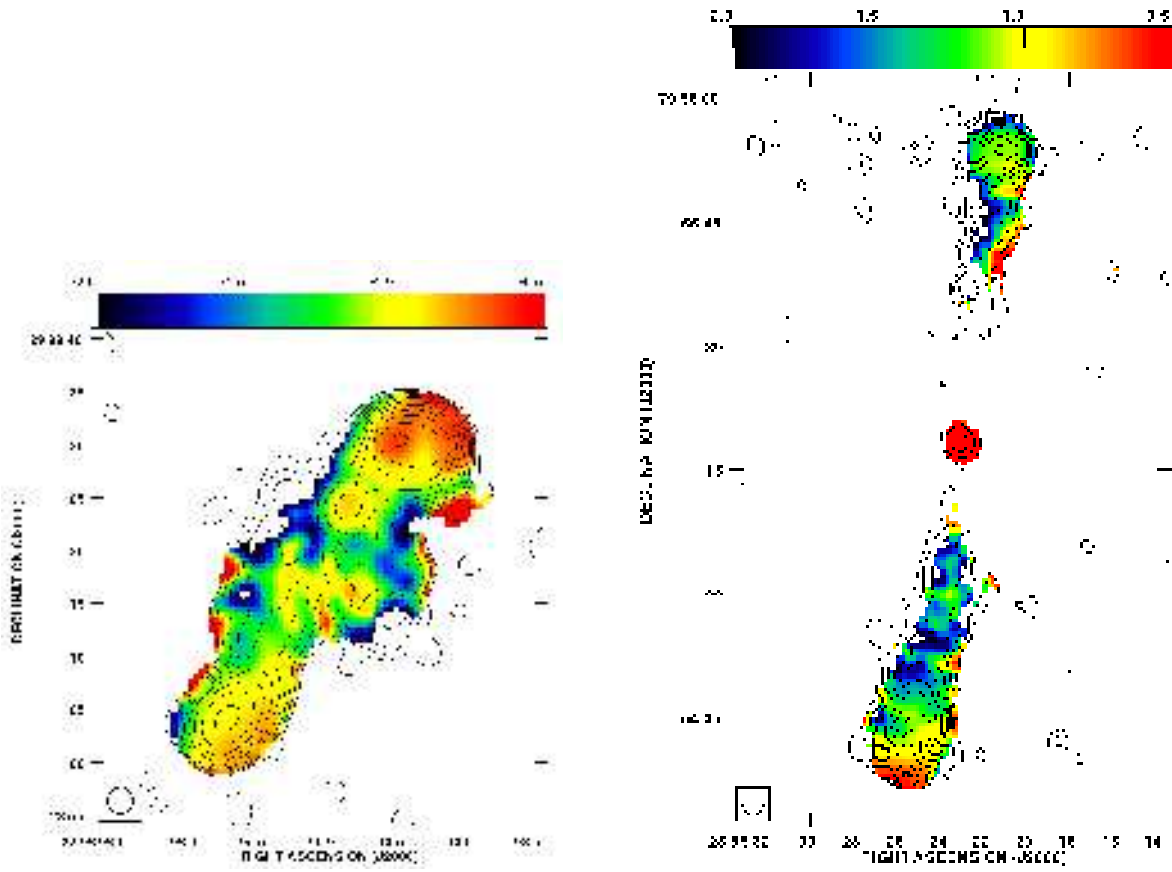


Fig. 61.— Spectral index image in colour superimposed by 1.4 GHz radio contours at a resolution of $\sim 2''$ for (left) 3C441 and (right) 3C469.1. The spectral index image was obtained with 1.4 and 5 GHz data.

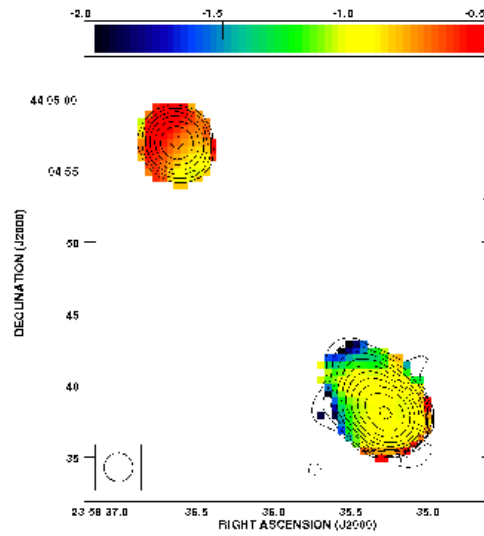


Fig. 62.— Spectral index image in colour superimposed by 1.4 GHz radio contours at a resolution of $\sim 2''$ for 3C470. The spectral index image was obtained with 1.4 and 5 GHz data.

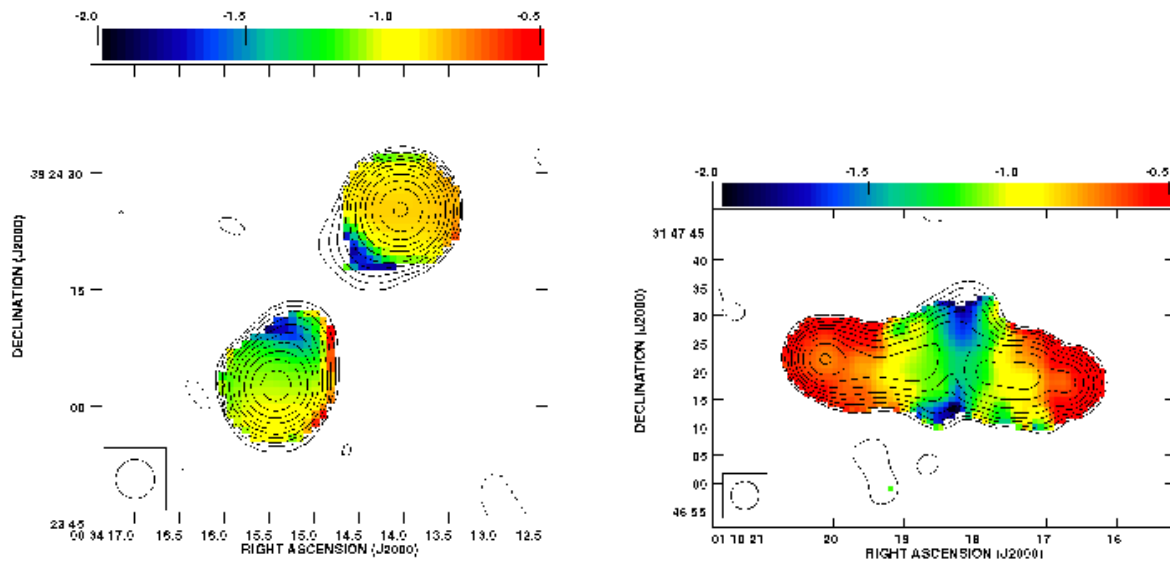


Fig. 63.— Spectral index image in colour superimposed by 1.4 GHz radio contours at a resolution of $5''$ for (left) 3C13 and (right) 3C34. The spectral index image was obtained with 327.6 MHz and 1.4 GHz data.

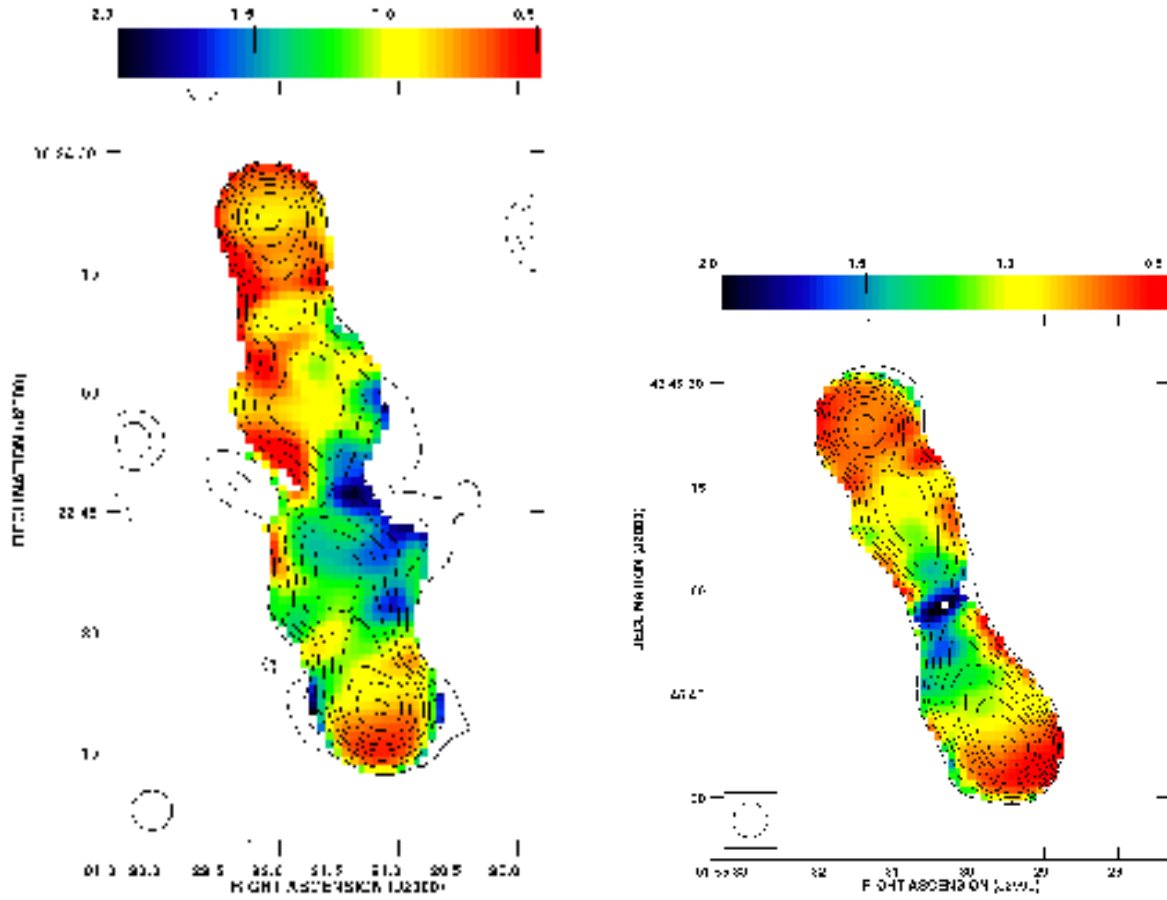


Fig. 64.— Spectral index image in colour superimposed by 1.4 GHz radio contours at a resolution of $5''$ for (left) 3C44 and (right) 3C54. The spectral index image was obtained with 327.6 MHz and 1.4 GHz data.

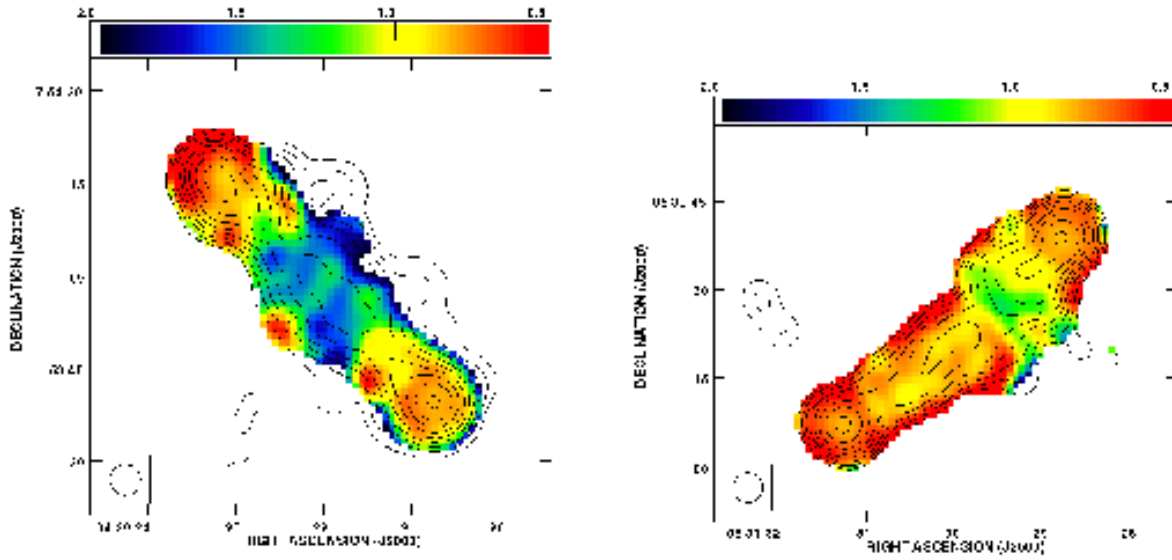


Fig. 65.— Spectral index image in colour superimposed by 1.4 GHz radio contours at a resolution of $5''$ for (left) 3C114 and (right) 3C142.1. The spectral index image was obtained with 327.6 MHz and 1.4 GHz data.

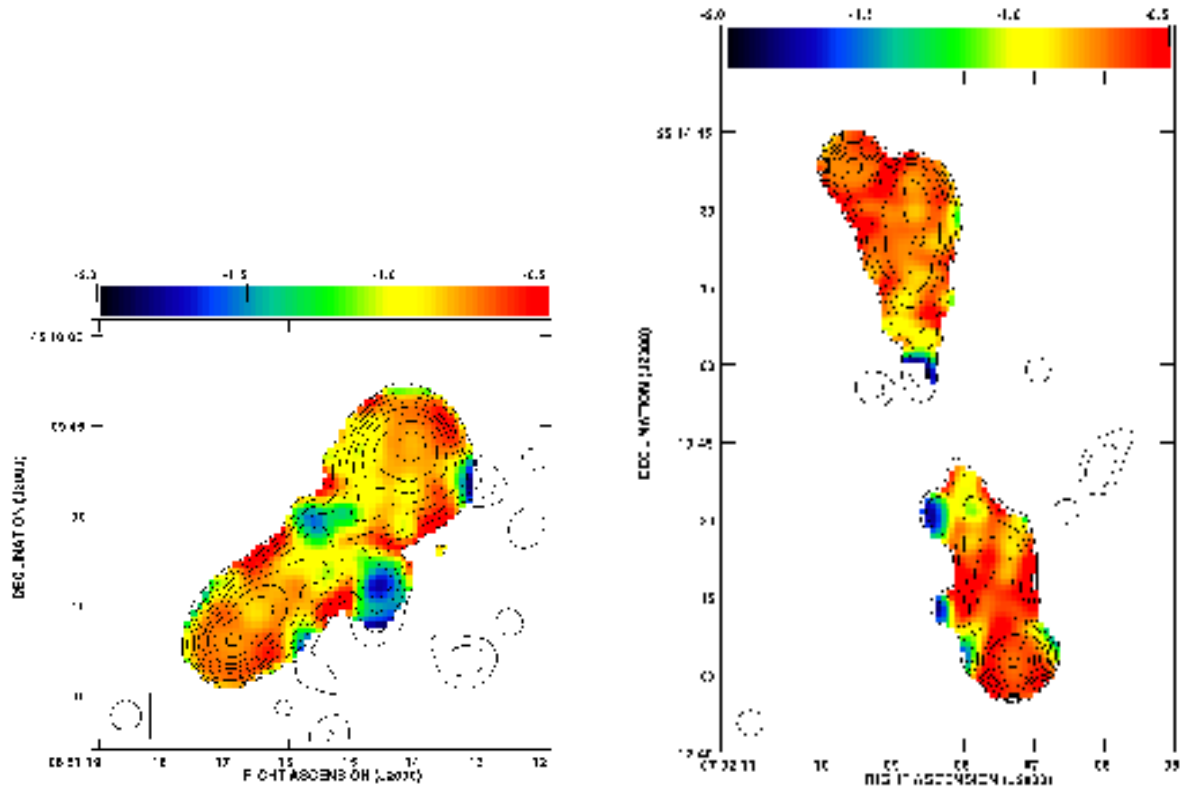


Fig. 66.— Spectral index image in colour superimposed by 1.4 GHz radio contours at a resolution of $5''$ for (left) 3C169.1 and (right) 3C172. The spectral index image was obtained with 327.6 MHz and 1.4 GHz data.

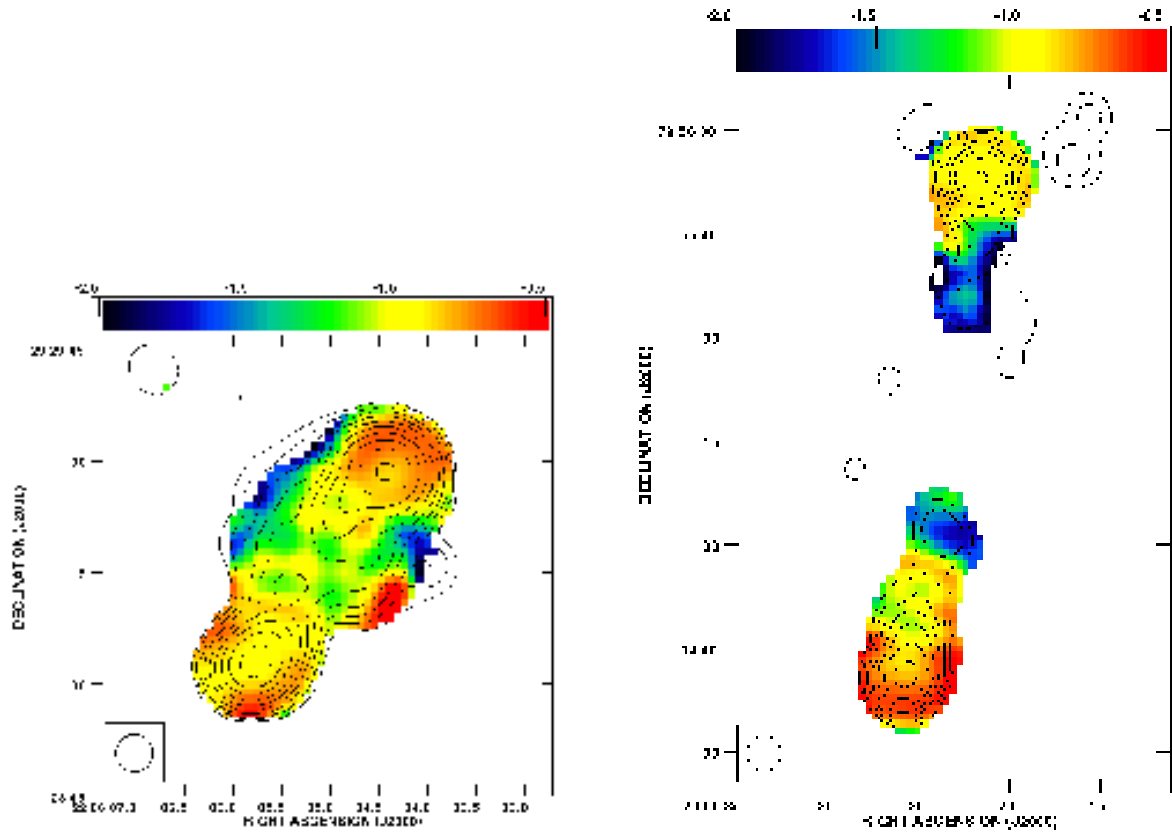


Fig. 67.— Spectral index image in colour superimposed by 1.4 GHz radio contours at a resolution of $5''$ for (left) 3C441 and (right) 3C469.1. The spectral index image was obtained with 327.6 MHz and 1.4 GHz data.

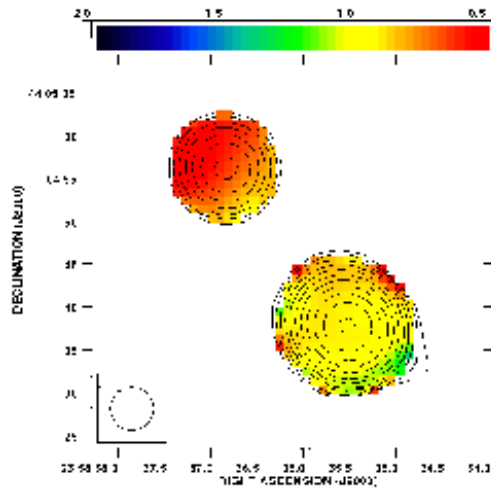


Fig. 68.— Spectral index image in colour superimposed by 1.4 GHz radio contours at a resolution of $5''$ for 3C470. The spectral index image was obtained with 327.6 MHz and 1.4 GHz data.

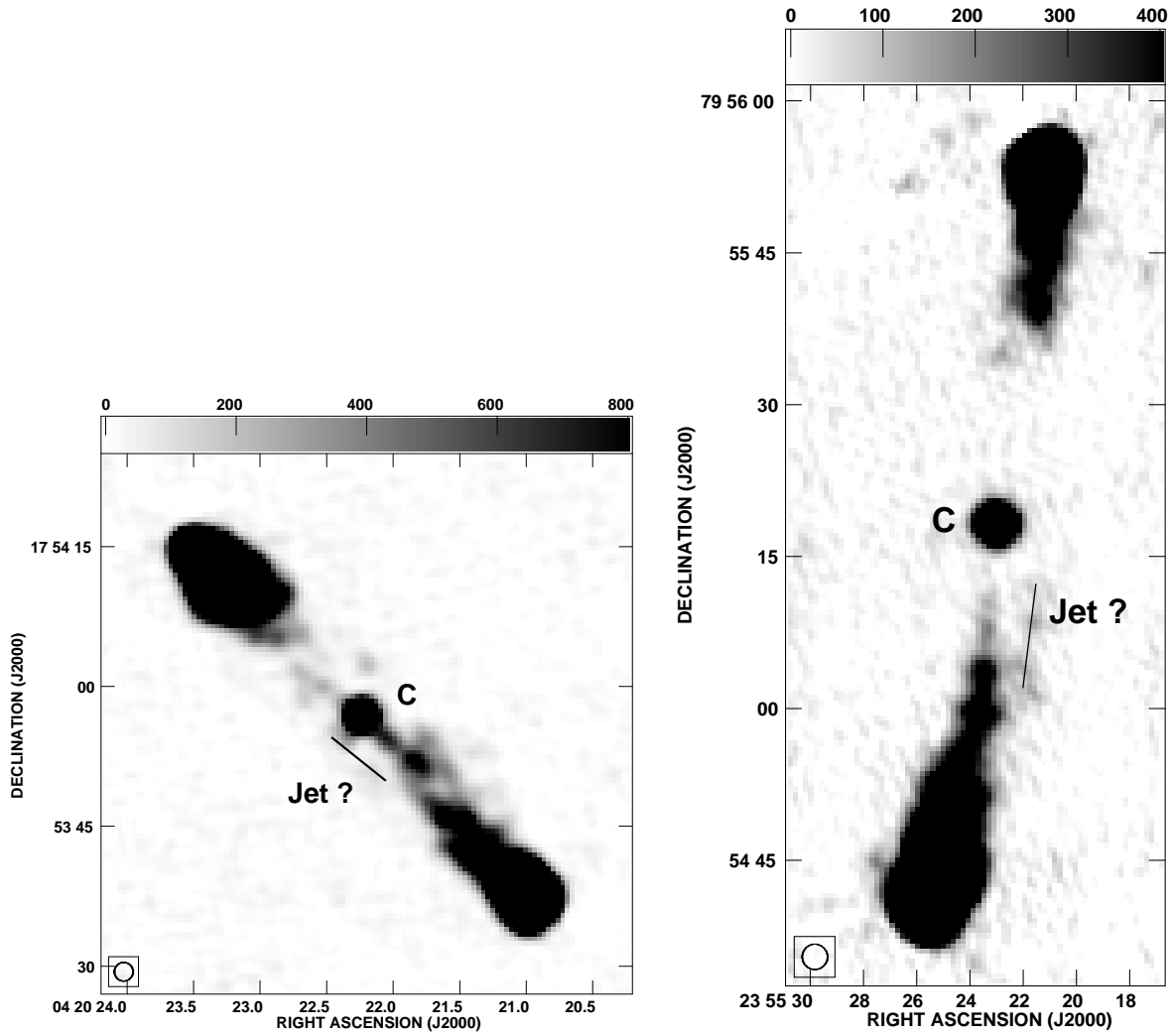


Fig. 69.— The 5 GHz grey-scale image of (left) 3C114 and (right) 3C469.1, showing the jet-like feature.

We would like to express our thanks to the referee for a careful assessment of our work, which has significantly improved this paper. We thank Joel C. Carvalho for stimulating discussions on this work. This work was supported in part by the U. S. National Science Foundation under grant AST-0507465 (R. A. D.). The National Radio Astronomy Observatory is a facility of the National Science Foundation operated under cooperative agreement by Associated Universities, Inc. This research has made use of the NASA/IPAC Extragalactic Database (NED) which is operated by the Jet Propulsion Laboratory, California Institute of Technology, under contract with the National Aeronautics and Space Administration.

Facility: VLA (A, B, C and D-array configurations)

A. Notes on Individual Sources

3C6.1: The Hubble Space Telescope (*HST*) observations with WFPC2/F702W by McCarthy et al. (1997) show the optical galaxy to be compact with the lower isophotes extending at $PA \sim 30^\circ$, roughly aligned with the radio axis (Pooley & Henbest 1974). The overall radio morphology could be classified as type LW1. The spectral index $\alpha_{5.0}^{1.4}$ shows a general steepening away from the hotspot and towards the core.

3C13: The *HST* observations of this source show the optical galaxy to be extended over nearly $4''$ with two tail-like structures to the south and east of the nucleus (McCarthy et al. 1997). The extended emission in both the nucleus and on the $1''$ scale is aligned with the radio axis at a PA of 145° . Best et al. (1997, 1998) find that the infrared emission from the host galaxy is also strongly aligned with the radio axis. Our radio image shows clear hotspots but no radio core in this high-redshift source (Fig. 15). More sensitive observations are required to be able to image the full radio bridge.

3C34: This source lies in a compact cluster of galaxies (McCarthy et al. 1995). The *HST* observations of McCarthy et al. (1997) find that the central galaxy is diffuse with a low surface brightness. Best et al. (1997) have proposed that the aligned optical emission observed in the *HST* images of 3C34 is associated with a region of massive star formation, induced by the passage of the radio jet through a galaxy within the surrounding cluster. In Fig. 18 we see that 3C34 shows twin hotspots on the eastern side. The polarization image shows extensive structure and changes in the orientation of the magnetic field. The 5 GHz greyscale image shows a faint jet on both sides of the core with the jet on the western side being brighter closer to the core.

3C41: The *HST* observations of McCarthy et al. (1997); Best et al. (1997) show that the optical galaxy is compact and symmetrical. The K-band image of the galaxy indicates

that it is misaligned by about 25° with the radio axis (Best et al. 1997, 1998). We observe extended radio bridge region in this source, but the radio core is observed only in the 8 GHz image (see Fig. 21). The high resolution image at 8 GHz also shows a complex hotspot region. The radio morphology shows a LW3-type distortion, although the southern lobe seems to turn back towards the core close to it. The spectral index map shows a flatter spectral index extending through the centre of the northern lobe, perhaps suggesting the presence of the radio jet (Fig 57).

3C44: This galaxy lies in a cluster (Spinrad 1986; McCarthy et al. 1995). The *HST* observations show that the galaxy is either composed of two components oriented north-south or, more likely, is bisected by a dust lane running east-west (McCarthy et al. 1997). Figure 23 shows that this source exhibits a LW1-type radio morphology. We detect a weak radio core at the position, RA=01h,31m,21.6459s, Dec= $06^\circ, 23', 43.1048''$. There is a bright radio source on the eastern side about $50''$ from the core in 3C44. The spectral index shows a general steepening away from the hotspots (Fig. 58). 3C44 shows a hint of a jet-like structure extending towards the southern hotspot in the 5 GHz image (Fig. 69).

3C54: The *HST* observations reveal a compact nucleus in this galaxy with an extension to the southwest in PA 220° (McCarthy et al. 1997). There is a compact object near the end of the $2''$ extension from the nucleus. It is unclear if the extension is a bridge, tidal tail, or jet. There is another companion object a few arcseconds to the southeast. In Fig.26 we see that this source shows a LW1-type lobe morphology. No radio core is observed. The northern hotspot shows two components in the 5 GHz image. 3C54 shows a jet-like structure extending towards the southern hotspot in the 5 GHz image.

3C114: The low surface brightness optical galaxy of 3C114 is poorly detected in the *HST* observations (McCarthy et al. 1997). A faint compact nucleus with several clumps within the central few arcseconds is observed in this source. The radio bridge region and core are clearly detected in our observations (Fig.29). 3C114 shows a jet-like structure extending towards the southern hotspot in the 5 GHz image. However, the jet-like feature is more prominent on the northern side in the 1.4 GHz image.

3C142.1: Extended [OII] emission in an elongated east-west structure $\sim 5''$ across has been observed for 3C142.1 by Hes et al. (1996). The radio source lies close to a PA $\sim 40^\circ$, not aligned with the emission-line region. We see clear extended radio lobes in 3C142.1. (Fig. 32). The southern lobe shows a nearly constant spectral index across it (Fig. 59). This is an interesting source with a bridge structure that is different from most sources. It does not show the classic surface brightness decline from the hotspot toward the core, has a roughly constant spectral index, and a complex hotspot structure.

3C169.1: McCarthy et al. (1997) have observed two galaxies in this system, both with extended structure. The host galaxy of 3C169.1 shows a clear extension to the east with a number of faint clumps within the central arcsecond. The two components lie along the radio axis, and the companion object has an extension pointing towards the radio galaxy. In Fig. 35 we see that the northern hotspot is much fainter than the southern hotspot. The northern hotspot is not detected in the 8 GHz image.

3C172: The *HST* image of 3C712 shows that it lies in a complex system – four objects are detected in the optical image (McCarthy et al. 1997). There are two galaxies lying to the southwest that appear to be associated with 3C172, and they lie along the axis of the radio source. We find that this source has an interesting radio structure (see Fig. 38). The bridge appears to pull away to the west side of the source. The polarization image suggests that the magnetic field has been carried to the side of the radio bridge along with the relativistic plasma. However, the 8 GHz image indicates that the two brightest hotspots and the weak radio core lie roughly along a line. 3C172 shows a jet-like feature closer to the northern hotspot in the 5 GHz image.

3C441: The *HST* observations of 3C441 by McCarthy et al. (1997) and Best et al. (1997) show that the host galaxy is compact and lies in a cluster. The optical galaxy shows a slight extension to the northwest, along the radio axis. The *HST* image shows a diffuse object located 12'' north and 8'' west of the core galaxy. We find that this source has a complex radio morphology, especially in the northern radio lobe and hotspot (Fig. 41). The maps suggest that the jet has shifted position moving from the west to the present position indicated by the brightest hotspot. The bridge seems to exhibit a type LW3 lobe morphology. The 5 GHz greyscale image shows a jet-like feature extending towards the northern hotspot.

3C469.1: The *HST* observations of McCarthy et al. (1997) find that the host galaxy of 3C469.1 shows a double structure at PA 95°, not aligned with the radio axis. We detect a bright radio core in this source but not sufficient radio bridge emission (Fig. 44). The source is at a redshift of $z=1.336$ and more sensitive observations are needed to observe the full bridge region in the source 3C469.1 shows a jet-like feature extending towards the southern hotspot in the 5 GHz image.

3C470: Best et al. (1998) find that the host galaxy of 3C470 is slightly extended in both the optical and the K-band images, with the elongation being highly misaligned (by 80°) with the radio axis. We find that the radio bridge in 3C470 is partly visible only on the southern side (Fig. 44). This is the highest redshift object in our sample ($z=1.653$). Therefore more sensitive observations are required to observe the full bridge region. We detect a radio core at the position, RA=23h,58m,35.9063s, Dec=44°,04',45.5180''. 3C470 shows a slight extension in the radio core towards the southern hotspot in the 5 GHz image.

REFERENCES

- Alexander P., 1987, MNRAS, 225, 27
- Alexander P., Leahy J. P., 1987, MNRAS, 225, 1
- Athreya R. M., Kapahi V. K., 1999, in Röttgering H. J. A., Best P. N., Lehnert M. D., eds, The Most Distant Radio Galaxies Radio Galaxies from the MRC/1Jy sample. p. 453
- Baars J. W. M., Genzel R., Pauliny-Toth I. I. K., Witzel A., 1977, A&A, 61, 99
- Baldwin J. E., Scott P. F., 1973, MNRAS, 165, 259
- Barthel P. D., Miley G. K., 1988, Nature, 333, 319
- Begelman M. C., Blandford R. D., Rees M. J., 1984, Reviews of Modern Physics, 56, 255
- Begelman M. C., Cioffi D. F., 1989, ApJ, 345, L21
- Bennett A. S., 1962, MmRAS, 68, 163
- Best P. N., Bailer D. M., Longair M. S., Riley J. M., 1995, MNRAS, 275, 1171
- Best P. N., Longair M. S., Roettgering H. J. A., 1998, MNRAS, 295, 549
- Best P. N., Longair M. S., Roettgering J. H. A., 1997, MNRAS, 292, 758
- Best P. N., Longair M. S., Rottgering H. J. A., 1997, MNRAS, 286, 785
- Best P. N., Röttgering H. J. A., Longair M. S., 2000, MNRAS, 311, 23
- Blundell K. M., Rawlings S., Willott C. J., 1999, AJ, 117, 677
- Bogers W. J., Hes R., Barthel P. D., Zensus J. A., 1994, A&AS, 105, 91
- Bridle A. H., Hough D. H., Lonsdale C. J., Burns J. O., Laing R. A., 1994, AJ, 108, 766
- Carilli C. L., Perley R. A., Dreher J. W., Leahy J. P., 1991, ApJ, 383, 554
- Carvalho J. C., O’Dea C. P., 2002a, ApJS, 141, 337
- Carvalho J. C., O’Dea C. P., 2002b, ApJS, 141, 371
- Chambers K. C., Miley G. K., van Breugel W. J. M., 1990, ApJ, 363, 21
- Daly R. A., 1990, ApJ, 355, 416

- De Breuck C., van Breugel W., Röttgering H. J. A., Miley G., 2000, *A&AS*, 143, 303
- Dennett-Thorpe J., Bridle A. H., Laing R. A., Scheuer P. A. G., 1999, *MNRAS*, 304, 271
- Dennett-Thorpe J., Bridle A. H., Scheuer P. A. G., Laing R. A., Leahy J. P., 1997, *MNRAS*, 289, 753
- Fanaroff B. L., Riley J. M., 1974, *MNRAS*, 167, 31P
- Fernini I., Burns J. O., Perley R. A., 1997, *AJ*, 114, 2292
- Garrington S. T., Conway R. G., Leahy J. P., 1991, *MNRAS*, 250, 171
- Garrington S. T., Leahy J. P., Conway R. G., Laing R. A., 1988, *Nature*, 331, 147
- Gilbert G. M., Riley J. M., Hardcastle M. J., Croston J. H., Pooley G. G., Alexander P., 2004, *MNRAS*, 351, 845
- Goodlet J. A., Kaiser C. R., 2005, *MNRAS*, 359, 1456
- Goodlet J. A., Kaiser C. R., Best P. N., Dennett-Thorpe J., 2004, *MNRAS*, 347, 508
- Gopal-Krishna 1988, *A&A*, 192, 37
- Gopal-Krishna Wiita P. J., 2004, *ArXiv Astrophysics e-prints*
- Gower J. F. R., Scott P. F., Wills D., 1967, *MmRAS*, 71, 49
- Hardcastle M. J., Alexander P., Pooley G. G., Riley J. M., 1998, *MNRAS*, 296, 445
- Hes R., Barthel P. D., Fosbury R. A. E., 1996, *A&A*, 313, 423
- Hough D. H., Readhead A. C. S., 1989, *AJ*, 98, 1208
- Inskip K. J., Best P. N., Rawlings S., Longair M. S., Cotter G., Röttgering H. J. A., Eales S., 2002, *MNRAS*, 337, 1381
- Ishwara-Chandra C. H., Saikia D. J., 2000, *MNRAS*, 317, 658
- Ishwara-Chandra C. H., Saikia D. J., McCarthy P. J., van Breugel W. J. M., 2001, *MNRAS*, 323, 460
- Jackson N., Rawlings S., 1997, *MNRAS*, 286, 241
- Johnson R. A., Leahy J. P., Garrington S. T., 1995, *MNRAS*, 273, 877

- Kaiser C. R., Alexander P., 1997, *MNRAS*, 286, 215
- Kapahi V. K., Kulkarni V. K., 1990, *AJ*, 99, 1397
- Kapahi V. K., Saikia D. J., 1982, *Journal of Astrophysics and Astronomy* (ISSN 0250-6335), vol. 3, Dec. 1982, p. 465-483., 3, 465
- Klamer I. J., Ekers R. D., Bryant J. J., Hunstead R. W., Sadler E. M., De Breuck C., 2006, *MNRAS*, 371, 852
- Krolik J. H., Chen W., 1991, *AJ*, 102, 1659
- Kronberg P. P., Conway R. G., Gilbert J. A., 1972, *MNRAS*, 156, 275
- Kuehr H., Witzel A., Pauliny-Toth I. I. K., Nauber U., 1996, *VizieR Online Data Catalog*, 8005, 0
- Lacy M., Hill G. J., Kaiser M. E., Rawlings S., 1993, *MNRAS*, 263, 707
- Laing R., 1989, *Lecture Notes in Physics*, Berlin Springer Verlag, 327, 27
- Laing R. A., 1981, *MNRAS*, 195, 261
- Laing R. A., 1988, *Nature*, 331, 149
- Laing R. A., 1993, in Davis R. J., Booth R. S., eds, *Sub-arcsecond Radio Astronomy Relativistic flow in low luminosity radio jets*. p. 346
- Laing R. A., 1996, in Ekers R. D., Fanti C., Padrielli L., eds, *IAU Symp. 175: Extragalactic Radio Sources Large Scale Structure: Jets on kiloparsec Scales (Review)*. p. 147
- Laing R. A., Peacock J. A., 1980, *MNRAS*, 190, 903
- Laing R. A., Riley J. M., Longair M. S., 1983, *MNRAS*, 204, 151
- Law-Green J. D. B., Leahy J. P., Alexander P., Allington-Smith J. R., van Breugel W. J. M., Eales S. A., Rawlings S. G., Spinrad H., 1995, *MNRAS*, 274, 939
- Leahy J. P., 1987, *MNRAS*, 226, 433
- Leahy J. P., Muxlow T. W. B., Stephens P. W., 1989, *MNRAS*, 239, 401
- Leahy J. P., Williams A. G., 1984, *MNRAS*, 210, 929
- Liu R., Pooley G., 1991a, *MNRAS*, 249, 343

- Liu R., Pooley G., 1991b, MNRAS, 253, 669
- Liu R., Pooley G., Riley J. M., 1992, MNRAS, 257, 545
- Longair M. S., 1975, MNRAS, 173, 309
- MacDonald G. H., Kenderdine S., Neville A. C., 1968, MNRAS, 138, 259
- Macklin J. T., 1981, MNRAS, 196, 967
- McCarthy P. J., 1993, ARA&A, 31, 639
- McCarthy P. J., Miley G. K., de Koff S., Baum S. A., Sparks W. B., Golombek D., Biretta J., Macchetto F., 1997, ApJS, 112, 415
- McCarthy P. J., Spinrad H., van Breugel W., 1995, ApJS, 99, 27
- McCarthy P. J., van Breugel W., 1989, in Merus E. J. A., Fosbury R. A. E., eds, Extranuclear Activity in Galaxies Emission Line Properties of High Redshift Radio Galaxies. p. 55
- McCarthy P. J., van Breugel W., Kapahi V. K., 1991, ApJ, 371, 478
- Morris D., Tabara H., 1973, PASJ, 25, 295
- Mullin L. M., Hardcastle M. J., Riley J. M., 2006, MNRAS, 372, 113
- Myers S. T., Spangler S. R., 1985, ApJ, 291, 52
- Napier P. J., Thompson A. R., Ekers R. D., 1983, IEEE Proceedings, 71, 1295
- Neff S. G., Roberts L., Hutchings J. B., 1995, ApJS, 99, 349
- Orr M. J. L., Browne I. W. A., 1982, MNRAS, 200, 1067
- Pedely J. A., Rudnick L., McCarthy P. J., Spinrad H., 1989, AJ, 97, 647
- Perley R. A., Taylor G. B., 1991, AJ, 101, 1623
- Perucho M., Martí J. M., 2003, Publications of the Astronomical Society of Australia, 20, 94
- Pooley G. G., Henbest S. N., 1974, MNRAS, 169, 477
- Privon G. C., O’Dea C. P., Baum S. A., Axon D. J., Kharb P., Buchanan C. L., Sparks W., Chiaberge M., 2007, submitted to ApJ Suppl. Ser.

- Rees M. J., Setti G., 1968, *Nature*, 219, 127
- Riley J. M., Pooley G. G., 1975, *MmRAS*, 80, 105
- Roger R. S., Costain C. H., Bridle A. H., 1973, *AJ*, 78, 1030
- Scheuer P. A. G., 1982, in Heeschen D. S., Wade C. M., eds, *IAU Symp. 97: Extragalactic Radio Sources Morphology and power of radio sources*. pp 163–165
- Schilizzi R. T., Kapahi V. K., Neff S. G., 1982, *Journal of Astrophysics and Astronomy*, 3, 173
- Schwab F. R., 1980, *SPIE*, 231, 18
- Simard-Normandin M., Kronberg P. P., Button S., 1981, *ApJS*, 45, 97
- Simonetti J. H., Cordes J. M., Spangler S. R., 1984, *ApJ*, 284, 126
- Spinrad H., 1986, *PASP*, 98, 269
- Strom R. G., Conway R. G., 1985, *A&AS*, 61, 547
- Strom R. G., Riley J. M., Spinrad H., van Breugel W. J. M., Djorgovski S., Liebert J., McCarthy P. J., 1990, *A&A*, 227, 19
- Tribble P. C., 1991, *MNRAS*, 250, 726
- Wardle J. F. C., Kronberg P. P., 1974, *ApJ*, 194, 249
- Wellman G. F., Daly R. A., Wan L., 1997, *ApJ*, 480, 96
- Williams A. G., Gull S. F., 1985, *Nature*, 313, 34

